

Unclassified

SECURITY CLASSIFICATION OF THIS PAGE (When Data Entered)

REPORT DOCUMENTATION PAGE		READ INSTRUCTIONS BEFORE COMPLETING FORM
1. REPORT NUMBER 92828-1	2. GOVT ACCESSION NO.	3. RECIPIENT'S CATALOG NUMBER
4. TITLE (and Subtitle) Comparison of Techniques to Measure the Low Wavenumber Wall Pressure Spectrum of A Turbulent Boundary Layer		5. TYPE OF REPORT & PERIOD COVERED Final progress report
		6. PERFORMING ORG. REPORT NUMBER
7. AUTHOR(s) K. Martini, P. Leehey and M. Moeller		8. CONTRACT OR GRANT NUMBER(s) N00014-82-K-0728
9. PERFORMING ORGANIZATION NAME AND ADDRESS Massachusetts Institute of Technology Cambridge, Massachusetts 02139		10. PROGRAM ELEMENT, PROJECT, TASK AREA & WORK UNIT NUMBERS
11. CONTROLLING OFFICE NAME AND ADDRESS Office of Naval Research 800 North Quincy Street Arlington, VA 22217		12. REPORT DATE August 1984
		13. NUMBER OF PAGES 189
14. MONITORING AGENCY NAME & ADDRESS (If different from Controlling Office) Office of Naval Research 800 North Quincy Street Arlington, VA 22217		15. SECURITY CLASS. (of this report) Unclassified
		15a. DECLASSIFICATION/DOWNGRADING SCHEDULE
16. DISTRIBUTION STATEMENT (of this Report) Approved for public release; distribution unlimited.		
17. DISTRIBUTION STATEMENT (of the abstract entered in Block 20, if different from Report)		
18. SUPPLEMENTARY NOTES		
19. KEY WORDS (Continue on reverse side if necessary and identify by block number)		
20. ABSTRACT (Continue on reverse side if necessary and identify by block number) See page 2 of this report		

DD FORM 1 JAN 73 1473

EDITION OF 1 NOV 65 IS OBSOLETE
S/N 0102-014-6601

Unclassified

SECURITY CLASSIFICATION OF THIS PAGE (When Data Entered)

COMPARISON OF TECHNIQUES TO MEASURE THE LOW WAVENUMBER SPECTRUM OF A TURBULENT BOUNDARY LAYER

by

KYLE F. MARTINI

Report No. 92828-1

August, 1984

This research was carried out under the
Office of Naval Research, ACSAS Project
under Contract N00014-82-K-0728

Approved for public release; distribution unlimited

Acoustics and Vibration Laboratory
Massachusetts Institute of Technology,
Cambridge, Massachusetts 02139

Massachusetts Institute of Technology
Cambridge, Massachusetts 02139



COMPARISON OF TECHNIQUES TO MEASURE THE LOW
WAVENUMBER WALL PRESSURE SPECTRUM OF
A TURBULENT BOUNDARY LAYER

by

K. Martini, P. Leehey and M. Moeller

Abstract

The agreement between low wavenumber measurements of the turbulent wall pressure spectrum by various investigators has not been too good. Different techniques have been used in different facilities and have yielded data in different nondimensional frequency and wavenumber ranges. The current measurement program has utilized the wavenumber filtering techniques used by three primary investigators, the Martin plate, the Jameson plate and the Farabee and Geib 6-element microphone array in the same facility. Also a 12-element collinear and stagger array and a lateral array were used. The agreement between the different techniques in the M.I.T. facility is generally good. In addition, the difference of results between facilities has been reduced by displaying the data in a non-dimensional form that does not include the effect of boundary layer thickness. However, there was still a significant scatter in the data for each technique. Scatter is believed to be due to variation of each filter's wavenumber response away from the main acceptance lobe where the filter is responding to the acoustic and convective contamination and also the variation of the contamination with flow speed. The 6-element array was steered to determine the levels of the acoustic and convective response of a single microphone in the array. The levels were determined to be quite significant.

Acknowledgements

There are many individuals who have made significant contributions to this report effort and deserve a special word of appreciation. We would like to thank Dr. Nathan Martin, Mr. F. Ellsworth Geib, Jr. and Mr. Paul Jameson who all discussed freely and openly their low wavenumber experiments which we repeated at M.I.T. Special thanks goes to Hung Son Nguyen who created software to mate the A to D converter to the PDP 11/44 computer so we could steer our array and to Margaret Cahoon for her efficient typing of this report.

The financial support for this work was provided for by the Office of Naval Research under contract N00014-82-K-0728.

TABLE OF CONTENTS

	<u>Page</u>
ABSTRACT	2
ACKNOWLEDGEMENTS	3
TABLE OF CONTENTS	4
LIST OF TABLES	7
LIST OF FIGURES	8
LIST OF SYMBOLS	13
I. INTRODUCTION	16
II. RESPONSE OF WAVENUMBER FILTERS TO TURBULENT BOUNDARY LAYER WALL PRESSURE FIELDS .	19
2.1 Properties of Wall Pressure Spectra	19
2.2 Microphone Array Wavenumber Filter	20
2.2.1 Single Microphone Response	20
2.2.2 Microphone Array Response	24
2.2.3 Array Design	27
2.3 Structural Plate Wavenumber Filter	30
2.3.1 Plate Response	30
2.3.2 The Martin Plate	34
2.3.3 The Jameson Plate	35
III. EXPERIMENTAL FACILITIES	37
3.1 M.I.T. Low Noise, Low Turbulence Wind Tunnel	37
3.2 Boundary Layer Tests	38
3.2.1 Test Boundary Configuration	38
3.2.2 Boundary Layer Profiles	39
3.2.3 Single Point Wall Pressure Spectra .	40
3.3 Measurement of Background Acoustic Noise .	41
3.4 Comparison of the M.I.T. Facility with the BBN Facility	43
IV. WAVENUMBER FILTER MEASUREMENTS	45
4.1 Experimental Source of Excitation	45

	<u>Page</u>
IV. WAVENUMBER FILTER MEASUREMENTS (cont'd)	
4.2 Microphone Array Measurements	46
4.2.1 Alternating Phased Array	46
4.2.2 The Convective Region-- Alternating Array	47
4.2.3 The Acoustic Region-- Alternating Array	49
4.2.4 The Low Wavenumber Region-- Alternating Array	52
4.2.5 The Common Phased Array	53
4.3 Plate Measurements	53
4.3.1 The Martin Plate	53
4.3.2 The Jameson Plate	55
4.3.3 Plate Convective Response	57
4.3.4 Plate Acoustic Response	58
4.3.5 Plate Low Wavenumber Response	61
V. LOW WAVENUMBER RESULTS	62
5.1 Microphone Low Wavenumber Results	62
5.1.1 Method of Calculating Low Wavenumbers	62
5.1.2 Alternating Phase Results	63
5.1.3 Common Phase Results	65
5.2 Plate Low Wavenumber Results	65
5.2.1 Method of Calculating Low Wavenumbers	65
5.2.2 Martin Plate Results	68
5.2.3 Jameson Plate Results	68
5.3 Effect of Boundary Layer Thickness on Low Wavenumber Results	69
5.4 A Look at Other Normalization	69
5.5 Comparison with Other Investigators	70
5.5.1 Martin Plate	70
5.5.2 Jameson Plate	70
5.5.3 Microphone Array	72
5.6 Low Wavenumbers in the Wavenumber- Frequency Plane	72

	<u>Page</u>
VI. CONCLUSIONS	74
6.1 Conclusions on Acoustic Contamination	74
6.2 Conclusions on Convective Contamination	76
6.3 Conclusions on Low Wavenumber Data	77
APPENDIX A. 12-ELEMENT MICROPHONE ARRAY	81
A.1 12-ELEMENT COLLINEAR ARRAY	81
A.2 12-ELEMENT STAGGER ARRAY	84
A.3 CROSS ARRAY	87
APPENDIX B. ARRAY STEERING	88
B.1 BEAMFORMING	88
B.2 ARRAY STEERING IN THE WIND TUNNEL	91
REFERENCES	95

LIST OF TABLES

Table No.

- | | |
|-----|--|
| 2.1 | Comparison of Experimentally Determined Characteristics of Martin's CCCC Plate |
| 2.2 | Comparison of Experimentally Determined Characteristics of Jameson's Plate |
| 3.1 | Boundary Layer Flow Properties |
| 4.1 | Comparison of Acoustic Sensitivity Test on Martin Plate with Speakers at Two Different Locations |
| 5.1 | Measured Microphone Alternating Phased Array Levels |
| 5.2 | Measured Microphone Common Phased Array Levels |
| 5.3 | Measured Martin Plate Acceleration Levels |
| 5.4 | Measured Jameson Plate Acceleration Levels |
| A1 | 12-Element Collinear Array Measured Low Wavenumber Levels |
| A2 | 12-Element Stagger Array Measured Low Wavenumber Levels |
| B1 | Steered Acoustic Levels in Wind Tunnel @ 15 m/s |
| B2 | Steered Convective Levels in Wind Tunnel @ 15 m/s |

LIST OF FIGURES

Figure Number

- 2.1 Wall Pressure Spectrum at a Particular Frequency as a Function of Streamwise Wavenumber
- 2.2 Microphone Spatial Sensitivity
- 2.3 Microphone Wavenumber Response
- 2.4 Calculated Common Phased Microphone Array Wavenumber Response
- 2.5 Calculated Alternating Phased Microphone Array Wavenumber Response
- 2.6 Schematic of Analog Summation Box
- 2.7 Measured Alternating Phased Array Wavenumber Response
- 2.8 Effect of Shading on Wavenumber Response
- 2.9 Measured Common Phased Array Wavenumber Response
- 2.10 Geometric Configuration of Plate Structure
- 3.1 M.I.T. Wind Tunnel Facility
- 3.2 Hard Walled Duct Test Configuration
- 3.3 Wall Jet Configuration (side view)
- 3.4 Wall Jet Configuration (top view)
- 3.5 Boundary Layer Measurement Comparison
- 3.6 Wall Pressure Spectra Comparison
- 3.7 Acoustic Measurement Setup
- 3.8 Comparison of Background Noise With Martin (1976)
- 3.9 Comparison Between Two Flushed Mounted 1" Microphones 15 M/S

- 3.10 Cross Spectrum and Phase Between Two
1" Microphones @ 15 M/S
- 3.11 Coherence Between Two 1" Microphones
@ 15 M/S
- 3.12 Single Point Wall Pressure Measurement
@ 40 M/S
- 3.13 Cross Spectrum and Phase Between Two
1" Microphones @ 40 M/S
- 3.14 Comparison Between Blockhouse Noise
Measurements and Flush Mounted
Microphone @ 40 M/S
- 3.15 Comparison of Flush Mounted Microphone
With Jameson
- 3.16 Comparison of Blockhouse Noise With
Jameson
- 4.1 Comparison of Various Microphone
Measurements @ 15 M/S
- 4.2 Relationship Between the Peak of the
Array Sensitivity and the Turbulent
and Acoustic Pressure Spectra
- 4.3 Coherence Between the Array and a
Single Microphone in the Array @ 15 M/S
- 4.4 Comparison of Alternating Phased Array
@ 15 M/S and 40 M/S
- 4.5 Cross Spectrum and Phase Relation
Between Two Microphones Excited by a
Plane Acoustic Wave
- 4.6 Comparison of the Alternating Phased
Response for Various Shading @ 15 M/S
- 4.7 Comparison of Coherence for Various
Shadings
- 4.8 The Common Phased Array Response
- 4.9 Coherence of Common Phased Array @ 15 M/S

- 4.10 Measured Wavenumber Filter Shape of the Martin (15,1) Mode Made by Martin [5]
- 4.11 Measured Acceleration Spectrum of Martin Plate @ 40 M/S
- 4.12 Measured Acceleration Spectrum of (odd,odd) Modes of Jameson Plate @ 40 M/S
- 4.13 Measured Acceleration Spectrum of (odd,2) Modes of Jameson Plate @ 40 M/S
- 4.14 Directivity Pattern of a Circular Cylinder
- 4.15 Contours of the Directivity Pattern as a Function of Polar Angle and Frequencies
- 4.16 Possible Effect of Different Sources on the Acoustic Levels Measured by the Blockhouse Microphone
- 5.1 Alternating Phased Uniformed Shaded Array Result from Position 1
- 5.2 Comparison of Alternating Phased Shaded Array Results Between Position 1 and 2
- 5.3 Comparison of Different Shading for Alternating Phased Array
- 5.4 Comparison Between Alternating Phase and Common Phased Array
- 5.5 Martin Plate Results at Position 1
- 5.6 Comparison of Martin Plate Results Between Position 1 and Position 2
- 5.7 Jameson Plate Results at Position 1
- 5.8 Alternating Phased Array Results with $\delta^* = 0.2$ inches
- 5.9 Martin Plate Results with $\delta^* = 0.2$ inches
- 5.10 Alternating Phased Array Result Normalizing on Inner Variables

- 5.11 Alternating Phased Array Result Normalizing on Flow Parameters
- 5.12 Martin Plate Results Normalizing on Flow Parameters
- 5.13 Martin Plate Results Compared with Previous Investigators
- 5.14 Jameson Plate Results Compared with Previous Investigators
- 5.15 Alternating Phased Array Results Compared with Previous Investigators
- 5.16 Low Wavenumber Results of Martin Plate in ω -k Plane
- 5.17 Low Wavenumber Results of Jameson Plate in ω -k Plane
- 5.18 Low Wavenumber Results of Microphone Arrays in ω -k Plane

- A1 12-Element Collinear Array
- A2 12-Element Stagger Array
- A3 Cross Array
- A4 Comparison of 6 and 12 Element Alternating Phased Wavenumber Response
- A5 12-Element Alternate Phased Array @ 15 m/s
- A6 Coherence of 12-Element Alternate Phased Array @ 15 m/s
- A7 12-Element Low Wavenumber Result--Uniform Shading
- A8 12-Element Low Wavenumber Result--Chebyshev Shading
- A9 12-Element Stagger Array Alternate Phased Wavenumber Response
- A10 12-Element Stagger Array Alternate Phased @ 15 m/s
- A11 Coherence of Stagger Array @ 15 m/s

- A12 Alternate Phased Stagger Array Wavenumber Response
@ $k_3 = 1.4\pi/d_3$
- A13 Stagger Array Low Wavenumber Results
- A14 Transfer Function Between Lateral Array and Single
Microphone @ 15 m/s
- B1 Trace Waves
- B2 Weighted Delay-and-Sum Beamforming
- B3 Frequency Domain Beamforming
- B4 Relationship among Turbulent and Acoustic
Pressure Spectra in ω -k Space
- B5 Downstream Acoustic Steered Array @ 15 m/s
- B6 Upstream Convectively Steered Array @ 15 m/s

LIST OF SYMBOLS

$ A(\underline{k}) ^2$	Point array wavenumber response
$ A_m(k_1) ^2$	Plate longitudinal shape factor
$ A_n(k_3) ^2$	Plate lateral shape factor
c_o	Velocity of sound in air
D	Flexural rigidity
$f_{mn}(x,z)$	Two-dimensional normal mode shape (m,n) mode
f_{mn}	Natural frequency of (m,n) mode
$ F_{mn}(k_1 k_3) ^2$	Two-dimensional wavenumber filter shape function
$g_m(x)$	Longitudinal mode shape
$h_n(z)$	Lateral mode shape
H	Boundary layer shape factor, $H = \delta^*/\theta$
$ H_{mn}(\omega) ^2$	Modal frequency response at resonance
k	Wavenumber: k_1 = longitudinal; k_3 = lateral
k_A	Acoustic wavenumber $k_A = \omega/c_o$
k_C	convective wavenumber, $k_C = \omega/U_C$
L	Structural dimension: L_1 = longitudinal; L_3 = lateral

LIST OF SYMBOLS (Continued)--

L_p	Level in dB
$p(\underline{x}, t)$	Instantaneous wall pressure fluctuation at position \underline{x} and time t
$P_m(t)$	Measured area-averaged instantaneous pressure
$P_{mn}(\omega)$	Modal pressure, (m,n) mode
$P(k_1, k_3, \omega)$	Measured wavenumber-frequency spectral density of wall pressure
q	Free stream dynamic head, $q = \frac{1}{2}\rho U_{c_0}^2$
$R(\underline{x}, t)$	Cross-correlation of the wall pressure
$S_w(x, z, \omega)$	Theoretical displacement spectral density
$S_a(x, z, \omega)$	Theoretical acceleration spectral density
$S(\underline{x})$	Microphone facial sensitivity distribution
S	Strouhal number
U_c	Convective velocity
U_∞	Free stream velocity
V_*	Friction velocity
$W(x, z, t)$	Instantaneous displacement at position (x, z)

LIST OF SYMBOLS (continued)--

$ W(\underline{k}) ^2$	Microphone array wavenumber response
x	Longitudinal distance variable
z	Lateral distance variable
β	Damping force per unit mass
δ^*	Boundary layer displacement thickness
η	Damping loss factor
θ	Boundary layer thickness
ρ	Fluid density
σ	Structural surface density
$\Phi(k, \omega)$	Wavenumber-frequency spectrum of the wall pressure
$\Phi(\underline{k}, \omega)_L$	Low wavenumber frequency spectrum of the wall pressure
$\Phi(\omega)$	Frequency spectrum of the wall pressure
ν	Kinematic viscosity
ω	Radian frequency
ω_{mn}	Resonant frequency at (m,n) mode
ω^*	Non-dimensional frequency $\omega^* = \frac{\omega \delta^*}{U_\infty}$

COMPARISON OF TECHNIQUES TO MEASURE THE LOW
WAVENUMBER SPECTRUM OF A TURBULENT
BOUNDARY LAYER

I. INTRODUCTION

The turbulent boundary layer that grows on vehicles moving through a viscous fluid causes pressure fluctuations on the surface of the vehicle. These pressure fluctuations can be an important source of structural vibration and contribute to the internal vehicle noise. These problems are encountered in many marine applications and in high speed aircraft.

The pressure field beneath a thick turbulent boundary layer has been investigated in the past. Single flush mounted transducers have been used to measure the root mean square wall pressure levels and the single point wall pressure spectra. Pairs of flush mounted transducers have been used to measure the two point wall pressure statistics of a turbulent boundary layer. These two point statistics describe the convective ridge, i.e., the part of the wall pressure spectrum associated with eddies convecting downstream at a major fraction of the freestream velocity.

In many marine applications the convective ridge is inefficient at producing structural vibration due to the low freestream velocities and the high frequencies of interest. Sources of excitation better coupled to the structural modes are the low wavenumber (long wavelength) components of the turbulent boundary layer. These low

wavenumber components do not contribute significantly to the single point wall pressure spectrum and so it is necessary to construct spatial filters in order to measure them.

There are two methods of constructing spatial filters for the measurement of the low wavenumber levels. Maidanik and Jorgensen [1] have shown that an array of flush mounted transducers can be used as a spatial filter. Blake and Chase [2], Jameson [7] and Farabee and Geib [3] used this technique. Aupperle and Lambert [4] showed how beams act as wavenumber filters. Martin [5], Jameson [8], and Moeller et al. [8] used the spatial filtering of clamped plates to make low wavenumber measurements. To date the two techniques have not been used in the same facility and have tended to yield data in different nondimensional frequency and wavenumber ranges. The agreement between the various investigators has not been too good. There has been a lot of scatter in the reported data.

The current measurement program has been to utilize both wavenumber filtering techniques in the same facility. The Martin [5] clamped plate, the Jameson [8] clamped plate, and the Farabee and Geib [3] 6-element microphone array wavenumber filters were used to perform the low wavenumber measurements. This will allow for a direct comparison of the techniques used by the three primary investigators.

Additional measurements have been made with a 12-element microphone array using three different configurations, a 12-element collinear array, a 12-element staggered array (an

attempt to decrease the inter-element spacing), and a 7X5 element cross array to determine any lateral wavenumber dependence. The description of these arrays and their results are discussed in Appendix A.

Array steering techniques using a DATEL 16-channel Analog to Digital converter and a DEC PDP11/44 computer to measure the array response to the acoustic contamination in the M.I.T. wind tunnel and the convective ridge. The procedure and results are discussed in Appendix B.

II. RESPONSE OF WAVENUMBER FILTERS TO TURBULENT BOUNDARY LAYER WALL PRESSURE FIELDS

2.1 Properties of Wall Pressure Spectra

The wall pressure field beneath a turbulent boundary layer is very complicated. The pressure fluctuations exerted on the wall are varied in both space and time. Statistical properties such as the root mean square wall pressure, the cross correlation, the spectral density, and cross spectral density, etc. are used to describe the pressure field.

The wall pressure beneath a turbulent boundary layer is denoted by $p(\underline{x}, t)$, where $\underline{x} = (x_1, x_3)$ is the distance vector in the plane of the wall, x_1 is the streamwise direction and x_3 is the cross-stream direction. The component x_2 is normal to the wall. Assuming the wall pressure field is homogeneous and stationary, the cross-correlation of the pressure at two points on the boundary is

$$R(\underline{x}, t) = \langle p(\underline{x}', t') p(\underline{x}' + \underline{x}, t' + t) \rangle \quad (2.1)$$

where the brackets $\langle \rangle$ represent a time average, \underline{x} is the separation distance between the two points, and t is a time delay. The wavenumber-frequency spectrum is obtained from $R(\underline{x}, t)$ by taking the Fourier transform over space and time,

$$\Phi(\underline{k}, \omega) = \frac{1}{(2\pi)^3} \int \int \int R(\underline{x}, t) \exp[-i(\underline{k} \cdot \underline{x} - \omega t)] d\underline{x} dt \quad (2.2)$$

where $i = \sqrt{-1}$, \underline{k} is the vector wavenumber, ω is the radian frequency, and the integration limits are from $-\infty$ to $+\infty$.

$\Phi(\underline{k}, \omega)$ describes the distribution of energy in the pressure field in terms of frequency and wavenumber. The behavior of the wavenumber-frequency spectrum is determined by the decay and convection of eddies in the turbulent boundary layer field. The convection of eddies lead to a high value of wavenumber-frequency spectrum along a convective ridge defined by $k_c = \omega / u_c(\omega)$, where $u_c(\omega)$ is the convective velocity. A schematic of the distribution of energy at a fixed frequency is given in Figure 2.1 [3]. This shows the strong convective ridge centered at $k_c = \omega' / u_c$. It also shows that the acoustic energy is restricted to the region of wavenumber space $0 < k \leq \omega' / c_0$, where c_0 is the speed of sound in the field.

The region of interest is the low wavenumber region $\omega' / c_0 < k_L < \omega' / u_\infty$. To make a measurement in this region it is necessary to reject both the acoustic contamination and the convective contamination. Section 2.2 describes how a microphone array acts as a wavenumber filter and Section 2.3 describes how the response of a plate can be used as a wavenumber filter.

2.2 Microphone Array Wavenumber Filter

2.2.1--Single Microphone Response. The frequency spectral density of wall-pressure fluctuation at a point is

$$\Phi(\omega) = \frac{1}{2\pi} \int R(0, t) e^{i\omega t} dt = \int \int \Phi(\underline{k}, \omega) d\underline{k} \quad (2.3)$$

The measurement of the frequency spectral density using a

single flush-mounted microphone involves the influence of the microphone facial sensitivity distribution $S(\underline{x})$ in averaging small-wavelength wall pressure components. When subject to a pressure field $p(\underline{x}, t)$, the microphone, on assumption of instantaneous response, measures an area-averaged pressure

$$p_m(t) = \int \int S(\underline{x}) p(\underline{x}, t) d\underline{x} \quad (2.4)$$

where $\int \int S(\underline{x}) d\underline{x} = 1$ (2.5)

The response function $|H(\underline{k})|^2$, expresses the facial distribution as a wavenumber filter and is defined by

$$H(\underline{k}) = \int \int S(\underline{x}) \exp[-i\underline{k} \cdot \underline{x}] d\underline{x} \quad (2.6)$$

where \underline{x} may be measured from the center of the face and $S(\underline{x})$ vanishes for \underline{x} outside the sensitive area. The frequency spectrum of area-averaged pressure measured by a single microphone is then given by

$$\Phi_M(\omega) = \int \int |H(\underline{k})|^2 \Phi(\underline{k}, \omega) d\underline{k} \quad (2.7)$$

The frequency response of the microphone is assumed [2] to be independent of the wavenumber response and will be neglected in this discussion.

If the microphone is a circular transducer of radius R and uniform facial sensitivity, then

$$|H(\underline{k})|^2 = [2J_1(kR)/kR]^2 \quad (2.8)$$

where $k^2 = k_1^2 + k_3^2$ and J_1 is a Bessel function of the first kind. The response $|H(\underline{k})|^2$ has an upper bound that decreases with kR and thus attenuates the high-wavenumber components of the pressure field.

The microphone actually used had a facial sensitivity significantly nonuniform. The microphones used to perform the measurements were Bruel & Kjaer (B&K) Type 4144 Condenser Microphones with a diaphragm radius of 0.37 inches. The distribution of the facial sensitivity of a nearly identical microphone was measured by Bruel and Rasmussen [9]. This sensitivity function has negligible frequency dependence up to 2 kHz, and although the frequency dependence changes perceptibly beyond this, the spatial function $S(\underline{x})$ for use in Equation (2.5) changes little up to 4 kHz.

The function $S(\underline{x})$ derived from the measured sensitivity distribution with neglect of small phase differences and assumption of circular symmetry is shown in Figure 2.2 (provided by Geib at DTNSRDC). This function, which is now written $S(r/R)$, with argument (r/R) , defined as distance from the microphone center, can be closely approximated by [2]

$$\frac{S(r/R)}{S(0)} = B[1 - \beta K_0(\frac{\alpha r}{R})] \quad 0 < r < R \quad (2.9)$$

$$\text{where } B=0.198, \alpha=2.96 \text{ and } \beta=-4.06. \quad (2.10)$$

as shown in Figure 2.2. Equation (2.10) permits the quadrature of Equation (2.6) to be performed to yield the

corresponding area averaging function, written as

$$|H(\underline{k})|^2 \equiv |H(kR)|^2 \quad \text{where [10]}$$

$$H(kR) = \frac{kR[1-\beta J_0(\alpha)]J_1(kR) + \alpha\beta J_1(\alpha)J_0(kR) - \alpha^2(kR)^{-1}J_1(kR)}{((kR)^2 - \alpha^2)[\frac{1}{2} - (\beta/\alpha)J_1(\alpha)]} \quad (2.11)$$

Analytically, the attenuation of this function as $kR \rightarrow \infty$ can be estimated by using the approximations to Bessel functions of the large argument. In this approximation

$$|H(kR)|^2 \rightarrow 2c_0(kR)^{-5} \cos^2(kR - \pi/4) \quad (2.12)$$

$$\text{where } c_0 = \frac{4\alpha^2\beta^2 J_1^2(\alpha)}{\pi[1-2(\beta/\alpha)J_1(\alpha)]^2} \approx 5.93 \quad (2.13)$$

for $kR \gg \alpha$ and $kR \gg 1$

Although the approximation to the measured sensitivity, given by Equations (2.9) and (2.10) is generally good, it has limited validity with regard to the small-scale variation of the true sensitivity near the element periphery. Accordingly, because of the sensitivity of $H(kR)$ to variation at large kR , beyond some maximum kR , Equations (2.12) and (2.13) should not be used except for order-of-magnitude considerations.

The area-averaging function $|H(kR)|^2$ for the microphone, as approximated by Equations (2.10) and (2.11) is shown in Figure 2.3, along with the results of Equation (2.8) that would apply if the facial sensitivity were uniform. The difference is significant. The actual lobes were wider and

the rate of decrease from lobe to lobe is more rapid. The actual microphone discriminates more effectively against higher wavenumbers.

2.2.2--Microphone Array Response. Maidanik and Jorgensen [1] have shown that a flush-mounted pressure transducer system can be used to construct a wave-vector filter to study the nature of the boundary pressure field in a turbulent boundary layer. For a transducer system consisting of a linear array of uniform microphones equally spaced, the wavenumber response of wave-vector filter is

$$|W(k)|^2 = |H(k)|^2 |A(k)|^2 \quad (2.14)$$

and the frequency spectrum measured by an array of microphones is then

$$\Phi_M(\omega) = \int \int |W(k)|^2 \Phi(k, \omega) dk \quad (2.15)$$

where $|H(k)|^2$ is the wavenumber response of a single microphone as described in Equation (2.6) and $|A(k)|^2$ is the array wavenumber response. The frequency response of the microphone is assumed to be independent of the wavenumber response in the frequency range of interest (see Section 2.2.1). For the array of N uniform microphones equally spaced, and with no time delays, the array response is

$$|A(k)|^2 = N^{-2} \left| \sum_{n=0}^{N-1} S_n \exp(-ink \cdot d) \right|^2 \quad (2.16)$$

where d is the separation distance and S_n represents the magnitude and polarity of the sensitivity of the nth microphone.

The filtering action of the array can be modified by adjusting the magnitude and polarity of S_n for each microphone. This is called shading the array. The simplest shading is the uniform shaded or the unshaded array. For this type of shading the magnitude of each microphone is adjusted so that $|S_n|=1$. For an array of microphones aligned in the k direction, Equation (2.15) can be written

$$|A(k)|^2 = \frac{1}{N^2} \sin^2(\frac{1}{2}Nk_1d) / \sin^2(\frac{1}{2}k_1d) \quad \text{for } S_n = (-1)^{2n} \quad (2.17)$$

$$= \frac{1}{N^2} \sin^2(\frac{1}{2}Nk_1d) / \cos^2(\frac{1}{2}k_1d) \quad \text{for } S_n = (-1)^{n+N} \text{ even} \quad (2.18)$$

$$= \frac{1}{N^2} \cos^2(\frac{1}{2}Nk_1d) / \cos^2(\frac{1}{2}k_1d) \quad \text{for } S_n = (-1)^{n+N} \text{ odd} \quad (2.19)$$

Equation (2.17) is for a common phased array and is plotted in Figure 2.4 for $N=6$. The major characteristics of the array are shown on this figure. The main lobe occurs at $k_1d/\pi=0$, and aliasing lobes occur at $k_1d/\pi=2,4$, etc. The width of the main lobe and the aliasing lobe is $\pi/3d$.

Equations (2.18) and (2.19) are for an alternating phased array. This type of summing shifts the array response by $k_1d/\pi=1$. The characteristics are then the same as for the common phased array. The alternating phased array shifts the main lobe of the response out of the acoustic region, but does not shift it into the convective region. Thus the alternating phased array will produce the best low wavenumber results in the frequency region where the main lobe is between the

acoustic and convective region.

Equation (2.18) is plotted in Figure 2.5 for $N=6$. Also plotted on this figure is Equation (2.11), the response of a single B&K Microphone with $d/R=1.63$. The choice of $d/R=1.63$ is to nullify the effect of the first aliasing lobe of the array occurring at $k_1 d/\pi=3$ by the minimum in the single microphone response occurring at $k_1 R=5.8$. Nullifying the first aliasing lobe will reduce the effect of the convective ridge region as will be discussed in Section IV.

A significant amount of noise is still admitted by nearby minor lobes and more distant major lobes. The response of the actual microphone, Equation (2.10), reduces the acceptance at wavenumbers higher than that of the main lobe as was shown in Figure 2.3. In addition, suppression of the minor lobes can be accomplished by using a different type of array shading. This type of array shading is just assigning unequal weights S_n to microphone outputs in Equation (2.16).

Two different array shadings were used to suppress the minor lobes. One was Chebyshev shading [11]. This shading is an optimal method. The coefficients S_n can be chosen so as to reduce the minor lobes by any specific amount. For a given level of reduction the widening of the major lobe is minimized with respect to other shading. The other shading used was Binomial shading [12]. This method results in the total elimination of the side lobes for spacing less than one-half wavelength but greatly increases the main lobe's width. The effects of the two shadings described above will

be discussed in greater detail in Section IV.

2.2.3--Array Design. The Farabee and Geib [3] 6-element microphone array measurements were repeated using the same microphones, preamplifiers, microphone power supplies, and mounting plate for the array as was used at the David Taylor Naval Ship Research and Development Center. An additional six microphones of the same type were used to create a 12-element array of various configurations. The design of the 6-element array with analog summation box is described below. Appendix A describes the 12-element array configuration, and Appendix B describes the array steering techniques used to determine the array response to the convective ridge and the wind tunnel acoustic contamination.

The microphones were 1" Bruel & Kjaer Type 4144 Condensor Microphones with diaphragm radius of $R=0.35$ inches. The array consisted of six microphones mounted flush in the wall of the test section aligned with the direction of the flow. The center to center spacing of the microphones was $d=1.06$ inches, giving a d/R ratio of 3.03. The desired ratio of 1.63 ($d=0.86$ inches) could not be obtained because the outer diameter of the Type 4144 microphone was 1 inch. Special caps were used for the microphones to eliminate discontinuities over the surface of the array.

The microphone signals passed through the Bruel & Kjaer Type 2619 FET preamplifiers, Bruel & Kjaer Type 2606 Microphone amplifiers, and then through a Precision Filter

Programmable Multi-Channel Filter System. The signal then passed into an analog summation box that was built so the array could be used in real time. The box has six inputs, with the gain of each input controlled by a trimming potentiometer. Each input has an on-ground switch so that four, five or six elements can be tested. A schematic of the box is shown in Figure 2.6. The outputs of the box are the common phased array and the alternating phased array. The dynamic range of the summing box is sufficient so that the box is not the limiting factor in the array performance.

The performance of the array was qualitatively checked, in-situ, using an acoustic source in the inlet to the muffler diffuser. This caused a plane acoustic wave to travel down the test section. The wavenumber of the acoustic wave could be inferred from the relation $k_1 = \omega/c_0$, where c_0 is the speed of sound in air.

The microphones were calibrated using a Bruel & Kjaer Pistonphone. It yields a calibration at 250 Hz. The microphone response was assumed to be flat through the frequency range of interest, $1 \text{ kHz} < f < 5 \text{ kHz}$. The microphones have a resonance near 8 kHz. Near the resonance, the phase between microphones varies greatly and the acoustic check will give erroneous results. However, the acoustic check is useful for frequencies well below the microphone's resonant frequency. The rejection of acoustic noise in the

test facility can be inferred from the acoustic check of the microphones.

Figure 2.7 shows the result of the acoustic check for the alternating phased uniform shaded array in both frequencies as measured and the equivalent wavenumber. The main lobe occurs at 6.3 kHz or $k=2.9 \text{ in}^{-1}$. This is assumed to be the main acceptance wavenumber region for the filter. The sidelobes are approximately 12-15 dB down from the main lobe. There are two nulls before the main lobe at 2.2 kHz and 4.4 kHz. Data obtained at these frequencies will have a reduction in the response to acoustic plane waves.

Figure 2.8 shows the effect of Chebyshev and Binomial shading on the alternating phased array. For the Chebyshev shading, the reduction in the side lobe is approximately 30 dB and the width of the main lobe is approximately 1.5 times that for the Uniform shaded array. The Binomial shading virtually eliminates the side lobe, but the main lobe is increased to over twice that of the Uniform shaded array.

Figure 2.9 shows the result of the acoustic calibration of the common phased Uniform shaded array. The main lobe occurs at $k=0$. The side lobes are again 12-15 dB down from the main lobe and the first two nulls occur at 2.2 and 4.2 kHz. The first aliasing lobe occurs at about 12 kHz.

2.3 Structural Plate Wavenumber Filters

2.3.1--Plate Response. Aupperle and Lambert [4] have described analytically the wavenumber filtering action of beams. The concept of the wavenumber filter shape, $|A_m(k)|^2$, is shown to come from a normal mode analysis of structural response to random pressure excitation. Martin [5,12] discusses both analytical and numerical techniques for evaluating $|A_m(k)|^2$ for several ideal structures as well as techniques for measuring $|A_m(k)|^2$ via mode shape measurements. The techniques used within are the same as Martin [5] used and will be briefly summarized for rectangular plates.

The geometric configuration of the plate structure is shown in Figure 2.10. The structure is characterized by dimensions L_1 and L_3 , uniform mass per area σ , and flexural rigidity D . The transverse displacement $W(x,z,t)$ represents the response of the plate when excited by a normal random pressure field $p(x,z,t)$ and subjected to a uniform damping force per unit mass $\beta \frac{\partial W}{\partial t}$. The governing dynamic equation is

$$(D\nabla^4 + \sigma \frac{\partial^2}{\partial t^2} + \sigma \beta \frac{\partial}{\partial t}) W(x,z,t) = p(x,z,t) \quad (2.20)$$

Solving this equation using normal mode techniques results in

$$W(x,z,\omega) = \sum_{m=1}^{\infty} \sum_{n=1}^{\infty} \frac{1}{\sigma(\omega^2 - \omega_{mn}^2 - i\beta\omega)} P_{mn}(\omega) f_{mn}(x,z) \quad (2.21)$$

where ω_{mn} are the eigenvalues and $f_{mn}(x,z)$ are the normal modes. The following normalization was used for the orthogonal function

$$\int_0^{L_1} \int_0^{L_3} f_{mn}(x,z) f_{jk}(x,z) dx dz = \delta_{mj} \delta_{nk} \quad (2.22)$$

P_{mn} is the modal pressure defined by

$$P_{mn} = \int \int p(x,z,\omega) f_{mn}(x,z) dx dz \quad (2.23)$$

Martin [5,12] then shows when considering only the resonant frequencies of the structure (ω_{mn}), and modal overlap is negligible, the displacement response spectral density can be written as

$$\begin{aligned} S_w(x,z,\omega_{mn}) &= \\ &= f_{mn}^2(x,z) |H_{mn}(\omega_{mn})|^2 \int_{-\infty}^{\infty} \int_{-\infty}^{\infty} |F_{mn}(k_1,k_3)|^2 \Phi(k_1,k_3,\omega_{mn}) dk_1 dk_3 \end{aligned} \quad (2.24)$$

where $\Phi(k_1, k_3, \omega)$ is the wall pressure wavenumber-frequency spectrum as described in Equation (2.2). $|H_{mn}(\omega)|^2$ is the modal frequency response which at resonance is

$$|H_{mn}(\omega_{mn})|^2 = \frac{1}{(\sigma\beta\omega_{mn})^2} = \frac{1}{(\sigma\eta\omega_{mn}^2)^2} \quad (2.25)$$

where $\eta_{mn} = (\beta_{mn}/\omega_{mn})$ is the loss factor. $|F_{mn}(k_1, k_3)|^2$ is the two-dimensional wavenumber filter shape defined as

$$F_{mn}(k_1, k_3) = \int_0^{L_1} \int_0^{L_3} f_{mn}(x, z) e^{i(k_1 x + k_3 z)} dx dz \quad (2.26)$$

In an experimental sense Equation (2.24) can be used to relate the pressure excitation to the vibratory response if the modal characteristics $|H_{mn}(\omega_{mn})|^2$ and $|F_{mn}(k_1, k_3)|^2$ can be determined accurately. The evaluation of $|H_{mn}(\omega_{mn})|^2$ requires only a determination of the total damping and surface density associated with the modes under consideration.

In many cases the normal mode shape $F_{mn}(x, z)$ is easily separated into an x-dependent term and a z-dependent term. This separation of variables is analytically exact for plates having any two opposite sides simply supported. Even for the case of the fully clamped plate, a separation of variables technique using clamped beam function is often used as a reasonable approximation to the mode shape since an exact solution is unobtainable in closed form. To take advantage of this separation of variables, let

$$f_{mn}(x, z) = g_m(x) h_n(z) \quad (2.27)$$

Substitution of Equation (2.27) into Equation (2.25) yields

$$F_{mn}(k_1, k_3) = \int_0^{L_1} g_m(x) e^{ik_1 x} dx \int_0^{L_3} h_n(z) e^{ik_3 z} dz \quad (2.28)$$

Defining

$$\begin{aligned} A_m(k_1) &= \int_0^{L_1} g_m(x) e^{ik_1 x} dx \\ A_n(k_3) &= \int_0^{L_3} h_n(z) e^{ik_3 z} dz \end{aligned} \quad (2.29)$$

then $|F_{mn}(k_1, k_3)|^2$ can be expressed in terms of one dimensional filter shapes as

$$|F_{mn}(k_1, k_3)|^2 = |A_m(k_1)|^2 |A_n(k_3)|^2 \quad (2.30)$$

Substituting Equations (2.29) and (2.24) into Equation (2.23) results in

$$\begin{aligned} S_w(x, z, \omega_{mn}) &= \\ &= \frac{f_{mn}^2(x, z)}{(\sigma_{\eta\omega})_{mn}^2} \int_{-\infty}^{+\infty} |A_m(k_1)|^2 |A_n(k_2)|^2 \phi(k_1, k_3, \omega_{mn}) dk_1 dk_3 \end{aligned} \quad (2.31)$$

This equation forms the basis for evaluating the acoustic, convective and low wavenumber response.

2.3.2--The Martin Plate. The Martin plate tested was the clamped plate Martin [5] used in 1976. The aluminum plate was removed from its frame, refurbished, and then epoxied to the frame using EccoBond 45 Epoxy. The plate was made from 0.034" aluminum sheet stock. The frames were constructed from 3/4" thick by 3" wide steel members which were machined to the required lengths and bolted together. The total weight of the frame was about 30 lbs., and the ratio of frame to plate mass was nearly 200:1.

The plate's physical characteristics are as follows:

Surface dimension: $L_1=0.508\text{m}$, $L_3=.0762\text{m}$;

Thickness: $8.64 \times 10^{-4}\text{m}$;

Surface density: 2.37kg/m^2 .

The modal characteristics of the plate were determined after the plate was refurbished. The same procedure as Martin [5] used was repeated. To identify the modes, the plates were driven at a single frequency by a small area acoustic drive. When a resonant response was observed, the modal pattern was determined by lightly dusting the structure with sand to produce Chladni patterns. The odd number modes from the (3,1) to the (21,1) mode were identified.

The damping factors (η_{nm}) for the plate modes were determined experimentally from decay rate measurements. The small area acoustic drive was used to excite the structure at its natural frequencies, and the vibratory response at the location of interest (in this case at the center of the plate)

was monitored with a Wilcoxon Model 91 Accelerometer. After adjusting the drive level to achieve a reasonable response signal, the excitation was shut off, and the resulting decay transient was captured on a B&K Model 7502 digital event recorder. The decay transient was then played back at a slower speed, and the decaying rms signal level was recorded on a B&K Model 2305 graphic level recorder. The damping factor (η_{mn}) is determined by the equation

$$\eta_{mn} = 1.833R_1 \tan \alpha / f_{mn} \quad (2.32)$$

where R_1 =recording rate/playback rate; α =decay angle;

f_{mn} =natural frequency (Hz).

Table 2.1 lists the experimentally determined resonant frequencies and damping factors. These are compared with those values determined by Martin [5] in 1976. The comparison is quite good.

2.3.3--The Jameson Plate. The Jameson plate tested used the same steel bar frame and similar fixture as Jameson [8] used in 1975. The steel plate used by Jameson was replaced by a stainless steel plate. The plate thickness was 24 gauge, the same as Jameson used. The plate, 22.8 inches in diameter, was flush mounted to a flat surface. The active area of the plate is a rectangle of area 500 cm^2 with side lengths in the ratio of 3 to 2, the longer side in the downstream direction. The outside part was glued to wood to provide mechanical support and damping; large steel bars (1.5"x0.75") were epoxied to the underside to make a framework defining

the active area. The steel bars clamped the plate edge, isolating the active area. The unsupported plate between the wood and the beam, about one-quarter the length of a bending wave at frequencies of interest, increased isolation from vibrations of surrounding surface by acting as a quarter-wave choke.

The plate's physical characteristics are as follows:

Surface dimension: $L_1=0.274\text{m}$; $L_3=0.183\text{m}$;

Thickness: $6.07 \times 10^{-4}\text{m}$;

Surface density: 4.92kg/m^2 .

The modal characteristics of the plate were determined using the same technique as was used for the Martin plate. The response was monitored at two locations. First, at the center of the plate to monitor the odd-odd modes. The second location was at the center of the long direction of the plate with the accelerometer moved along this midline until the anti-node of the odd, 2 modes were located. The response was monitored with a Wilcoxon Model 95 Accelerometer.

The results of the modal characteristic test are shown in Table 2.2 and compared with Jameson's [8] 1975 results. The comparison was not good. Three attempts were made to epoxy the bars to the plate. All attempts resulted in the same modal characteristics as shown in Table 2.2

III. EXPERIMENTAL FACILITIES

This section describes the experimental facilities and the experiments. In Section 3.1 the Wind Tunnel is described. The test set ups and boundary layer measurements are described in Section 3.2. The background acoustic noise measurements are described in Section 3.3, and a comparison of noise in the M.I.T. Facility is made with the BBN Facility in Section 3.4.

3.1 M.I.T. Low Noise, Low Turbulence Wind Tunnel

The experiments were conducted in the M.I.T. low noise, low turbulence wind tunnel using the equipment of the M.I.T. Acoustics and Vibration Laboratory. The wind tunnel is shown in Figure 3.1 and is described in Hanson [13]. The wind tunnel consists of an intake, a flow straightening section, a test section enclosed in an air tight blockhouse, a muffler diffuser, and a variable speed centrifugal blower.

This wind tunnel has been used for low wavenumber measurements by Martin [5] and by Moeller et al. [6]. The wind tunnel has been modified since the experiments of Moeller et al. The semianechoic treatment in the blockhouse has been changed since the previous experiments were conducted. The new treatment consists of a 4 inch blanket of urethane foam covering the walls, floor and ceiling of the blockhouse. A set of 4 inch foam blocks was then draped at random on the walls, floor, and ceiling, with a set of 2 inch foam blocks draped randomly over the 4 inch blocks. This change in semi-anechoic treatment did not significantly affect the low wavenumber measurement program.

The wind tunnel was operated in the free jet mode. This was done to isolate the wavenumber filters in the test sections from noise propagating upstream from the blower. The isolation was provided by allowing the noise to propagate into the blockhouse and be absorbed by the semianechoic treatment.

3.2 Boundary Layer Tests

3.2.1--Test Boundary Configurations. The low wavenumber measurements were conducted in three different test configurations. The first configuration was to test in a hard walled duct using the same ducting as Martin [5] and Moeller et al. [6]. This test configuration is shown in Figure 3.2. This configuration was used for both structural filtering tests and microphone array tests.

The next configuration tested was a lined duct. The duct was lined with a 1 inch thick blanket of urethane foam to attenuate the cross modes propagating in the duct. The foam is faced with a coating to provide a smooth surface to the flow. This configuration was used only for structural wavenumber filtering tests.

The final configuration tested was similar to the test configuration used by Jameson [7,8] at Bolt, Beranek & Newman and is shown in Figures 3.3 and 3.4. The wind tunnel was operated in the wall jet configuration. The walls of the duct were removed and only the bottom remained in place. The boundary layer on the bottom wall of the ducting was allowed to develop naturally. Tests were done at two different locations in this configuration. The first was 1.34 meters

downstream of the contraction exit plane. The second was 0.45 meters downstream of the contraction exit.

The open duct configuration produced the best results. The hard walled duct allowed cross duct mode to propagate upstream from the blower. The lined duct was thought to generate as well as absorb high-frequency noise. The open duct took greatest advantage of the blockhouse semianechoic treatment. These conclusions are in agreement with Jameson [7].

The results presented in this report will be only for two different locations of the open duct configuration.

3.2.2--Boundary Layer Profiles. The boundary layer properties were measured for speeds ranging from 15 m/s to 40 m/s for each configuration tested. The boundary layer profiles were measured at the center of the test plate using a United Sensors 0.035" total head tube and a static tap on the test section wall. The pressure differences were measured using a Validyne DP-15 pressure transducer that was calibrated against a Beta micromanometer. The boundary layer parameters displacement, thickness, δ^* , and momentum thickness, θ , were determined by integrating the boundary layer profiles. The shape factor $H = \delta^* / \theta$ was then calculated. By fitting the boundary layer profiles to a law of the wall, the friction velocity, v_* , was determined from the slope of the logarithmic overlap region of the law of the wall. The boundary layer properties are summarized in Table 3.1

The outer mean flows of the boundary layers follow quite closely the velocity-defect law derived from Cole's Law of the Wake. This law may be written [14]

$$u^+ = 1/K \log_e y^+ + B + \Pi/KW(y/\delta) \quad (3.1)$$

where $W(g/\delta) \cong 2\sin^2(\frac{\Pi}{2} \frac{y}{\delta})$ (3.2)

The wake parameter $\Pi=0.55$ for the zero-pressure-gradient boundary layer, $K=0.4$ is the von Karman universal constant, and the constant $B=5.0$. The agreement between a typical measurement and Equation (3.1) is shown in Figure 3.5. The agreement is good.

3.2.3--Single Point Wall Pressure Spectra. The single point wall pressure spectra were measured for each test configuration. The measurements were performed using a B&K 1/8" microphone with a 1/32" pinhole cap. The microphone was flush mounted at the center of the measurement location. The results were nondimensionalized on the previously determined boundary layer properties and are compared to Burton [15] and Blake [16,17] in Figure 3.6.

The single point wall pressure spectra are a measurement of the convective ridge levels at a particular frequency. The small area microphone does not attenuate the signal very much until the point where $\omega R/u_c=1.0$ is marked on the plots. The single point wall pressure spectrum levels measured this way are used to make estimates of the convective ridge contamination of the wavenumber filters.

3.3 Measurement of the Background Acoustic Noise

An accurate measurement of the background noise in the test facility is necessary to insure the quality of the low wavenumber data. The test set up used to measure the background noise in the blockhouse is shown in Figure 3.7. The levels were determined using a B&K 4144 1 inch microphone. The current measurements are compared to those of Martin [5] for the same test configuration in Figure 3.8. The noise in the blockhouse has not changed much since the earlier tests.

The wavenumber filtering behavior of the 1 inch flush mounted B&K Type 4144 microphone was used to provide an estimate of the acoustic noise at the measurement location. The measurement technique is the same as the single point wall pressure measurement. The 1 inch microphone was flush mounted using a cap that was designed and used by Farabee and Geib [3] in their experiments. The microphone's diaphragm was exposed such that it could be flush mounted in the test section.

The large area microphone is essentially a low pass filter in wavenumber. The typical single point spectrum levels measured this way are shown in Figure 3.9 for the wall jet test configuration and a test speed of 15 m/s. The low frequency behavior shows the response of the microphone to the convective ridge. The convective ridge is at $k_c = 2\pi f / u_c$. The microphone rapidly attenuates the convective ridge information by averaging it out over the face of the microphone. What is left at the higher frequencies, where the single point spectrum changes

levels slowly, is made up of background acoustic noise and the low wavenumber components of the wall pressure spectrum.

A pair of microphones were used in the background noise test configuration. The HP5425 Analyzer was used to compute a normalized cross-spectrum between the pair of flush mounted microphones. The pressure spectrum levels are shown in Figure 3.9 and are the same at both measurement locations. The separation between the microphones was 2.12 inches. The normalized cross-spectrum is shown in Figure 3.10. The coherence between the two microphones is shown in Figure 3.11. In the region where the pressure spectrum levels are flat the coherence between the two microphones is between 0.5 and 0.7. In this region the phase of the normalized cross-spectrum shows a linear phase delay that corresponds to acoustic wave propagating upstream from the blower. In Figure 3.12 the single point spectrum for a speed of 40 m/s is shown and in Figure 3.13 the corresponding normalized cross-spectrum is shown. Because of the higher speed, the convective region of the single point pressure spectrum extends to higher frequency than those of the lower speed case. The phase of the normalized cross-spectrum shows two distinct regions of linear phase delay. In the low frequency region is a linear phase delay that corresponds to turbulent eddies convecting downstream at a major fraction of the freestream velocity. Conversely, in the high frequency region one can see a phase delay of the opposite sense corresponding to an acoustic wave propagating upstream from the blower. The combination of the coherence between the pair of

microphones at the higher frequencies and the phase delay corresponding to an acoustic wave propagating upstream, leads to the interpretation of the pressure spectrum levels at the higher frequencies to be primarily acoustic in nature.

The acoustic levels at the test location determined by the large area flush mounted transducer are compared to the background noise measurements for the same test conditions with the result shown in Figure 3.14. The acoustic levels at the wavenumber filter location are more than 10 dB louder than the blockhouse noise levels. The blockhouse noise levels underestimate the acoustic contamination of the wavenumber filter data. This is due to the acoustic source downstream in the blower being much more directive than previously anticipated (see section 4.3.4 for further discussion).

3.4 Comparison of the M.I.T. Facility with the Bolt, Beranek & Newman Facility.

The current background noise and single flush mounted microphone measurements are compared to those made by Jameson [7] at Bolt, Beranek and Newman, Inc. The Jameson data is from Figure 10 of BBN Report No. 1937 at a speed of 55 ft/s or 16.8 m/s. Figures 3.15 and 3.16 compare the current measurements at 15 m/s and 20 m/s with the Jameson measurements.

The scaling on Figures 3.15 and 3.16 is the same as Jameson used. The length scale for the Strouhal parameter is a fixed quantity equal to 0.139 inches, which happens to be the average value of the displacement thickness for Jameson's boundary layers. That the length scale is the average value of

the displacement thickness was just a matter of choice. Blake and Chase [2] used the microphone radius for the length scale.

Figures 3.15 and 3.16 indicate that for the flush mounted microphones, above a Strouhal number of 6, about 2.5 kHz, the levels are 3-4 dB higher at the M.I.T. Facility. The region above 2.5 kHz (see Section 3.3) is the region in which the flush mounted microphone is thought to be measuring acoustic waves propagating upstream from the blower in the M.I.T. Facility. The background noise measure, although sensitive to position in the blockhouse and perhaps not indicative of what is happening in the flow, shows the M.I.T. Facility to be as quiet or slightly quieter than the BBN Facility.

IV. WAVENUMBER FILTERS MEASUREMENTS

4.1 Experimental Source of Excitation

As discussed in Section 2.1 and shown in Figure 2.1, at a given frequency, wavenumber-frequency wall pressure spectrum consists of convective, acoustic and low wavenumber components. A reasonable model for the wavenumber-frequency spectrum is to assume that the three components are statistically independent and can be written as a sum

$$\Phi(\underline{k}, \omega) = \Phi(\underline{k}, \omega)_{\text{conv.}} + \Phi(\underline{k}, \omega)_{\text{acoustic}} + \Phi(\underline{k}, \omega)_{\text{low } k} \quad (4.1)$$

Equation (4.1) can be used with Equation (2.23) to obtain the total structural response as a sum of convective, acoustic and low wavenumber responses. The wavenumber filters are designed to reject or minimize the acoustic and convective contamination. To ensure that the measured response is dominated by the wavenumber contribution, it is important to estimate the magnitude of response due to acoustic and convective excitation. If the measured response exceeds the predicted contaminating levels by a sufficient amount, it is appropriate to use the measured data to determine the actual magnitude of $\Phi(\underline{k}, \omega)_{\text{low } k}$.

The estimate of the contamination levels is not trivial. The levels of the convective contamination are only known near the convective ridge, and the response of the filters (plates or microphones) is not accurately known at high wavenumbers where the convective ridge is located. In addition, because of the directivity of the acoustic contamination source (see

Section 3.3), a blockhouse microphone will not measure the proper levels and a single flush mounted microphone will be convectively contaminated.

Because of the above difficulties, this report will not include a quantitative estimate of the response due to the contaminations. The levels measured will be upper bound to the low wavenumber levels. Qualitative estimates of the contamination will be given for the microphone array and the plates in Section 4.2 and 4.3 respectively. Array steering techniques have been used to determine the response of a single microphone to convective and acoustic contaminations. This has been done only in limited frequency range and only at 15 m/s. The results can be found in Appendix B. Estimates of the contaminated response have been done by earlier investigators [2,3,5,6,7,8] on the filters used in this measurement program, and contamination estimates can be found in the literature.

4.2 Microphone Array Measurements

4.2.1--Alternating Phased Array Measurements. Measurements using the microphone array were performed at 15, 20, 25, 30, 35 and 40 m/s. Data was obtained with a single 1 inch microphone, a 1/8 inch microphone with a 1/32 inch pinhole cap, and with the array of six microphones operating in the common phase mode and the alternating phase mode for each speed using uniform, Chebyshev and binomial shading.

Figure 4.1 shows a comparison of the wall pressure measurements obtained with a single 1/8 inch microphone with pinhole cap, a 1 inch microphone, and the alternating phased array with uniform shading at 15 m/s. In addition, the block-house noise measurement is shown. The ordinate in Figure 4.1 is the mean square pressure in a 1 Hz frequency band and the abscissa is frequency.

Before discussing the response of the array, it is helpful to study the relationship between the peak of the array sensitivity (the major lobe) and the turbulent and acoustic pressure spectra as shown in Figure 4.2. The major lobe is at a fixed wavenumber k_{10} . The pressure measurements are made in frequency space. As the frequency increases, the array encounters the convective peak first at $\omega = k_{10}u_c$. As frequency is further increased, the low wavenumber region is encountered next, and finally the acoustic region at $\omega \geq k_{10}c_o$. The same relation is also valid concerning the array nulls and aliasing lobes.

4.2.2--The Convective Region--Alternating Array.

Returning to Figure 4.1, the 1/8 inch microphone with pinhole cap can be assumed to be indicative of the convective ridge levels at a particular frequency. The attenuation of the convective ridge by a single 1 inch microphone can be readily seen by comparing the two microphones.

Referring to Figure 3.10, the phase relation between two 1 inch microphones at 15 m/s, the microphones respond

strongest to the convective ridge below 1 kHz, between 1 kHz and 2.5 kHz the phase denote a transition region, and above 2.5 kHz the response is primarily to acoustic excitation coming from downstream. A similar phenomenon can be observed by comparing the slope of the 1 inch flush mounted microphone with the blockhouse microphone in Figure 4.1. The slopes become almost parallel when the flush mounted microphone is responding to the acoustic excitation.

Next observing the alternating phased array curve on Figure 4.1 and starting from the low frequencies, a peak occurs at 175 Hz. This peak is the coincidence of the major lobe at $k=2.9 \text{ in}^{-1}$ (see Figure 2.7) with the convective peak. The next peak at 525 Hz is due to the coincidence of the first aliasing lobe at $k_1=8.8 \text{ in}^{-1}$ with the convective peak. Because of the physical size of the microphone, it was not possible to space the microphones to cancel the first aliasing lobe as described in the ideal case in Section 2.2.2. The nulls in the array response have been smoothed out by the response of the major lobe and first aliasing lobe to the convective ridge. All that can be seen is the dip between the two main lobes' response.

Figure 4.3 shows the coherence between the array response and a single 1 inch microphone in the array. The response of the main lobe and first aliasing lobe is readily evident in this figure with the main lobe having a coherence about 0.7 and the first aliasing lobe has a coherence about 0.5.

As the flow speed is increased, the coincidence of the array main lobes with the convective ridge occurs at higher frequencies. This can be clearly seen in Figure 4.4 where the array response at 40 m/s is compared with the array response at 15 m/s. In addition, the first null in the acoustic region which is evident at 15 m/s at 2.2 kHz is smoothed over by the convective region. This is further substantiated by referring to Figure 3.13, the phase relation between two microphones at 40 m/s. The convective region is clearly more evident and extends to about 2 kHz, with the transition region before the acoustic region being reduced.

The above figures indicate that to minimize the convective contamination, data should be obtained at the lowest speeds. The lowest speed at which reasonable data was obtained (i.e., where the array response was at least 6 dB above the electronic noise floor) was 15 m/s. The least convectively contaminated data was obtained in the 15 to 25 m/s speed range.

Some additional information concerning the single microphone response to the convective ridge can be found in Appendix B. In this appendix, results of steering the array to measure the 1 inch microphone response to the convective ridge at 15 m/s is discussed.

4.2.3--The Acoustic Region--Alternating Array. The test setup shown in Figure 3.7 was used to determine the acoustic sensitivity of both the structural wavenumber filters and the microphone arrays. The loudspeaker was located upstream

of the wind tunnel inlet. A two point normalized cross-spectrum was computed for this case. The excitation was white noise and there was zero flow velocity. The result is shown in Figure 4.5. The normalized cross-spectrum shows a flat magnitude and a linear phase delay. The coherence is good between the two microphones. The result is approximately an acoustic wave travelling down the test section. This setup was then used to determine the acoustic sensitivities of both types of wavenumber filters.

When comparing the phase relation in Figure 4.5 with the phase relation at a flow of 15 m/s in Figure 3.10 and the phase relation at a flow of 40 m/s in Figure 3.13, the slope at frequencies above 2.5 kHz of the flow curves is the negative of the acoustic curve. Both show a linear phase with the acoustic test indicating a plane wave propagating downstream and the flow tests indicating a plane wave propagating upstream.

The test setup shown in Figure 3.7 was used to calibrate the array by computing the transfer function from one of the array elements to the array output. The acoustic check of the alternating phased uniformly shaded array was shown in Figure 2.7 and the major characteristics were described in Section 2.2.3.

Returning to Figure 4.1, and observing the array response at 15 m/s, as the frequencies increase beyond the convective region, the array dips below the blockhouse noise measurements.

Two minimas are observed at 2200 Hz and 4200 Hz corresponding to the coincidence of the two nulls on either side of the side lobe before the major lobe of the array at $k_1 = 1.02 \text{ in}^{-1}$ and 2.04 in^{-1} and the sonic line $\omega = k_1 c_o$. These minima are more evident in the coherence plot at 15 m/s shown in Figure 4.3. The coherence at the two minimas or the nulls in the acoustic check, is practically zero.

After the two minimas, the array response increases and a maxima occurs at 6.3 kHz. This maxima is due to the coincidence of the major lobe with the sonic line. This maxima asymptotes with the single 1 inch microphone.

Again the fact that the frequency where the array responds essentially to an acoustic plane wave asymptotes to the single microphone response and coherence of the array is practically zero at the nulls of the plane wave acoustic check is another indication that the single microphone above 2.5 kHz is responding to predominately an acoustic plane wave travelling upstream.

In Appendix B the array was acoustically steered during flow at 15 m/s for a plane wave propagating upstream. The results showed that the steered array levels were very close to the single microphone levels at frequencies above 2.5 kHz. This indicates that the single microphone is measuring primarily acoustic plane waves propagating upstream at frequencies above 2.5 kHz. For more detail, see Appendix B.

4.2.4--The Low Wavenumber Region--Alternating Array. The low wavenumber region in the frequency response of the array occurs between the first aliasing lobe response of the convective region and the main lobe response of the acoustic region. The best frequencies to extract the low wavenumber data for the alternating phased uniformly shaded array would be at the two nulls, 2200 Hz and 4200 Hz, at speeds between 15 to 25 m/s. These frequencies have the effect of spatial averaging attenuation of the convective ridge and the array minimization of the acoustic contamination.

The low wavenumber region, except possibly at the two nulls, is dominated by the side lobe response. As discussed in Section 2.2.2, the side lobes can be suppressed by using a different type of array shading. Figure 4.6 shows a comparison of the alternating phased array response for uniform shading, Chebyshev shading and binomial shading. Figure 4.7 shows the coherence of the shaded arrays with a single microphone in the array. As was discussed in Section 2.2.2, the Chebyshev shading reduces the minor lobe with the minimum widening of the major lobe, and the binomial shading totally eliminates the minor lobe but greatly increases the major lobe's width. These effects are most evident in the acoustic region. For the Chebyshev shading, the minor lobe between the two nulls has been virtually eliminated. The coherence at this location is almost zero. Low wavenumber data can therefore be taken

anywhere in this region. The binomial shading, although it eliminates the minor lobe, increases the width of the major lobe so that the sonic response of the major lobe contaminates the second null and the minor lobe region between the first and second null. Only in the vicinity of the first null can good low wavenumber data be obtained.

4.2.5--The Common Phased Array. The common phased array has its major lobe response centered at $k_1=0$. Referring again to Figure 4.2, the main lobe occurs at the very low frequency for both the convective ridge and the sonic line $\omega=kc_0$. If as assumed, the acoustic contamination is primarily plane wave so that there are no trace waves, then at higher frequencies there should be minimal acoustic contamination.

Figure 4.8 shows a plot of the common phased array. The initial peak at the lower frequencies is masked because of use of a high pass filter at 100 Hz. The first aliasing lobe is coincidental with the convective ridge near 375 Hz. Two minimas occur which are the nulls in the acoustic response. They occur at approximately 2.4 and 4.2 kHz. Their location is more evident in Figure 4.9 showing the coherence of the common phased array. It is at these two locations where the low wavenumber measurement were taken.

4.3 Plate Measurements

4.3.1--The Martin Plate. Martin [5] made mode shape measurements of selected modes of all his spatial filters. The mode shapes were Fourier transformed (see Equation 2.29)

by numerical techniques to obtain the wavenumber filter shapes $|\bar{A}_m(\bar{k})|^2$. A reprint of the wavenumber filter shape measured and computed by Martin [5] for the (15,1) mode is shown in Figure 4.10. Also on Figure 4.10 is the curve for the envelope of the peaks for the ideal clamped beam. The comparison between the two is good.

As expected, the plot is characterized by a major lobe which peaks near the characteristic wavenumber \bar{k}_m of the mode and a series of side lobes at higher and lower wavenumbers. On Figure 4.10, in the high wavenumber vicinity, is indicated the convective wavenumber \bar{k}_c for a free stream velocity of 40 m/s. At this point the wavenumber response is more than 40 dB down from the main lobe. However in the acoustic region (the lower wavenumbers) the wavenumber response is only 20 dB down from the main lobe. This indicates that the plates are a better rejector of convective contamination than they are of acoustic contamination.

Measurements using the plate filters were performed at 15, 20, 25, 30, 35 and 40 m/s. A typical plate acceleration spectrum excited at 40 m/s is shown in Figure 4.11. The acceleration was measured at the center of the plate. The spectrum exhibits sharp resonances corresponding to the odd numbered modes ranging from (3,1) mode to the (21,1) mode. The fundamental mode does not appear in a distinct form. Its response would be expected to be severely limited by radiation damping, and it is also quite likely that a model overlap

situation exists between the fundamental and the (3,1) mode. Above 4 kHz the third order lateral modes appeared and created another modal overlap situation. The intermediate modes (i.e., 7,1 mode through the 17,1 mode) are well separated in frequency and have peak levels which are well above the observed background levels. These are the modes that were used to make low wavenumber measurements.

4.3.2--The Jameson Plate. The Jameson plate was designed to have higher order lateral modes in the frequency range of interest. Unlike the Martin plate, the lateral filter shape $|A_n(k_3)|^2$ major lobe is not always centered at $k_3=0$, but is located at the characteristic wavenumber k_n . As indicated in Equation (2.30), the total wavenumber response can be expressed as a product of the one dimensional wavenumber responses. Each one dimensional wavenumber response is similar to the one shown in Figure 4.10 for the Martin plate.

The exact shape of the wavenumber response of the Jameson plate is not known since the mode shape measurements were not made. As indicated in Section 2.3.3, the measured natural frequencies for a particular mode were not as expected. When compared to approximated calculated values, the natural frequencies occurred between the case for clamped edges and the case for simple supported edges, while the values measured by Jameson [8] in 1975 approached the clamped condition. The ratio between the calculated and measured natural frequency for each mode was not a constant as would be expected for a difference in plate thickness or material properties.

It was assumed that the boundary conditions were not met because of a poor bond. As mentioned previously, three attempts were made to achieve the desired boundary condition (one attempt was made at an outside facility); all attempts had the same results. The epoxy used was the same as Jameson used. The plate material however was stainless steel and not steel. It is not known whether the plate material would make a difference or not. Jameson [8] did have more difficulty with a brass plate than he did with the steel plate.

Low wavenumber measurements were made on the Jameson plate at 15, 20, 25, 30, 35 and 40 m/s. Figures 4.12 and 4.13 show a typical acceleration spectrum for the two locations monitored. The spectrum in Figure 4.12 is when the plate was monitored at the center of the plate and the response of the odd-odd modes were measured. The spectrum in Figure 4.13 is for the case where the accelerometer was at the center of the long direction of the plate and moved along this mid-line until the anti-node of the odd, 2 modes were located.

Model overlap is a more serious problem for the Jameson plate than for the Martin plate. The Jameson plate exhibited the same limitation in the lower frequencies due to radiation damping and modal overlap, but the problem of modal overlap existed at all frequencies because of the addition of higher order lateral modes. An attempt was made to select modes that were well separated for the low wavenumber measurements. The modes selected are indicated on Figures 4.12 and 4.13.

4.3.3--Plate Convective Response. As mentioned in Section 4.1, because of uncertainties about the shape of the convective ridge and the response of low wavenumber filters to high wavenumber excitation, estimates of convective contamination are not trivial and only qualitative estimates will be provided.

Martin [5] predicted by calculation that his membranes and s-c-s-c plate exhibit a flow speed dependence of $(U_\infty)^9$ while the clamped plate has $(U_\infty)^{11}$ dependence. This means, in general, the convective response will become increasingly significant at the higher flow speeds. Martin [5] also indicated from calculation that the clamped plate will have less convective response by a factor $(\bar{k}_m/\bar{k}_c)^2$ than the s-c-s-c plate, where the (\bar{k}_m/\bar{k}_c) in the experiments range from 0.07 to 0.25. The clamped plate would therefore be expected to have significantly less convective response than the s-c-s-c plate.

Martin [5] predicted the levels of the plate's convective response and compared those with his measured response. The convective estimates of the clamped plate were found to be 10 to 30 dB below the measured levels and were not considered a significant contaminant. The s-c-s-c plate did have some predicted responses within 4 dB of the measured responses at 50 m/s. These data points were discarded. Comparing Martin's [5] measured results for the clamped plate with the measured results for the s-c-s-c plate shows that the s-c-s-c plate measures lower values (even when corrected for differences in damping and frequency) than the clamped plate. This indicates

that convective response is not the significant contaminant for the s-c-s-c plate.

Jameson [8] concluded similar results concerning convective contamination. The present data for the Jameson plate is also assumed not to be seriously convectively contaminated even though the plate boundaries may be simply supported. This assumption is made based on comparison of the two Martin plates.

4.3.4--Plate Acoustic Response. The wavenumber response of a single mode, determined by Martin [5] and shown in Figure 4.10 indicated that the plate responds better to the low wavenumber acoustic waves than the high wavenumber convective waves. Both Martin [5] and Jameson [8] determined their plate's acoustic response by the same method. An acoustic source was used to insonify the blockhouse, similar to the test setup shown in Figure 3.7, and the coupling between the sound measured by a microphone located outside the flow and the plate response was calculated to determine the plate's acoustic sensitivity. The level of the acoustic contamination was estimated using the blockhouse microphone during the flow tests. From these results, the acoustic contribution to the modal excitation was estimated.

Jameson [8] kept only the data for which the acoustic contribution was at least 8-10 dB below the measured data. Martin [5] calculated acoustic contribution typically fell below, but reasonably close to, the measured levels. Data points that were less than 4 dB below the measured data were discarded.

The acoustic contamination estimates were repeated for both the Martin plate and the Jameson plate in the open jet configuration. The results were similar for both plates. The acoustic contamination estimates typically fell below, but reasonably close to, the measured levels. Very few of the acoustic estimates, however, were 8-10 dB below the measured levels. Also, at the lower flow speeds, where there is less convective contamination, more modes had acoustic contamination estimates that exceeded the measured levels.

The accuracy of the acoustic contamination estimates are highly suspect. As indicated in Section 3.2.3, the primary acoustic source located downstream in the blower is thought to be more directive than previously anticipated. A rough estimate of the directivity of the acoustic source can be calculated by modeling the source as an equivalent circular cylinder with an area equal to the area of the duct. This assumes that the acoustic contamination is primarily plane wave.

The directivity pattern for a circular piston [18] is

$$D(\theta) = \frac{2J_1(k a \sin \theta)}{k a \sin \theta} \quad (4.2)$$

where θ is the polar angle from the axis of the cylinder, a is the radius of the cylinder. Values of the directivity function, $2J_1(x)/x$, are plotted as a function of x in Figure 4.14. It can be observed from the plot that the curve has zero crossings at $x=3.83, 7.02$, etc.

For a duct 15"X15", the equivalent circular radius is 8.5 inches. Figure 4.15 plots the polar angle, θ , versus frequency for directivity pattern 3 dB down, 6 dB down, and the first null for such a duct. The directivity of the acoustic contamination, especially in the higher frequencies, is obvious from the plot.

The speaker used to insonify the blockhouse is also directive. However, its directive pattern is probably different than the acoustic contamination occurring during flow and is dependent on its location. Because of the differences in directivity patterns, the plate could respond quite differently to the same level measured by the blockhouse microphone for the two cases. Figure 4.16 visually shows how the blockhouse microphone could respond differently to two sources with different directivity patterns. As an example, Table 4.1 shows the results of two acoustic sensitivity tests with the speaker in two different locations. The first test on the speaker was located in the inlet of the diffuser (see Figure 3.1). In the second test, the speaker was located at an inlet of the wind tunnel (see Figure 3.7). As the table indicates, for some modes there could be quite a difference.

In light of the above, the method for determining the plates' acoustic response can only be considered an indication of the acoustic contamination, and no real values can be assigned.

As mentioned in Section 4.3.3, Martin's [5] s-c-s-c plate resulted in lower levels than the clamped plate. In addition, the sensitivity test indicated that the s-c-s-c plate typically responded less to acoustic excitation than the clamped plate. This is an indication that acoustic contamination is still a major contributor to the total response of the plate.

4.3.5--Plate Low Wavenumber Response. The peaks of the modal response shown in Figure 4.11 for the Martin plate and Figures 4.12 and 4.13 for the Jameson plate are assumed to be low wavenumber data points. The spectrums were measured at analyzer bandwidth greater than the plate modal bandwidth. Corrections were performed on the peak values to account for the difference in bandwidths. Data was obtained at various analyzer bandwidths to evaluate the correction method. Spectral levels for various analyzer bandwidths after correction generally differ by less than 2 dB.

No corrections were made to the low wavenumber data to account for acoustic or convective contamination. However, only those modes thought to have good modal separation were used.

V. LOW WAVENUMBER RESULTS

5.1 Microphone Low Wavenumber Results

5.1.1--Method of Calculating Low Wavenumbers. The array output at any frequency, as shown in Equation (2.15) represents an integration over wavenumber space of the array response and the spectral density. If the spectral density is assumed to be independent of \underline{k} for the frequencies of interest (2), then from Equation (2.15)

$$\Phi_M(\omega) \cong \Phi(\underline{k}, \omega)_L \int_{-\infty}^{+\infty} \int |W(\underline{k})|^2 d\underline{k} \quad (5.1)$$

Blake and Chase [2] performed an integration on a four microphone array with uniform shading to obtain an estimate for

$$\int_{-\infty}^{+\infty} \int |W(\underline{k})|^2 d\underline{k} = 37 \text{ in}^{-2} \quad (5.2)$$

The assumption used in obtaining Equation (5.1) is the main contribution to the array output comes from the major response lobe. Since the six element array is similar to that of Blake and Chase [2], Equation (5.2) can be used by modifying it to account for the difference in bandwidth of the main response lobe. The modified version of Equation (5.2) is then [3]

$$\int \int |W(\underline{k})|^2 d\underline{k} = \left(\frac{37.0}{B}\right) \left(\frac{4}{N}\right) \text{ in}^{-2} \quad (5.3)$$

where $B = 1.0$ for Uniform shading,
 $= 1.53$ for Chebyshev shading,
 $= 2.0$ for Binomial shading,
 $N =$ the number of microphones;

B was estimated by comparing the main lobe width in the acoustical calibration for various shadings.

Then substituting Equation (5.3) into Equation (5.1) and solving for $\Phi(\underline{k}, \omega)_L$

$$\Phi(\underline{k}, \omega)_L = \frac{\Phi_m(\omega) BN}{(4)(37)} \quad (5.4)$$

The values for $\Phi_m(\omega)$ are selected as discussed in Section 4.2.4.

5.1.2--Alternating Phased Results. The measured levels for the spectral density in the low wavenumber region are presented in nondimensional form. The first non-dimensional form presented is for the ordinate $\Phi(\underline{k}, \omega)_L U_\infty / q^2 \delta^{*3}$ and the abscissa is the Strouhal number $S = \omega \delta^* / U_\infty$. This is the same nondimensional form used by Farabee and Geib [3] and Martin [5].

Figure 5.1 shows the results for the alternating phased uniform shaded array in position 1 (see Section 3.2.1) located 1.34 m downstream from the contraction exit plane. The plot shows the results at various speeds. Two points were measured, each corresponding to the nulls in the acoustic response. The important thing to notice is how the data tends

to curve upward at the higher speeds, especially for the low frequency data points where the convective ridge encroaches the first null region. The second point to notice is that the data from the first null region (i.e., of the two data points obtained for a particular speed, the one with the lower Strouhal number) has a different slope than the data from the second null region. Remember the data from the second null lies strictly in the acoustic region while the data from the first null lies in the transition region (see Sections 4.2.2 and 4.2.3).

Figure 5.2 shows a comparison between the data measured at position 1 and the data measured at position 2 for the alternating phased uniformly shaded array. The main difference between the two locations is the boundary layer displacement thickness. The average displacement thickness at position 1 is 0.21 inches, while the average displacement thickness for position 2 is 0.09 inches. As shown on the figure, the nondimensional form used, having a strong dependence on boundary layer thickness, does not collapse the two different sets of data. The two sets of data do have parallel slope indicating (as will be shown in Section 5.3) a weak dependence on displacement thickness as a length scale.

Figure 5.3 shows a comparison between the data for the three different shadings for the alternating phased array measured at position 1. Both the Chebyshev shading and the binomial shading produces slightly lower results than the uniform shading.

Table 5.1 tabulates the raw data for all the various cases measured using the alternate phased array.

5.1.3--Common Phased Array. Figure 5.4 shows a comparison between the common phased array data and the alternating phased array data at position 1. The alternating phased array typically gave lower results than the common phased array.

Table 5.2 tabulates the raw data for all the various cases measured using the common phased array.

5.2 Plate Low Wavenumber Results

5.2.1--Method of Calculating Low Wavenumber. If the excitation $\Phi_p(k, \omega)$ is reasonably constant in the low wavenumber region, the integral of Equation (2.31) will be dominated by contributions from the major lobes of the wavenumber filter shapes, $|A(k_1)|^2$ and $|A_n(k_3)|^2$. The major lobes of the mode shapes $|A_m(k_1)|^2$ and $|A_n(k_3)|^2$ are located at the characteristic wavenumbers k_m and k_n respectively. For the plates used, the wavenumber bandwidths are sufficiently narrow to allow the filter shapes to be approximated by Dirac delta functions at $k_1 = \pm k_m$ and $k_3 = \pm k_n$. Since

$$\int_{-\infty}^{+\infty} |A(k)|^2 dk = 2\pi ,$$

the approximations are

$$|A_m(k_1)|^2 = \pi[\delta(k_1 - k_m) + \delta(k_1 + k_m)]$$

$$|A_n(k_3)|^2 = \pi[\delta(k_3 - k_n) + \delta(k_3 + k_n)] \quad (5.5)$$

The substitution of Equations (5.5) into Equation (2.31) yields

$$S_w(x, z, \omega_{mn}) = \frac{2\pi^2 f_{mn}(x, z)}{(\sigma\eta\omega^2)_{mn}} [\Phi_p(k_m, k_n, \omega_{mn}) + \Phi_p(-k_m, k_n, \omega_{mn})] \quad (5.6)$$

It was assumed when computing Equation (5.6), that because of symmetry in the lateral dimension

$$\Phi_p(+k_m, k_n, \omega_{mn}) = \Phi_p(+k_m, -k_n, \omega_{mn}) \quad (5.7)$$

For the plate experiments, it is the acceleration response which is measured. Since $S_a(x, z, \omega_{mn}) = \omega_{mn}^4 S_w$
 $S_a(x, z, \omega_{mn}) = \omega_{mn}^4 S_w(x, z, \omega_{mn})$, the acceleration spectral density at resonance is given by

$$S_a(x, z, \omega_{mn}) = \frac{2\pi^2 f_{mn}^2(x, z)}{(\sigma\eta)_{mn}} [\Phi_p(k_m, 0, \omega_{mn}) + \Phi_p(-k_m, 0, \omega_{mn})] \quad (5.8)$$

Equation (5.6) and (5.8) provide the basis for the experimental measurements of $\Phi_p(\underline{k}, \omega)$ in the low wavenumber region. Once the plate has been calibrated by determining

its physical parameters and resonance characteristics, it is possible to determine the level of the excitation $\Phi_p(\underline{k}, \omega)$ from displacements or acceleration measurements. As the equation indicates, there is no way to separate the component of excitation at $k_1=k_m$ from that at $k_1=-k_m$. To be consistent with Martin [5], both terms will be retained by defining

$$P(k_1, k_3, \omega) = \Phi_p(k_1, k_3, \omega) + \Phi_p(-k_1, k_3, \omega) \quad (5.9)$$

Substituting Equation (5.9) into Equation (5.8) and solving for $P(k_m, k_n, \omega)$ yields

$$P(k_m, k_n, \omega) = \frac{(\sigma\eta)_{mn}^2}{2\pi^2 f_{mn}^2(x, z)} S_a(x, z, \omega_{mn}) \quad (5.10)$$

In all experiments the response was measured at the anti-node of a particular mode. From analytical mode shapes [5], it was found that at the anti-node

$$\begin{aligned} f_{mn}^2(x, z) &\cong \frac{5.044}{L_1 L_3} && \text{for } \begin{matrix} n = 1 \\ m \geq 3 \end{matrix} \text{ or } \begin{matrix} n \geq 3 \\ m = 1 \end{matrix} \\ &\cong \frac{4.554}{L_1 L_3} && \text{for } \begin{matrix} n = 2 \\ m \geq 3 \end{matrix} \text{ or } \begin{matrix} n \geq 3 \\ m = 2 \end{matrix} \\ &\cong \frac{4}{L_1 L_3} && \text{for } \begin{matrix} n \geq 3 \\ m \geq 3 \end{matrix} \end{aligned} \quad (5.11)$$

5.2.2--Martin Plate Results. Figure 5.5 shows the results of the Martin plate located in position 1 for various speeds. Again there is a slight upturn of the data at the higher speeds, although not as pronounced as the microphone data. The plate data is thought to be more convectively contaminated at the higher speeds and more acoustically contaminated at the lower speeds.

Figure 5.6 shows a comparison between the data measured at position 1 and the data measured at position 2. Again the non-dimensional form does not collapse the data very well.

Table 5.3 tabulates the raw data for all the various cases measured using the Martin plate.

5.2.3--Jameson Plate Results. Figure 5.7 shows the results of the Jameson plate at position 1 for various speeds. The Jameson plate data is slightly lower than the Martin plate data but still within each plate's scatter. One possible reason for the slightly lower results of the Jameson plate is additional rejection of acoustic contamination by the higher order lateral modes. The (3,3), (5,3) etc. modes have corner mode [19] cancellation while the (1,5), (1,7), etc. modes have only edge mode cancellation.

Table 5.4 tabulates the raw data for all the various cases measured using the Jameson plate.

5.3 Effect of Boundary Layer Thickness on Low Wavenumber Results

As indicated in Figures 5.2 and 5.6, the use of boundary layer thickness as a length scale does not collapse the data very well. Comparing the raw data at the two positions in Table 5.1 and 5.3, one notices that the data does not vary significantly from one position to another. From this it was decided that a length scale that does not vary from position to position would be more suitable.

As an initial trial, an arbitrary constant length scale was chosen. The length scale chosen was 0.2 inches (the average boundary layer thickness measured by Martin [5]). Figures 5.8 and 5.9 repeat the data of Figures 5.2 and 5.6 with a constant length scale. A much better collapse of the data occurs.

This indicates that the data measured in the M.I.T. Wind Tunnel does not have a strong dependence on boundary layer thickness.

5.4 A Look at Other Normalization

To get a better collapse of the data, two other normalizations have been tried. The one is normalized on the inner variable V_* , the friction velocity, where the ordinate is $\Phi(\underline{k}, \omega)_L \omega^3 / \rho^2 V_*^6$ and the abscissa is the Strouhal number $S = \frac{\omega V}{V_*^2}$. A plot of the microphone results for the two positions is shown in Figure 5.10. The collapse of the data is still not good.

The other normalization was on flow parameters, where the ordinate is $\Phi(\underline{k}, \omega)_L / \rho^2 v^3$ and the abscissa is $\omega v / U_\infty^2$. A plot of the microphone data is shown in Figure 5.11 and a plot of the Martin plate data is shown in Figure 5.12. This seems to result in a much better collapse of the data.

5.5 Comparison with Other Investigators

5.5.1--Martin Plate. A plot of the Martin plate results measured at position 1 with $\delta^*=0.2$ inches is shown in Figure 5.13. On that figure is a curve representing a least square fit of the data measured by Martin [5] in 1976. Also on the plot is a curve representing a least square fit of the data measured by Jameson [8] in 1975.

The present Martin plate data lies 2-3 dB below what Martin measured in 1976. This is primarily due to Wall Jet Configuration allowing the acoustic cross modes to be absorbed by the anechoic treatment in the chamber. However, the results are still more than 10 dB above Jameson's 1975 data.

5.5.2--Jameson Plate. A plot of the Jameson plate results measured at position 1 with nominal $\delta^*=0.2$ inches is shown on Figure 5.14. The Martin 1976 data and the Jameson 1975 data is also indicated on this figure. In addition, the Jameson 1975 data was also adjusted for a nominal $\delta^*=0.2$ inches instead of actual $\delta^*=0.139$ inches and is indicated on the plot as a dotted line.

As the plot indicates, without compensating for the difference in δ^* , Jameson's 1975 data is typically 12-13 dB below the present data. When the contribution from the

difference in δ^* is removed the present data is still 10dB higher.

In Section 3.4 a comparison was made between the MIT facility and the BBN facility. If it is assumed that the high frequency response of a 1" flush mounted microphone is indicative of the acoustic contamination (argument for this assumption has been given previously and is repeated in the conclusion), then the BBN facility seems to be approximately 3 dB quieter than the M.I.T. facility according to Figures 3.15 and 3.16. With the above compensations, the present data is approximately 7-8 dB higher than Jameson's 1975 data.

Jameson [8] used a 2 gram accelerometer to make his measurement while the present data was measured using a .5 gram accelerometer. Jameson [8] corrected this data for the mass of his accelerometer, but used an infinite plate model which assumes modal overlap conditions. The actual data was measured at modes where modal overlap did not exist. Tests were performed on the Jameson plate comparing response of the 2 gram accelerometer used by Jameson and the 1/2 gram accelerometer presently used. The test indicated that the 2 gram accelerometer would have a 2-4 dB effect on the results while the infinite plate model would only predict errors on the order of 1/2 dB.

Accounting for all the above, the present data at best is still 5-6 dB above Jameson's 1975 data. This would allow the results to be within each other's scatter.

5.5.3--Microphone Array. A plot of the alternating phased microphone array results measured at position 1 with $\delta^*=0.2$ inches is shown on Figure 5.15. The Martin 1976 data and the Jameson 1976 data is also indicated on this figure. In addition, the Farabee and Geib [3] 1976 data is shown on the plot adjusted for a nominal $\delta^*=0.2$ inches instead of the average actual $\delta^*=0.5$ inches measured by Farabee and Geib.

Farabee and Geib also indicated two different slopes in their data as was discussed in Section 5.1.2. The lower speed data had a slope of S^{-4} and the higher speed data, which is thought to be more convectively contaminated had a slope of S^{-5} .

If the present microphone data which is thought to be possibly convectively contaminated is ignored, the remaining data lies in the same vicinity and has close to the same slope as the plate data. The adjusted Farabee and Geib 1976 S^{-4} data also lie in this region, and the Martin 1976 data, which possibly responded to more acoustic contamination by 2-3 dB (see Section 5.5.1), also lie in this region. The Jameson 1975 data is still well below this region as was discussed in Section 5.5.2.

5.6 Low Wavenumber in the Wavenumber-Frequency Plane

The non-dimensional levels of $p(k_1, k_3, \omega)$ have been placed in their respective wavenumber-frequency positions in Figures 5.16, 5.17 and 5.18 for the Martin plate, the Jameson plate, and various microphone arrays, respectively (no variation in k_3 is shown). The wavenumber-frequency location of each piece of

data is marked with a symbol significant of flow speed and an adjacent number that indicates the corresponding value of

$$L_p = 10 \log \left[P(k_1, k_3, \omega) / (q^2 \delta^{*3} / u_\infty) \right] .$$

The data is from position 2 only.

VI. CONCLUSIONS

6.1 Conclusion of Acoustic Contamination

- A. The data from the 1" flushed mounted microphone at frequencies higher than the convective ridge roll-off is almost entirely acoustic contamination because
- i) The phase relation between two microphones (see Figures 3.10 and 3.13) show a linear phase delay at the higher frequencies with a slope of opposite direction than the linear phase delay due to the convective velocities occurring at the lower frequencies. This indicates that the acoustic contamination is coming from downstream. The velocity calculated from the linear phased delay was approximately the speed of sound. When the phase delay was compared to the phase delay of an acoustic source without flow (see Figure 4.5), except for a difference in direction, they were almost exactly the same.
 - ii) The alternating phased array response to flow (see Figure 4.1) at the frequency coincident with the sonic line main lobe response asymptotes to the single microphone response.

- iii) The coherence of the alternating array and single microphone in the array during flow (see Figure 4.3) is nearly zero at the locations of the sonic region nulls in the array.
- iv) When the 6-element array was steered to acoustic waves propagating upstream, above 2.5 kHz the array measurement and the single microphone measurement was very close (see Figure B5).

B. Acoustic contamination during flow is mostly plane wave due to the semianechoic treatment in the wall jet configuration. This is substantiated by the linear phased delay discussed in Item A and acoustic steering results in Table B1.

C. The acoustic contamination during flow is very directive. The arguments discussed in Item A indicate that the high frequency measurements of the flush mounted 1 inch microphone is mostly acoustic. When compared to the blockhouse microphone in Figure 3.14, there are substantial differences. This comparison agrees with the qualitative argument concerning directivity given in Section 4.3.4.

D. If the high frequency response of the flush mounted 1 inch microphone is more indicative of the acoustic contamination during flow than the

blockhouse microphone as argued above, then the BBN wind tunnel is perhaps 3 dB quieter (at least at the higher frequencies) than the M.I.T. wind tunnel (see Figures 3.15 and 3.16).

- E. The plates are responding very strongly to acoustic contamination. The acoustic response test, although not conclusive, indicated the response to acoustic contamination was nearly as great as the measured levels, especially at the lower speeds. When attempts to reduce acoustic contamination were made, such as using the wall jet test configuration, reduction in overall levels were observed. This indicated that acoustic contamination contributed to the results.

6.2 Conclusion on Convective Contamination

- A. The results of the microphone array become convectively contaminated at the higher speeds and lower frequencies. This follows from
 - i) The rejection of the convective contamination is due mostly to the low pass wavenumber filtering effect of the single 1 inch microphone. The phase relation between two microphones (see Figures 3.10 and 3.13) distinctly show the region where the microphones are responding to the convective contamination.

As the free stream velocity increases, this region extends to the frequency where low wavenumber data is measured.

- ii) Figure 5.1 distinctly shows an increasing negative slope for the higher speed, low frequency, low wavenumber data points. This corresponds to the convective ridge shifting to higher frequencies with higher speeds.

- B. Martin [5] and Jameson [8] indicated increasing convective contamination with increasing speed, but this was not significant until 50 m/s.

6.3 Conclusions on Low Wavenumber Data

- A. With the exception of the microphone array where the high speed data is obviously convectively contaminated, the Martin plate, the Jameson plate, and the microphone array all result in the same low wavenumber measurements. They typically lie 2-3 dB below a least "square fit" of Martin's [5] 1976 data with a significant amount of scatter.
- B. The scatter is believed to be due to different amounts of acoustic and convective contamination measured by each filter. Each mode of each plate has a slightly different wavenumber-frequency response characteristic and the various

shadings of the microphone produces different wavenumber-frequency response characteristics. The contamination varies with wavenumber, frequency, and speed. All of this contributes to spreading the data.

- C. Measurements were made at two locations with substantially different boundary layer displacement thickness, $\delta^* = 0.09$ and 0.21 inches. There was little difference between the measured data at the two locations, thus indicating a weak dependence on δ^* .
- D. The Farabee and Geib [3] 1976 microphone data when adjusted to a nominal $\delta^* = 0.2$ inches (Farabee and Geib's actual average $\delta^* = 0.5$ inches), lay in the same region as the current data.
- E. Arguments were made in Section 5.5.2, reducing the difference between Jameson's [8] 1975 data and the current data from 12-13 dB difference to 5-6 dB difference. This would bring the two results to within each other's scatter. The arguments for reducing the scatter were adjustment for difference in δ^* (Jameson's average $\delta^* = 0.139$ inches), differences in acoustic contaminations, and a more accurate adjustment

due to mass of the accelerometer. The remaining 5-6 dB difference could not be explained quantitatively. Possible differences could be differences in wavenumber-frequency response of the current Jameson plate and the one used in 1975, inaccurate estimation of facility acoustic contamination, technical differences between the two experimental programs, or facility dependent low wavenumber excitation.

- F. The 12-element collinear array resulted in slightly higher levels than the 6-element collinear array. This is due to both arrays having the same level of depth in the acoustic nulls limited by trace acoustic waves.
- G. A stagger array can only be used to decrease the streamwise spacing of the microphone and thus use the null of the single microphone wavenumber response to cancel the first aliasing lobe of the array wavenumber response if there is no k_3 dependence in the signal that is to be measured. If there is a k_3 dependence, major lobes would appear for an alternating phased stagger array at not only the expected locations for a collinear alternate phased array but also at the major lobes of a collinear common phased array (see Figure A12).

The same is true for a common phased stagger array.

- H. The cross array used as a lateral array showed there to be k_3 dependence in the frequency range of the spectrum dominated by the convective ridge.
- I. Based on the arguments of Sections 6.1 and 6.2, it cannot be certified that a true measure of the low wavenumber levels has been made. Because of convective contamination, the best data is obtained at the lower speed. However at the lower speeds, the low wavenumber levels are also reduced and acoustic contamination or equipment sensitivity becomes a problem.

APPENDIX A

12-ELEMENT MICROPHONE ARRAY

The 12-element array design consisted of the same components as described in Section 2.2.3 for the 6-element array. Three configurations were tested, a 12-element collinear array, a 12-element staggered array, and a 7X5 element cross array. The geometry of the three configurations are shown in Figures A1, A2 and A3 respectively.

A.1 12-Element Collinear Array

The 12-element collinear array was designed with the same center to center microphone spacing as the 6-element array. The purpose of the 12-element array was to reduce the width of the main lobe, reduce the levels of the side lobes, and increase the number of nulls in the array response that can be used to reject the acoustic contamination.

The acoustic check of the 12-element alternating phased collinear uniformly shaded array is shown on Figure A4. The main lobe again occurs at 6.3 kHz or $k=2.9 \text{ in}^{-1}$. There are now five nulls before the main lobe. They occur at approximately 1.1, 2.2, 3.3, 4.4, and 5.5 kHz. The 6-element uniformly shaded array acoustic check is shown on the same figure. A comparison of the two acoustic checks shows the 12-element array to have a narrower main lobe and the side lobes are slightly lower. The nulls, however, are approximately of the same depth.

Flow tests were performed on the collinear array at 15, 20 and 25 m/s. The array operated in the alternating phased mode for each speed using uniform and Chebyshev shading. The array was located in position 2 as represented in Figures 3.3 and 3.4.

Figure A.5 shows the alternating phased 12-element collinear uniform shaded array measurements at 15 m/s. Similarly as described in Section 4.2 for the 6-element array, the coincidence of the main lobe and first aliasing lobe of the array beam pattern with the convective ridge can be seen in the measurements at the lower frequencies. The coincidence of the lower side nulls with the acoustic region occurs next and then at approximately 6.3 kHz the coincidence of the main lobe with the acoustic region occurs. The regions become more obvious when observing the coherence between the array and a single microphone in the array as shown in Figure A.6.

The low wavenumber measurements were obtained at the frequencies where the array nulls are coincident with the sonic region. The measured data for both the uniform shading and the Chebyshev shading are listed in Table A1. The values are very close (within the scatter) of the 6-element array low wavenumber data listed in Table 5.1.

When the data is reduced by the methods described in Section 5.1.1 and non-dimensionalizing on boundary layer displacement thickness and dynamic head, the 12-element array results in slightly higher low wavenumber values. This is indicated in Figures A.7 and A.8.

The reason the 12-element array resulted in higher levels is that the low wavenumber levels are still upper bounds. The 1 inch microphones respond very strongly to acoustic contamination (see Appendix B) in the frequency range where low wavenumber measurements are made. The rejection of the acoustic contamination depends on having only plane acoustic waves propagating in the tunnel and the depth of the nulls of the array. Both the 6 and 12-element array had similar depth of nulls and the measured data was approximately the same.

The depth of the nulls are very sensitive to the phase and amplitude measured by the microphones. If all microphones had approximately the same phase response in the frequency range of interest and all microphones were calibrated with the same accuracy, the more microphones in the array the deeper the nulls should be.

Assuming that the phase response and calibration of the microphones are approximately the same, another possibility is that the acoustic trace waves may limit the depth of the nulls. An indication of this can be seen in Figure 2.8. This is a plot of the 6-element array response to an acoustic wave propagating down the tunnel. When the array is uniformly shaded, the depth of the first null was approximately down 48 dB. When Chebychev shading or binomial shading was used, which reduces the side lobes, the depth of the first null was slightly more than 60 dB. If most of the energy of the waves were contained in the side lobes, this would cause deeper nulls. The same trend on null depth between

uniform shading and Chebychev shading was found in the 12-element array.

As a side note, when the same electrical signal was fed into the 6-channel summation box alternately summed and analyzed, the largest cancellation that could be obtained was -65 dB. It is assumed that the 12-channel summation box would produce the same result, but no testing was performed to verify this. Both 6 and 12-element arrays had similar depth of nulls and the measured data was approximately the same. However, when the data was reduced as described in Section 5.1.1, it is assumed that the value measured is low wavenumber and is strongly dependent on the width of the main lobe of the array. This is not the case for an upper bound measurement which may be acoustically contaminated.

A.2 12-Element Stagger Array

The purpose of the stagger array was to decrease the spacing between microphones in the direction of flow so as to nullify the effect of the first aliasing lobe with the null of the single microphone (see Sections 2.2.2 and 2.2.3). The spacing chosen was that determined by Farabee and Geib [3] by measuring the acoustic plane wave response of the array and locating the single microphone response null in frequency space. [This was found after the fact to be incorrect because of the reasons discussed in Section 2.2.3. A better spacing might have been the theoretically determined spacing specified in Section 2.2.2.]

The acoustic check of the alternating phased stagger uniformly shaded array is shown on Figure A9. Because of the smaller spacing the main lobe has shifted higher in frequency to 8.8 kHz or $k=4.1 \text{ in}^{-1}$. The five nulls before the main lobe occur at 1.4, 3.0, 4.2, 6.0 and 7.5 kHz.

Flow tests were performed on the array at 15, 20, and 25 m/s. The array operated in the alternating phased uniform shaded mode for each speed. The array was located in position 2 as represented in Figures 3.3 and 3.4.

Figure A10 shows the alternating phased uniform shaded stagger srray measurements at 15 m/s. The coincidence of the array main lobe with the convective ridge occurs at a higher frequency than for the collinear array. However, the coincidence of the first aliasing lobe with the convective ridge which was also expected to move to a higher frequency and be partially cancelled by the null in the single microphone wavenumber response did not. In fact, it actually occurred at a slightly lower frequency. The convective peaks are more vividly shown in Figure A11, the coherence between the array and a single microphone in the array. The coincidence of the main lobe with the acoustic region is not shown on these figures because they occur at a higher frequency.

The reason the first aliasing lobe did not occur where it was expected was due to the k_3 response of the stagger array and the k_3 content of the convective ridge. The array response is given by the equation

$$A(k_1, k_3) = N^{-1} \sum_{n=1}^N S_n \exp [ik \cdot \underline{x}] \quad (A.1)$$

where \underline{x} is the distant vector from the center of the array to the center of the element. For a four element uniform alternating phased stagger array with equal distance between elements, equation A.1 becomes

$$A(k_1, k_3) = N^{-1} \left[e^{i(\frac{1}{2}k_1 d_1 + \frac{1}{2}k_3 d_3)} - e^{i(\frac{3}{2}k_1 d_1 - \frac{1}{2}k_3 d_3)} - e^{i(-\frac{1}{2}k_1 d_1 - \frac{1}{2}k_3 d_3)} + e^{i(-\frac{3}{2}k_1 d_1 + \frac{1}{2}k_3 d_3)} \right] \quad (A.2)$$

where d_1 and d_3 are the x_1, x_3 constant separation distance.

If $k_3=0$ this equation reduces to

$$A(k_1, 0) = N^{-1} \left[e^{i\frac{1}{2}k_1 d_1} - e^{i\frac{3}{2}k_1 d_1} - e^{-i\frac{1}{2}k_1 d_1} + e^{-i\frac{3}{2}k_1 d_1} \right] \quad (A.3)$$

This gives the same results as if the array was collinear.

The response would be the same as shown in Figure 2.5. However, if $k_3=\pi/d_3$ equation A.2 becomes

$$A(k_1, \pi/d_3) = N^{-1} \left[e^{i\frac{1}{2}k_1 d_1} + e^{i\frac{3}{2}k_1 d_1} - e^{-i\frac{1}{2}k_1 d_1} - e^{-i\frac{3}{2}k_1 d_1} \right] \quad (A.4)$$

This gives the same results as if the array was a common phased collinear array instead of an alternate phased array.

A similar result would also occur if you started with a common phased array. If k_3 is not a multiple of π/d_3 , major lobes will

occur at combined locations of major lobes for the common phased and alternate phased arrays. This is shown in Figure A12 for a 12-element array.

The fact that these major lobes occur in Figure A10 in locations other than those determined by $k_3=0$ indicate a k_3 content in the convective ridge. This will be shown in the next section on the cross array.

The low wavenumber results for the alternating phased, uniformly shaded stagger array at 15, 20, and 25 m/s is shown in Figure A13. The measured values can be found in Table A2.

A.3 Cross Array

The cross array was used to determine if there was a lateral (k_3) wavenumber effect. Figure A15 shows the transfer function between a common phased array consisting of 5 lateral microphones with a single microphone. In the frequency range where the convective ridge dominates there is a dip in the transfer function. However in the acoustic region (above 2.5 kHz) there is little difference between the array and the single microphone. This shows that there is a k_3 effect in the convective region but the acoustic is primary a plane propagating in the x_1 direction.

APPENDIX B

ARRAY STEERING

B.1 Beamforming

Array steering or beamforming is the reception of energy propagating in a particular direction while rejecting energy propagating in other directions. Signals in the beam are passed and those out of the beam are attenuated. Beamforming is thus analogous to band pass filtering.

The principles of beamforming will be explained with the aid of Figures B1 and B2. In Figure B1, a plane wave is propagating at some velocity c_0 and is incident on the boundary with some angle θ with the normal to the boundary. The trace wave is the projection of the wave on the boundary. For a given wavelength λ , the trace wavelength is given by

$$\lambda_t = \frac{\lambda}{\sin\theta} \quad \lambda_t \geq \lambda \quad (B.1)$$

The trace wavelength is always larger than the actual wavelength. In contrast, the trace wavenumber, proportional to the inverse of the trace wavelength is always smaller than the propagating wavelength and is given by

$$k_t = k \sin\theta \quad k_t \leq k \quad (B.2)$$

At the location where the arrow is coincident with the boundary, the trace wave and the propagating wave must arrive at the same time. Since the trace wave has to travel a longer

distance, it must travel at a faster speed. The trace velocity is

$$c_t = \frac{c_o}{\sin\theta} \quad c_t \geq c_o \quad (B.3)$$

One type of beamforming is shown in Figure B2. This is a weighted delay-and-sum beamformer. The particular setup shown in Figure B2 consists of a collinear array of receivers equally spaced in the boundary. This type of array is used to detect waves in the plane of the figure. Out-of-plane waves could be detected if the array was two dimensional. Each receiver has individual gain control to adjust the amplitude of the signal and to be used for shading the array. In addition, unlike the array design described in Section 2.2.3, each signal can be delayed in time before it is summed and analyzed.

If there are no time delays between receivers, the most receptive direction would be perpendicular to the plane of the array (see Figure 2.4). The signal coming from this direction would be added together in phase while those approaching from other directions would be added with different phases and would tend to cancel themselves out.

Because we are dealing with plane propagating waves, a wave propagating at some angle θ with the normal to the boundary (see Figure B2) will be seen by the receiver on the leading edge of the array first and then each successive receiver will see the same signal at some later time. Since

the receivers are equally spaced, this time delay between receivers will be a constant. Then by delaying the signal of each previous receiver by the time delay determined from the angle of incidence and the speed of propagation, the signal in this direction can be added together in phase while those in other directions will tend to cancel themselves out. The time delay for a particular direction and propagating speed is

$$\tau_d = \frac{D}{c_t} = \frac{D \sin \theta}{c_o} \quad (\text{B.4})$$

The weighted delay-and-sum beamformer takes the form

$$\text{BF}(t) = \frac{1}{N} \sum_{i=0}^{N-1} W_i R_i(t - i\tau_d) \quad (\text{B.5})$$

where	$\text{BF}(t)$	is the summed signal
	N	is the number of receivers
	W_i	is the weighting factor
	$R_i(t - i\tau_d)$	is the signal from the i th receiver at time $(t - i\tau_d)$.

This signal then can be spectrum analyzed or bandpassed filtered to determine the frequency content.

The schematic of the beamforming process in Figure B2 is done in the time domain. In the actual experiment, the beamforming was performed in the frequency domain. A schematic of this is shown in Figure B3. In this case the necessary

delaying, filtering and summing operations are performed in the frequency domain through the use of Fourier transform. In this case equation B.5 takes the form

$$fd(\omega) = \frac{1}{N} \sum_{i=0}^{N-1} W_i R_i(\omega) \exp^{-j(i\omega\tau_d)} \quad (B.6)$$

where $fd(\omega)$ is the frequency domain beamformer
 $R_i(\omega)$ is the Fourier transform of the receiver signal $R_i(t)$
 $\exp^{-j(i\omega\tau_d)}$ is the phase delay corresponding to a time delay at a particular frequency.

B.2 Array Steering in the Wind Tunnel

Figure B4 shows a schematic of the relationship of the turbulent and acoustic pressure spectra in the wavenumber frequency domain. The schematic allows for positive and negative wavenumbers. A positive wavenumber represents a wave propagating downstream. A negative wavenumber represents a wave propagating upstream. In this schematic, it is assumed that the convective ridge at 15 m/s is primarily composed of waves propagating downstream while the acoustic spectra consist of waves propagating both upstream and downstream. On the wavenumber axis, the main lobe and the aliasing lobe for the common phased 6-element array is indicated by an X.

Initially, the array was used to steer acoustically. Time delays were chosen in accordance with equation B.4 for the upper half plane of the array, where -90° is grazing waves propagating downstream and $+90^\circ$ is grazing waves propagating upstream. The results at different frequencies are tabulated in Table B1 for a flow speed of 15 m/s and are compared to the single 1 inch microphone. The acoustic steering results are only valid well above 1 kHz. Referring to Figure B4 again, it can be seen that the aliasing lobes will be contributing convective contamination below this region. As can be seen from Table B1, most of the acoustic contamination is coming from downstream at the grazing angle. Figure B5 compares the spectrum of the array steered downstream at the grazing angle with the single microphone spectrum. As can be seen, above 2.5 kHz the two are very close.

In Figure 4.1 when the main lobe of the array was coincident with the sonic line, the array result asymptotes with the single microphone at that point. Figure B5 does not indicate that even though it was steered in that direction. The reason for the difference is the array results in Figure 4.1 were summed by analog methods and analyzed with a spectrum analyzer in the same room. The steered array results were performed on a PDP 11/44 computer where the microphone signals were transmitted a longer distance to the computer. The long transmission length caused varying time delays between channels in the order of 0.1 - 1.0 microsec, while the analog method

resulted in varying time delays that were down an order of magnitude. This had a small effect on the main lobes of the array response. (It had a larger effect on the nulls of the array response and as a result the computer was not used to measure low wavenumbers.)

Next the array was steered convectively. At first this was done by the same method as was used acoustically using equation B.6. However, the aliasing lobes on the negative wavenumber side measured the acoustic region. This can be seen by the dotted lines on Figure B4, representing what these aliasing lobes see in the wavenumber frequency domain. The result of convectively steering this way is shown in Figure B6. Notice the picket fence effect.

The next attempt used was to shift the array in wavenumber space with no variation with frequency. This is similar to what was done by analog means with the alternate phased array. In doing this equation B.6 takes the form

$$fd(\omega) = \frac{1}{N} \sum_{i=0}^{N-1} W_i R_i(\omega) \exp^{-j(i\theta_s)} \quad (B.7)$$

$$\text{where } 0 \leq \theta_s \leq 2\pi$$

For the alternating phased array $\theta_s = \pi$ and the main lobe shifts to $k=\pi/d$, where d is the microphone spacing.

The main lobe was shifted from $0 \leq k \leq 2\pi/d$, where $d=1.07$. Data was obtained from the array spectrum at 15 m/s at the coincidence of the peak of the main lobe and the first

aliasing lobe with the convective ridge. This is usually evident on the spectrum, (see Figure 4.1). The result is tabulated in Table A2.

References

- [1] Maidanik, G. and D.W. Jorgenson, "Boundary Wave Vector Filters for the Study of Pressure Fields in a Turbulent Boundary Layer," JASA, 42, pp. 494-501 (1967).
- [2] Blake, W.K. and D.M. Chase, "Wavenumber-Frequency Spectra of Turbulent Boundary Layer Pressure Measured by Microphone Arrays," JASA, 49, pp. 862-867 (1971).
- [3] Farabee, T.M. and F.E. Geib, Jr., "Measurements of Boundary Layer Pressure Fields with an Array of Pressure Transducers in a Subsonic Flow," NSRDC Report 76-0031 (1976).
- [4] Aupperle, F.A. and R.F. Lambert, "On the Utilization of a Flexible Beam as a Spatial Filter," JS&V, 24, pp. 259-267 (1972).
- [5] Martin, N.C., "Wavenumber Filtering by Mechanical Structures," M.I.T. Ph.D. Thesis (January 1976).
- [6] Moeller, M.J., N.C. Martin and P. Leehey, "Low Wavenumber Levels of a Turbulent Boundary Layer Wall Pressure Fluctuations in Zero and Adverse Gradients," M.I.T. Acoustics & Vibration Lab. Report 82464-2 (1978).
- [7] Jameson, P.W., "Measurements of the Low Wavenumber Component of Turbulent Boundary Layer Wall Pressure Spectrum," Bolt, Beranek & Newman Report #1937 (1970).
- [8] Jameson, P.W., "Measurement of Low Wavenumber Component of Turbulent Boundary Layer Pressure Spectral Density," 4th Symposium on Turbulence in Liquids, University of Missouri-Rolla, September 1975.
- [9] Bruel, P.V. and G. Rasmussen, "Bruel & Kjaer Technical Review," No. 2 (1959).
- [10] Chase, D.M., "Turbulent Boundary Layer Pressure Fluctuations and Wavenumber Filtering by Non-uniform Spatial Averaging," JASA, 46, pp. 1350-1356 (1969).

References (cont'd)

- [11] Dolph, C.L., "A Current Distribution for Broadside Arrays which Optimize the Relationship between Beam Width and Side-Lobe Level," Proceedings of the Institute of Radio Engineers, 34, pp. 335-348 (1948).
- [12] Martin, N.C. and P. Leehey, "Low Wavenumber Wall Pressure Measurements Using a Rectangular Membrane as a Spatial Filter," JASA, 52, pp. 95-120 (1977).
- [13] Hanson, C.E., "The Design and Construction of a Low-Noise, Low-Turbulence Wind Tunnel," M.I.T. Acoustics & Vibration Lab. Report 79611-1 (1967).
- [14] White, R.M., Viscous Fluid Flow, McGraw-Hill, 1974, 480p.
- [15] Burton, T.E., "Wall Pressure Fluctuation at Smooth and Rough Surfaces under Turbulent Boundary Layers with Favorable and Adverse Pressure Gradients," M.I.T. Acoustics & Vibration Lab. Report 70208-9 (1973).
- [16] Blake, W.K., "Turbulent Boundary Layer Wall Pressure Fluctuations on Smooth and Rough Walls," M.I.T. Acoustics & Vibration Lab. Report 70208-1 (1969).
- [17] Blake, W.K., "Turbulent Boundary Layer Wall Pressure Fluctuation on Smooth and Rough Walls," JFM, 44, pp. 637-660 (1970).
- [18] Kinsler, L.E. and A.R. Frey, Fundamentals of Acoustics, John Wiley & Sons, Inc., 1962.
- [19] Smith, P.W. and R.H. Lyon, "Sound and Structural Vibration," NASA publication CR-160.

MODE (m,n)	1976 DATA		1983 DATA	
	<u>Frequency</u>	<u>Loss Factor</u>	<u>Frequency</u>	<u>Loss Factor</u>
3,1	805	.023	792	.026
5,1	910	.0082	914	.0073
7,1	1070	.0089	1078	.0051
9,1	1290	.0031	1304	.0029
11,1	1585	.0049	1606	.0038
13,1	1960	.0019	1979	.0017
15,1	2405	.0017	2425	.0018
17,1	2920	.0018	2938	.0017
19,1	3500	.0019	3519	.0016
21,1	4150	.0014	4166	.0014

TABLE 2.1 Comparison of Experimentally Determined Characteristics
of Martin's CCCC Plate

<u>MODE</u> <u>(m,n)</u>	<u>1975 DATA</u> <u>Frequency</u>	<u>1983 DATA</u>	
		<u>Frequency</u>	<u>Loss Factor</u>
3,2	487	376	.0030
5,2	830	695	.0023
5,3	---	918	.0010
3,4	---	948	.0017
7,1	1205	1017	.0021
7,2	1336	1167	.0012
1,5	---	1204	.0035
3,5	---	1358	.0019
7,3	1612	1403	.0016

TABLE 2.2 Comparison of Experimentally Determined Characteristic
of Jameson Plate

Flow Velocity	Position #1				Position #2			
	δ^*	θ	H	V_*	δ^*	θ	H	V_*
	(In.)	(In.)	(M/S)	(M/S)	(In.)	(In.)	(M/S)	(M/S)
15 M/S	0.079	0.058	1.36	0.67	0.215	0.161	1.33	0.55
20 M/S	0.082	0.060	1.37	0.83	0.205	0.153	1.34	0.70
25 M/S	0.087	0.064	1.36	1.04	0.213	0.154	1.33	0.90
30 M/S	0.090	0.067	1.34	1.22	0.213	0.160	1.33	1.09
35 M/S	0.094	0.070	1.34	1.35	0.216	0.164	1.31	1.28
40 M/S	0.096	0.072	1.33	1.54	0.211	0.160	1.32	1.47

TABLE 3.1 Boundary Layer Flow Properties

<u>MODE</u>	<u>Sensitivities for Speaker @ Inlet to Diffuse/(dB)</u>	<u>Sensitivities for Speaker @ Inlet to Tunnel (dB)</u>
3,1	31.4	24.7
5,1	33.2	20.6
7,1	22.5	16.6
9,1	25.5	24.5
11,1	36.2	27.8
13,1	25.8	25.3
15,1	29.3	21.0
17,1	34.8	34.2
19,1	32.2	32.5
21,1	36.5	34.7

$$\text{Sensitivity} = 20 \text{ Log } \left(\frac{\text{Accelerometer Value}}{\text{Microphone Value}} \right)$$

TABLE 4.1 Comparison of Acoustic Sensitivity Test on
Martin Plate with Speakers at Two Different
Locations

Alternating Array Measurements @ Position 1

<u>Speed (M/S)</u>	<u>Shading</u>	<u>Frequency (Hz)</u>	<u>Measured Level (dB)</u>
15	Uniform	2150	- 95.9
15	Uniform	4200	-103.7
20	Uniform	2150	- 84.1
20	Uniform	4200	- 95.0
25	Uniform	2150	- 72.8
25	Uniform	4200	- 88.7
30	Uniform	2150	- 68.2
30	Uniform	4200	- 83.4
35	Uniform	2150	- 62.7
35	Uniform	4200	- 78.9
40	Uniform	2150	- 53.9
40	Uniform	4200	- 72.2
15	Chebyshev	1950	- 93.7
15	Chebyshev	3550	-106.0
20	Chebyshev	1950	- 80.1
20	Chebyshev	3550	- 96.2
25	Chebyshev	1950	- 70.9
25	Chebyshev	3550	- 87.8
15	Binomial	2000	- 93.6
15	Binomial	2400	- 98.8
20	Binomial	2000	- 79.0
20	Binomial	2400	- 86.4

TABLE 5.1 Measured Alternating Array Spectral Levels
All Levels Are dB re 1 Pa and Hz

Alternating Array Measurements @ Position 2

<u>Speed</u>	<u>Shading</u>	<u>Frequency (Hz)</u>	<u>Measured Level (dB)</u>
15	Uniform	2350	- 96.0
15	Uniform	4200	-103.0
20	Uniform	2400	- 82.9
20	Uniform	4100	- 92.1
25	Uniform	2100	- 70.5
25	Uniform	4100	- 86.1
30	Uniform	2350	- 67.7
30	Uniform	4100	- 81.4
35	Uniform	2350	- 62.2
35	Uniform	4100	- 75.1
40	Uniform	2350	- 58.9
40	Uniform	4100	- 69.3
15	Chebyshev	1950	- 88.3
15	Chebyshev	3550	-102.9
20	Chebyshev	1675	- 72.0
20	Chebyshev	3100	- 89.2
25	Chebyshev	2000	- 69.1
25	Chebyshev	3450	- 84.7
15	Binomial	2300	- 93.2

TABLE 5.1 (cont.) Measured Alternating Array Spectral Levels
All Levels Are dB re 1 Pa and Hz

Common Array Measurements @ Position 1

<u>Speed</u>	<u>Shading</u>	<u>Frequency (Hz)</u>	<u>Measured Levels (dB)</u>
15	Uniform	2400	- 97.6
15	Uniform	4200	-103.3
20	Uniform	2400	- 86.3
20	Uniform	4200	- 94.2
25	Uniform	2400	- 77.0
25	Uniform	4200	- 86.8
30	Uniform	2400	- 68.1
30	Uniform	4200	- 81.7
35	Uniform	2400	- 62.6
35	Uniform	4200	- 77.0
40	Uniform	2400	- 57.2
40	Uniform	4200	- 72.8
15	Chebyshev	2400	- 99.3
15	Chebyshev	4200	-107.4
20	Chebyshev	2400	- 86.4
20	Chebyshev	4200	- 93.4
25	Chebyshev	2400	- 76.8
25	Chebyshev	4200	- 88.0
15	Binomial	2400	- 94.7
15	Binomial	4200	-106.3
20	Binomial	2400	- 83.8
20	Binomial	4200	- 95.5
25	Binomial	2400	- 74.2
25	Binomial	4200	- 86.4

TABLE 5.2 Measured Common Array Spectral Levels
All Levels Are dB re 1 Pa and Hz

Martin Plate Acceleration Response @ Position 1

<u>MODE</u>	<u>15 M/S</u>	<u>20 M/S</u>	<u>25 M/S</u>	<u>30 M/S</u>	<u>35 M/S</u>	<u>40 M/S</u>
7,1	-58.2	-49.2	-41.6	-36.2	-31.5	-26.8
9,1	-61.4	-52.7	-43.4	-35.8	-30.4	-21.9
11,1	-63.4	-55.7	-48.4	-42.3	-37.2	-29.7
13,1	-59.4	-49.1	-40.1	-34.7	-29.4	-25.2
15,1	-63.9	-60.1	-51.3	-43.8	-37.3	-32.5
17,1	-60.0	-54.3	-49.8	-45.7	-41.3	-37.3

Martin Plate Acceleration Response @ Position 2

<u>MODE</u>	<u>15 M/S</u>	<u>20 M/S</u>	<u>25 M/S</u>	<u>30 M/S</u>	<u>35 M/S</u>	<u>40 M/S</u>
7,1	-57.5	-50.8	-43.7	-38.7	-32.6	-26.9
9,1	-58.2	-50.2	-41.6	-34.7	-27.5	-21.9
11,1	-58.5	-48.1	-41.7	-37.5	-33.1	-29.1
13,1	-56.4	-45.2	-39.2	-32.8	-28.1	-21.6
15,1	-62.1	-55.8	-50.0	-44.3	-37.0	-32.2
17,1	-62.4	-54.4	-48.0	-42.5	-37.9	-33.5

TABLE 5.3 Measured Martin Plate Spectral Levels
All Levels Are dB re 1 M/S² and Hz

Jameson Plate Acceleration Response @ Position 1

<u>MODE</u>	<u>20 M/S</u>	<u>25 M/S</u>	<u>30 M/S</u>	<u>35 M/S</u>	<u>40 M/S</u>
5,2	-46.0	-39.0	-31.4	-25.0	-18.4
5,3	-45.1	-40.7	-33.9	-27.5	-21.8
3,4	-48.5	-44.9	-38.8	-33.0	-28.2
7,1	-49.8	-45.5	-39.0	-32.2	-24.9
7,2	-49.5	-43.4	-38.4	-30.5	-25.4
1,5	-54.5	-48.4	-44.8	-40.6	-35.6
3,5	-52.2	-46.8	-40.9	-34.1	-29.8
7,3	-52.3	-47.5	-42.0	-35.9	-29.1

TABLE 5.4 Measured Jameson Plate Spectral Levels
All Levels Are dB re 1 M/S² and Hz

TABLE A1

MEASURED 12-ELEMENT ALTERNATING ARRAY SPECTRAL
LEVELS--ALL LEVELS ARE DB RE 1 PA AND HZ

12-Element Alternating Array Measurements Pos 2

Speed (m/s)	Shading	Frequency (Hz)	Measured Level (dB)
15	uniform	2325	- 95.8
15	uniform	4200	-105.0
15	uniform	5275	-105.7
20	uniform	1700	- 77.6
20	uniform	3175	- 92.1
20	uniform	4200	- 95.2
20	uniform	5175	- 94.4
25	uniform	2500	- 79.2
25	uniform	3050	- 84.1
25	uniform	4175	- 88.1
25	uniform	5175	- 87.1
15	Chebyshev	2325	- 96.8
15	Chebyshev	2900	- 98.7
15	Chebyshev	4200	-105.4
15	Chebyshev	4750	-106.7
20	Chebyshev	1700	- 76.6
20	Chebyshev	3150	- 90.5
20	Chebyshev	4275	- 95.2
20	Chebyshev	2275	- 84.5
25	Chebyshev	1875	- 72.9
25	Chebyshev	3025	- 83.3
25	Chebyshev	4250	- 88.6
25	Chebyshev	4675	- 89.4

TABLE A2

MEASURED 12-ELEMENT STAGGER ALTERNATING ARRAY SPECTRAL
LEVELS--ALL LEVELS ARE DB RE 1 PA AND HZ

12-Element Stagger Alternating Array Measurements Pos 2

Speed(m/s)	Shading	Frequency(Hz)	Measured Level(dB)
15	uniform	3075	-101.2
15	uniform	4250	-105.3
15	uniform	5775	-109.5
20	uniform	3250	- 90.5
20	uniform	4200	- 94.4
20	uniform	5750	- 96.6
25	uniform	2750	- 80.9
25	uniform	3125	- 82.4
25	uniform	4100	- 87.0
25	uniform	5650	- 88.7

TABLE B1

ACOUSTICALLY STEERED SPECTRAL LEVELS @ 15 M/S

--ALL LEVELS ARE DB RE 1 PA AND HZ

Angle of Incidence	S P E C T R A L L E V E L S A T		
	2500 Hz	3750 Hz	5000 Hz
-90°	-91.5	-93.9	-96.0
-62°	-92.0	-93.8	-96.0
-49°	-92.7	-94.7	-97.1
-30°	-92.8	-96.0	-96.4
-15°	-92.2	-95.5	-97.7
0°	-93.5	-95.7	-97.3
15°	-93.8	-95.5	-97.3
30°	-88.9	-97.2	-97.1
49°	-85.6	-90.2	-92.6
62°	-84.9	-88.2	-89.3
90°	-84.8	-87.6	-88.5
Flush mounted single microphone	-84.0	-86.0	-97.5

TABLE B2

CONVECTIVELY STEERED SPECTRAL LEVELS @ 15 M/S

--ALL LEVELS ARE DB RE 1 PA AND HZ

Wavenumber (in^{-1})	Spectral Level (dB)	
1.76	-26.3	
2.35	-27.8	
2.93	-31.1	Response at main lobe
3.52	-34.6	
4.11	-35.5	
4.70	-36.2	
5.28	-39.7	
5.87	-40.8	
6.46	-41.9	
7.04	-42.8	
7.63	-45.4	Response at first aliasing lobe
8.22	-48.6	
8.81	-48.9	
9.40	-52.2	
9.98	-52.4	
10.57	-53.9	

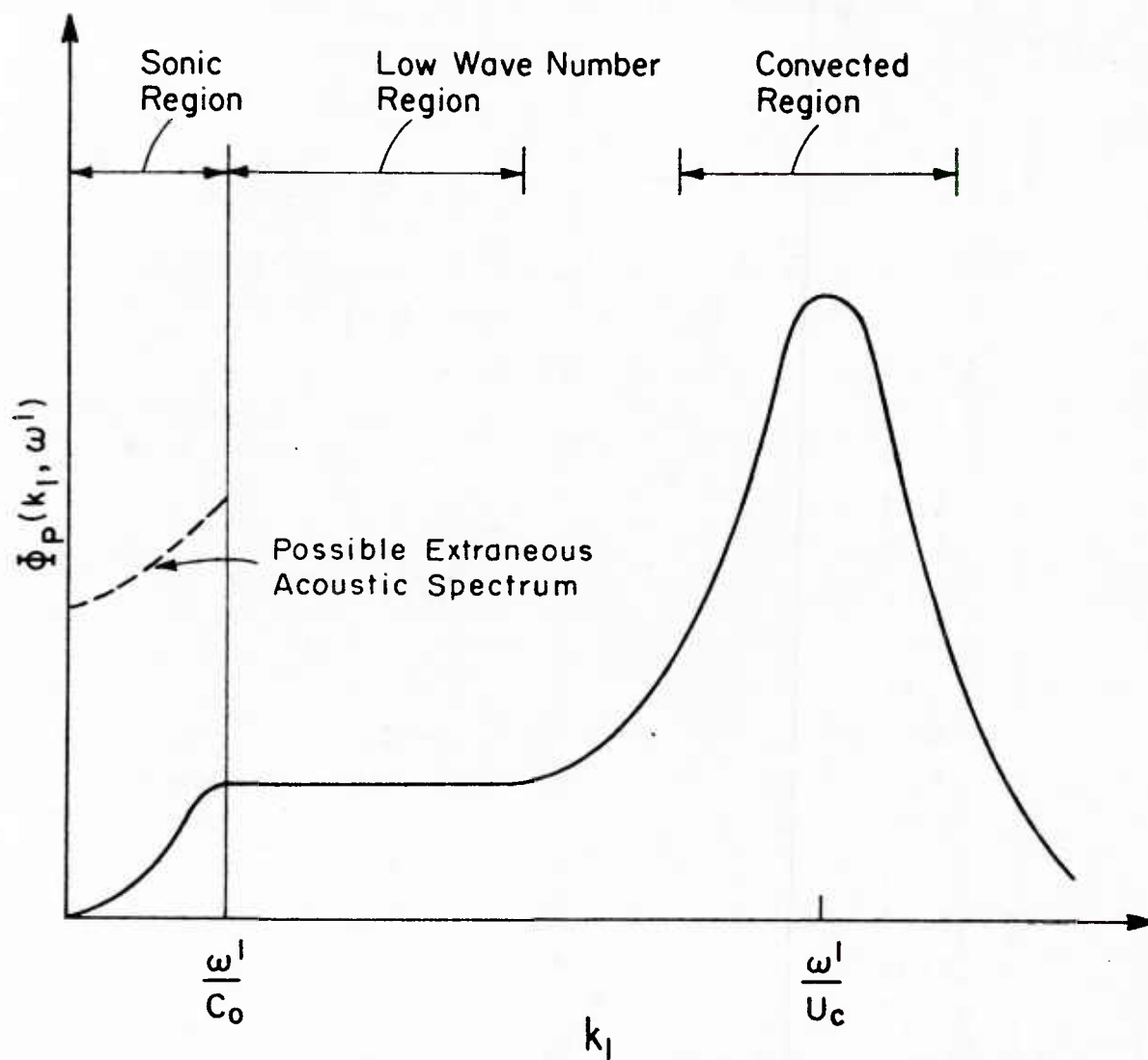


FIGURE 2.1 Schematic of the Variation of Magnitude of the Wavenumber Frequency Spectrum at a Particular Frequency, ω^1 .

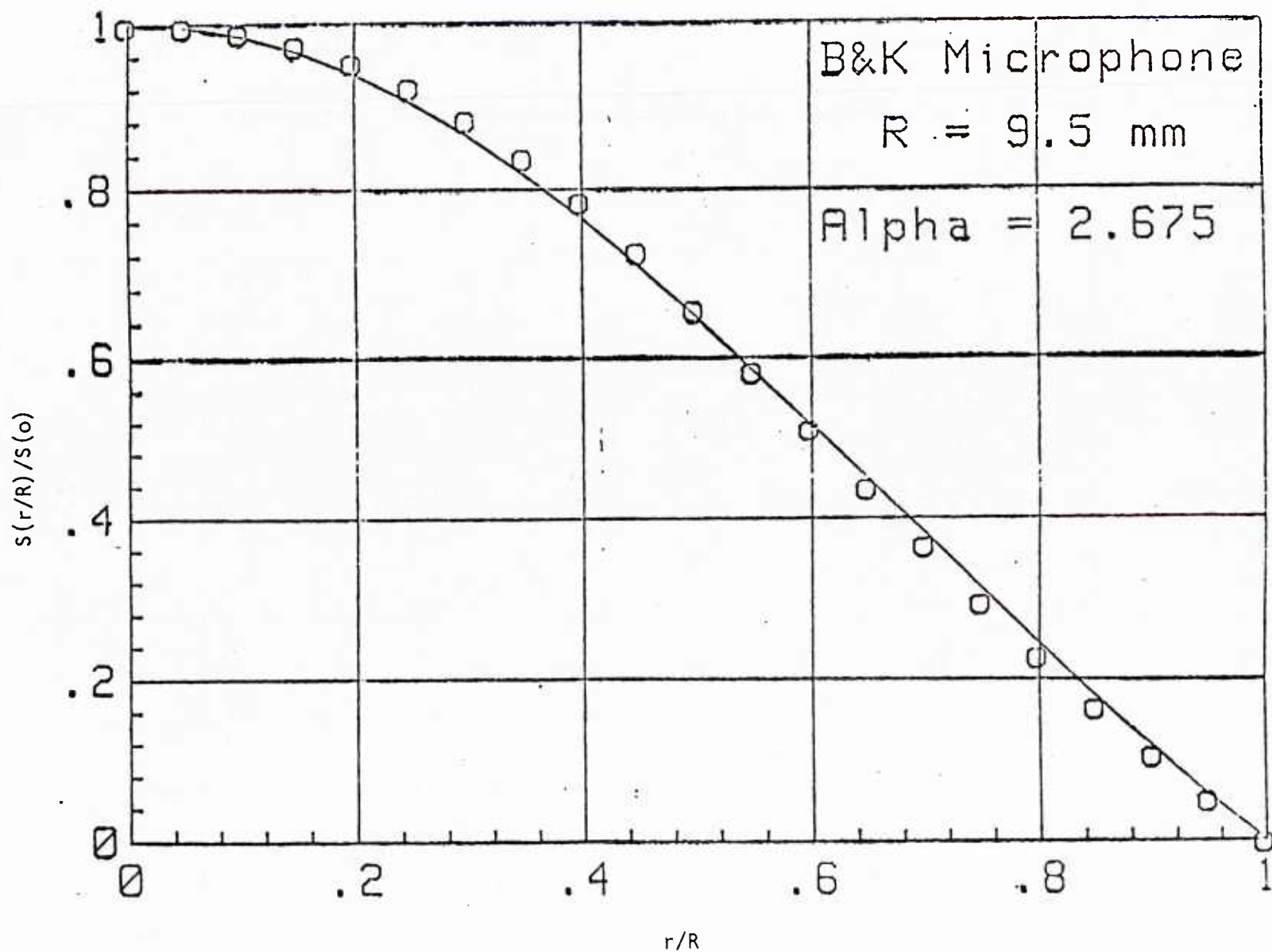


Figure 2.2. Microphone Spatial Sensitivity.

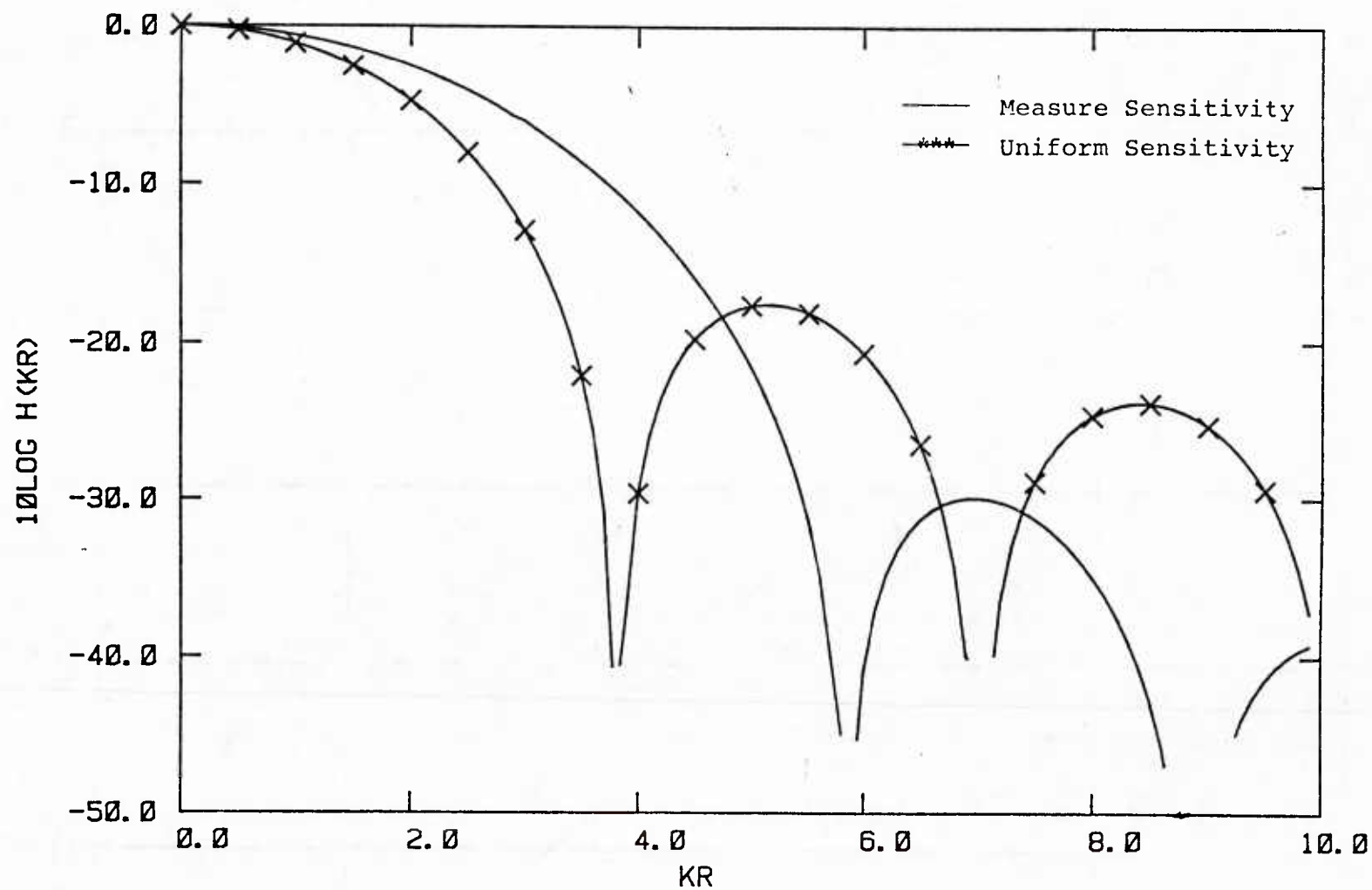


FIGURE 2.3 Single Microphone Wavenumber Response.

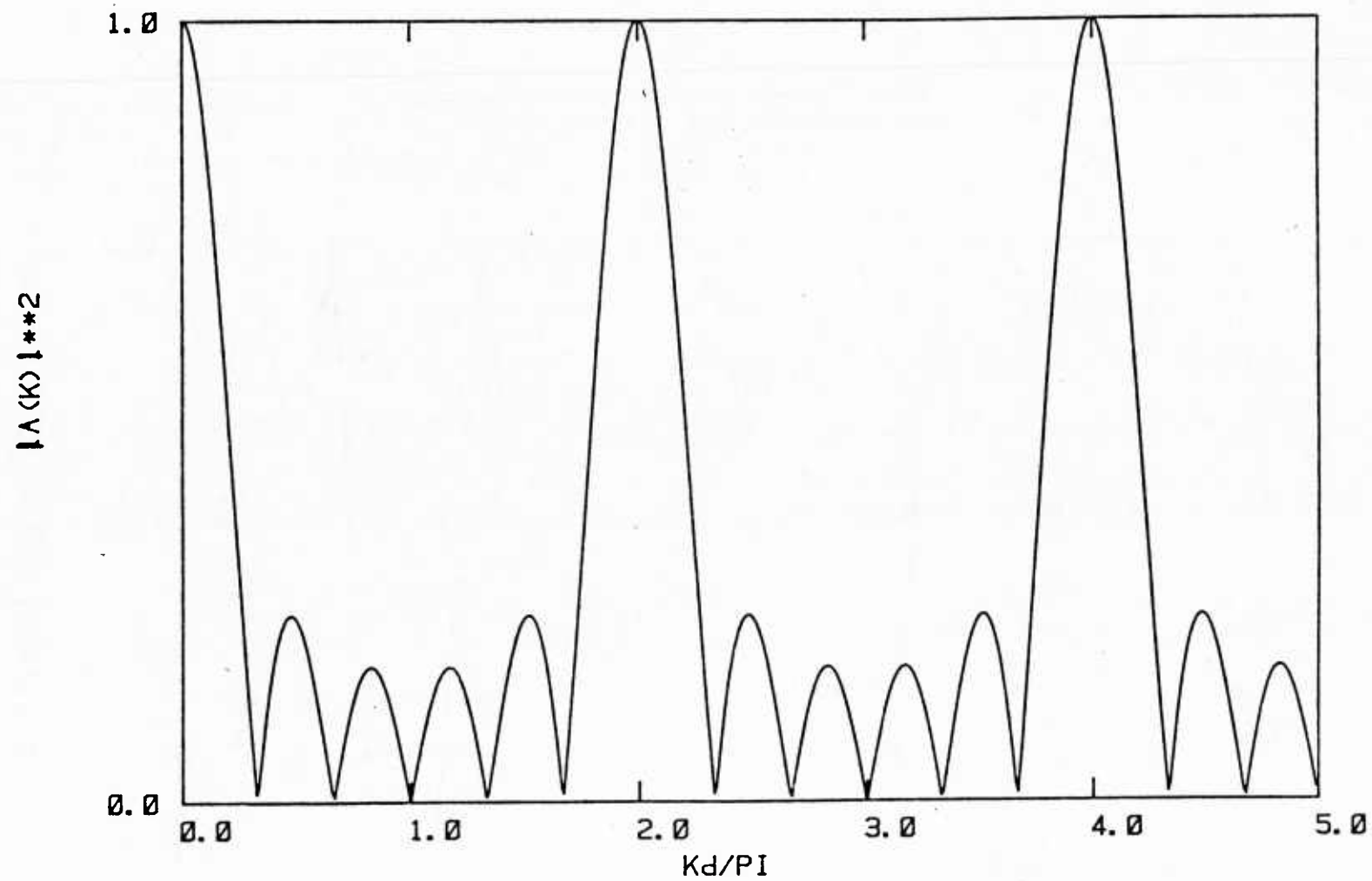


FIGURE 2.4 Common Phase Array Wavenumber Response.

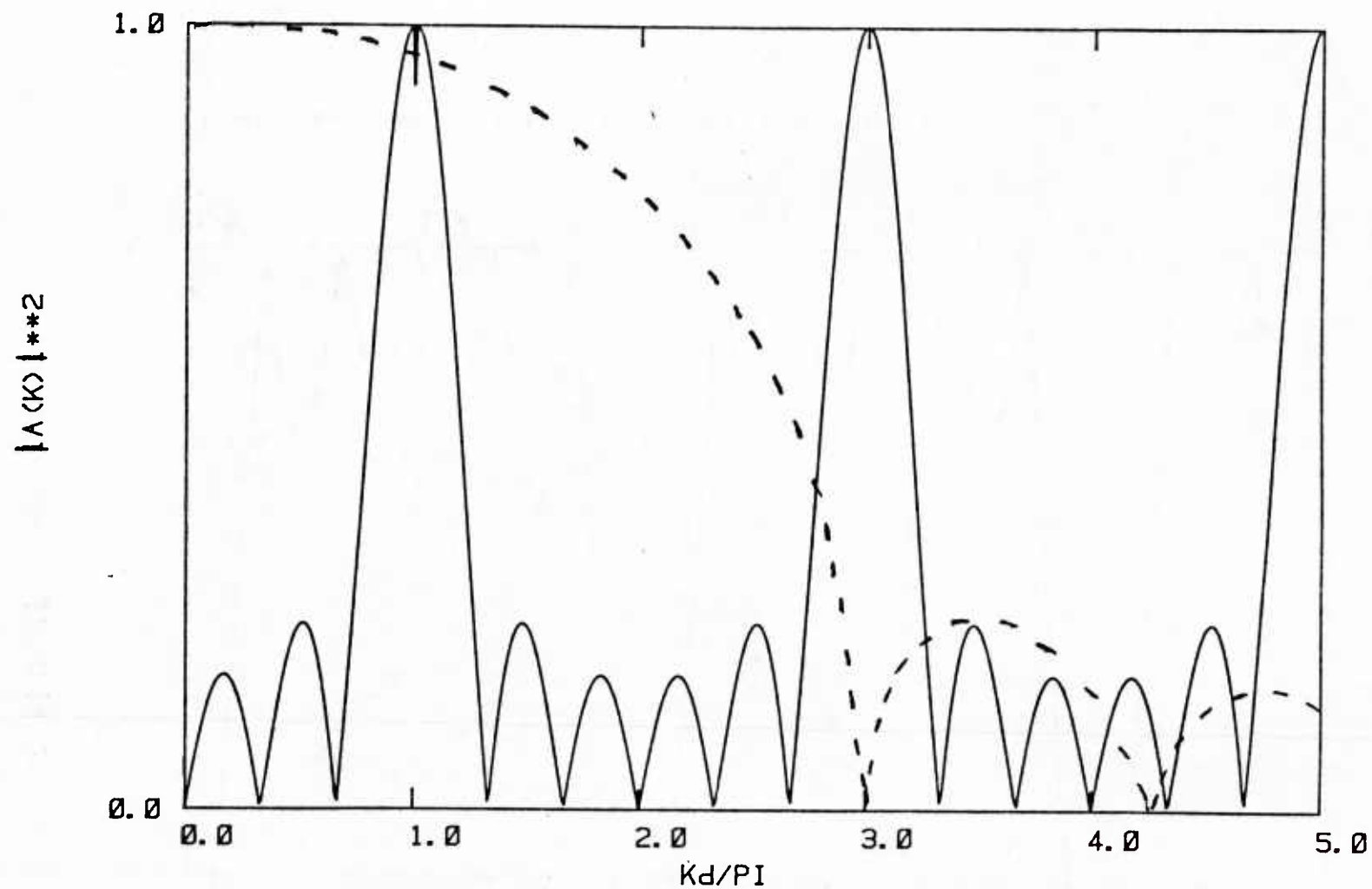


FIGURE 2.5 Alternating Phase Array Response With Single Microphone Response for $d/R = 2.19$.

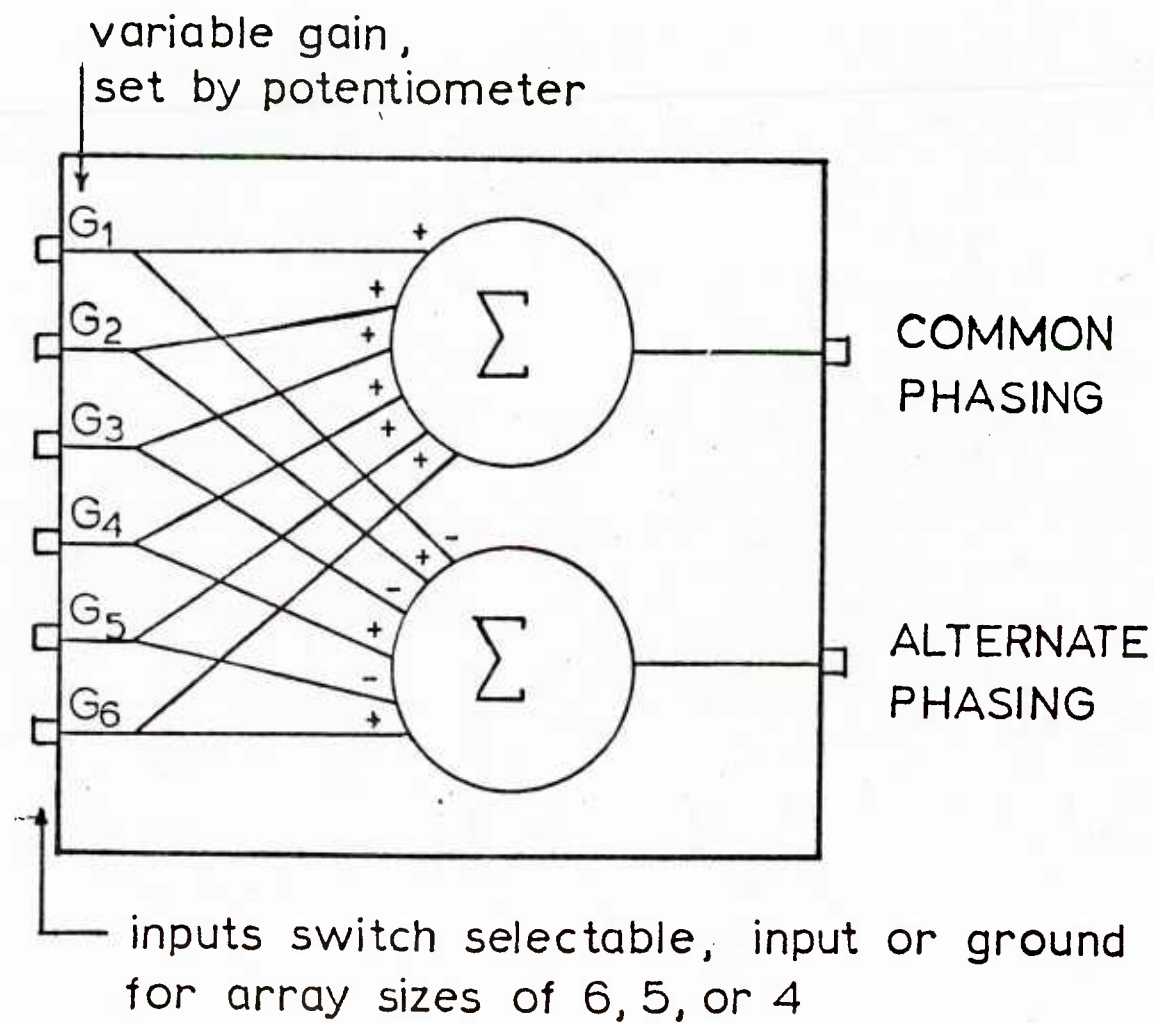


FIGURE 2.6 Schematic of Summation Box

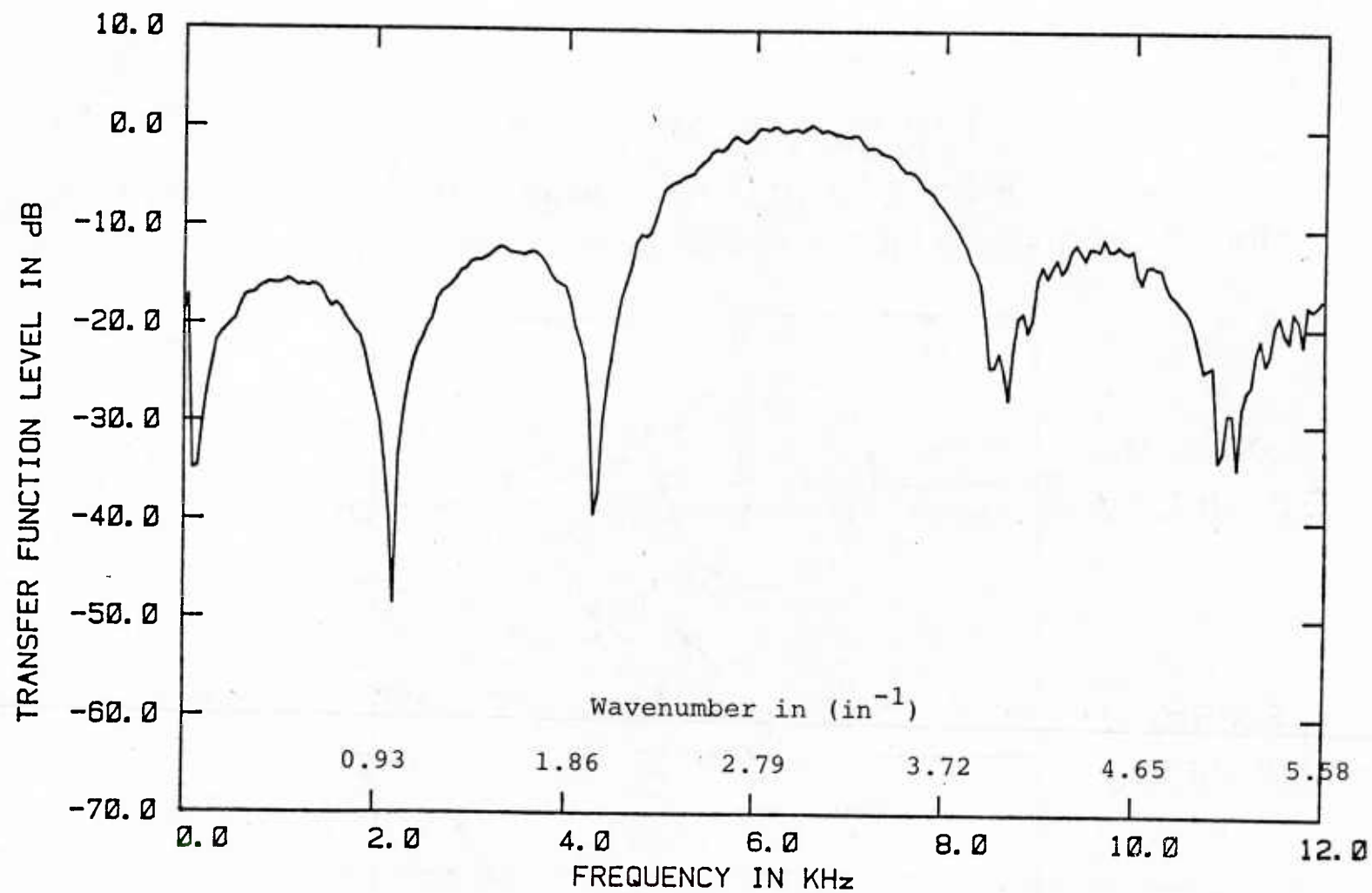


FIGURE 2.7 Measured Alternating Phased Wavenumber Response.

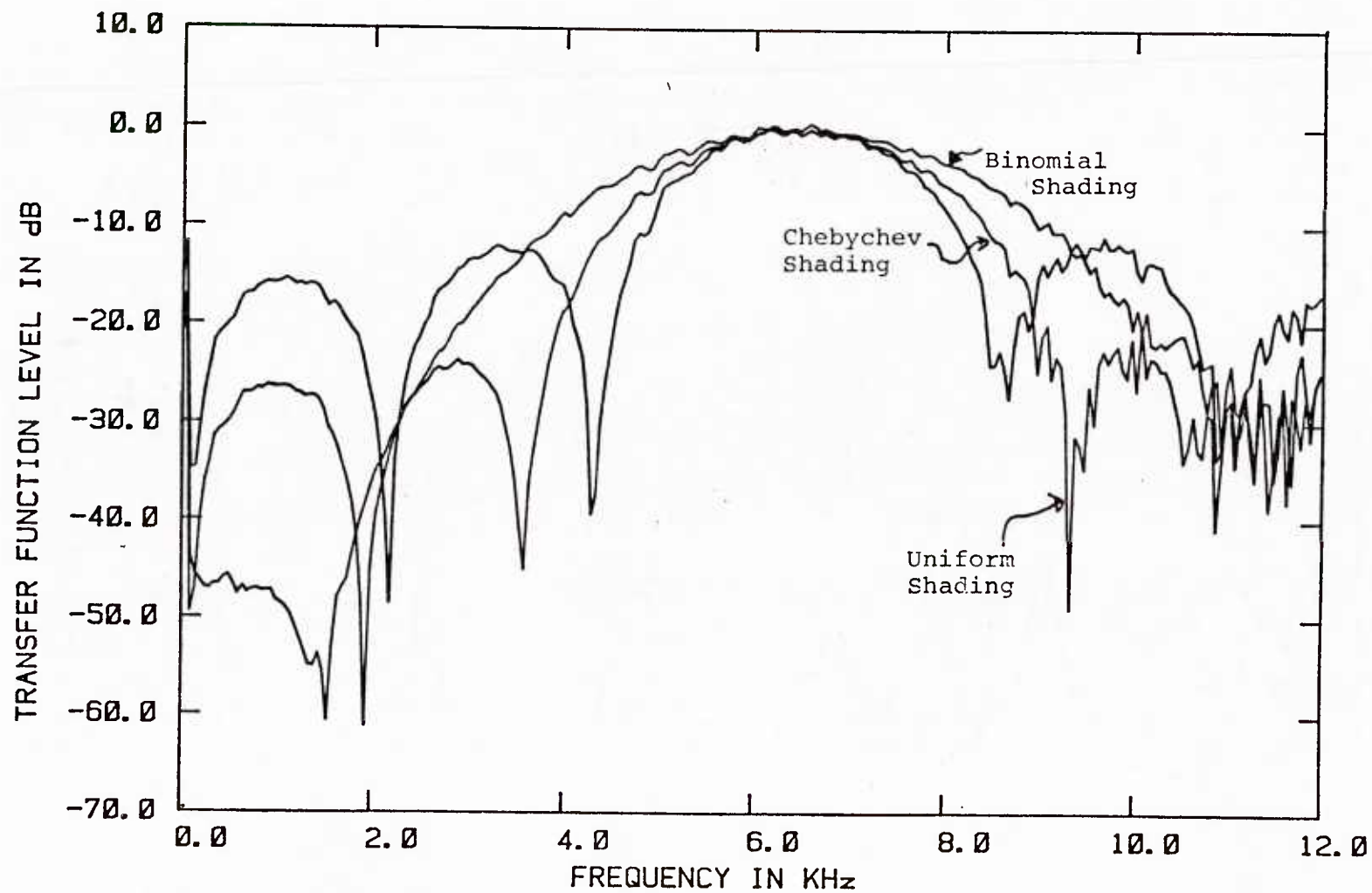


FIGURE 2.8 Effect of Shading on Wavenumber Response.

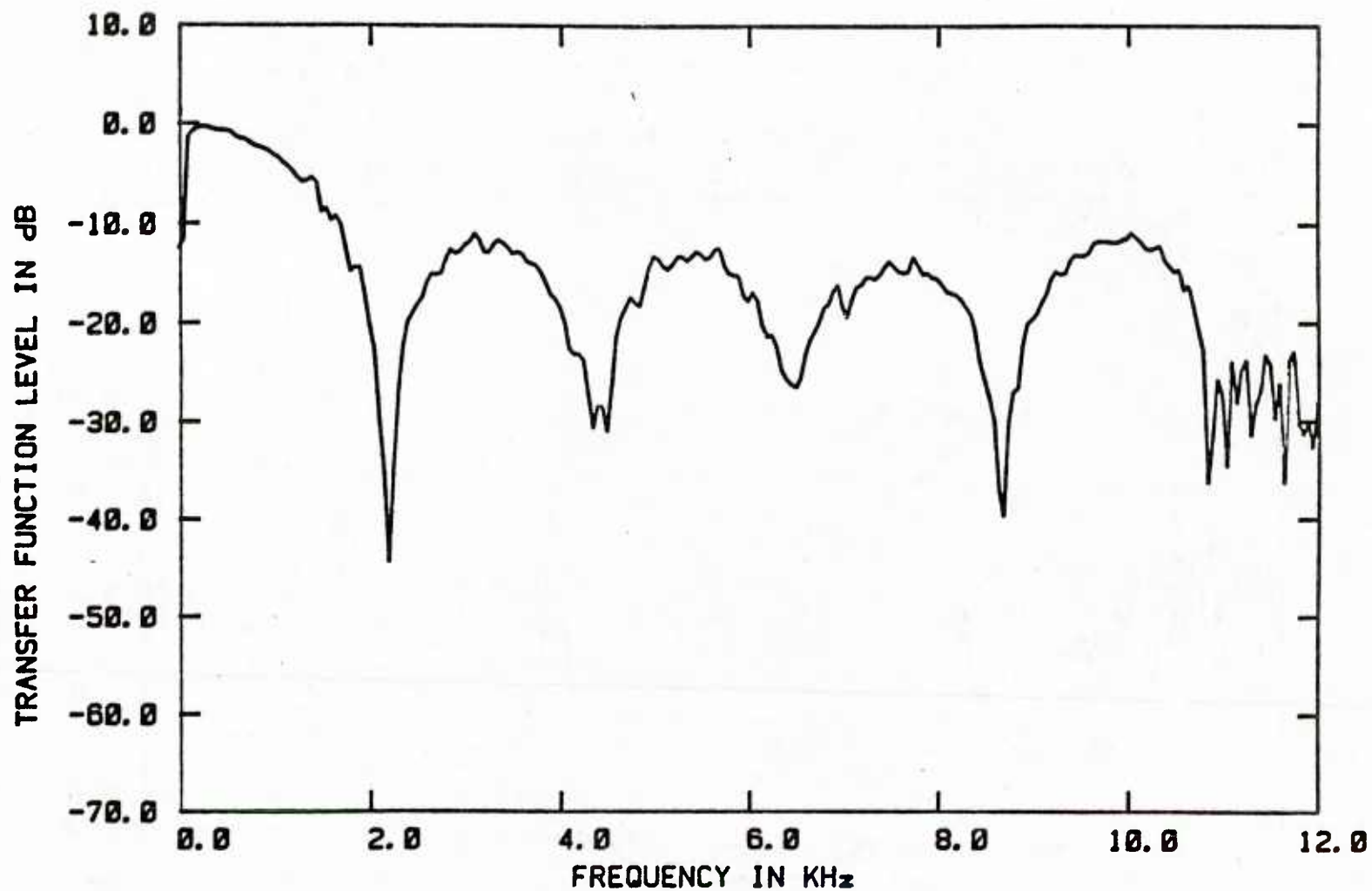


FIGURE 2.9 Measured Common Phase Array Wavenumber Response.

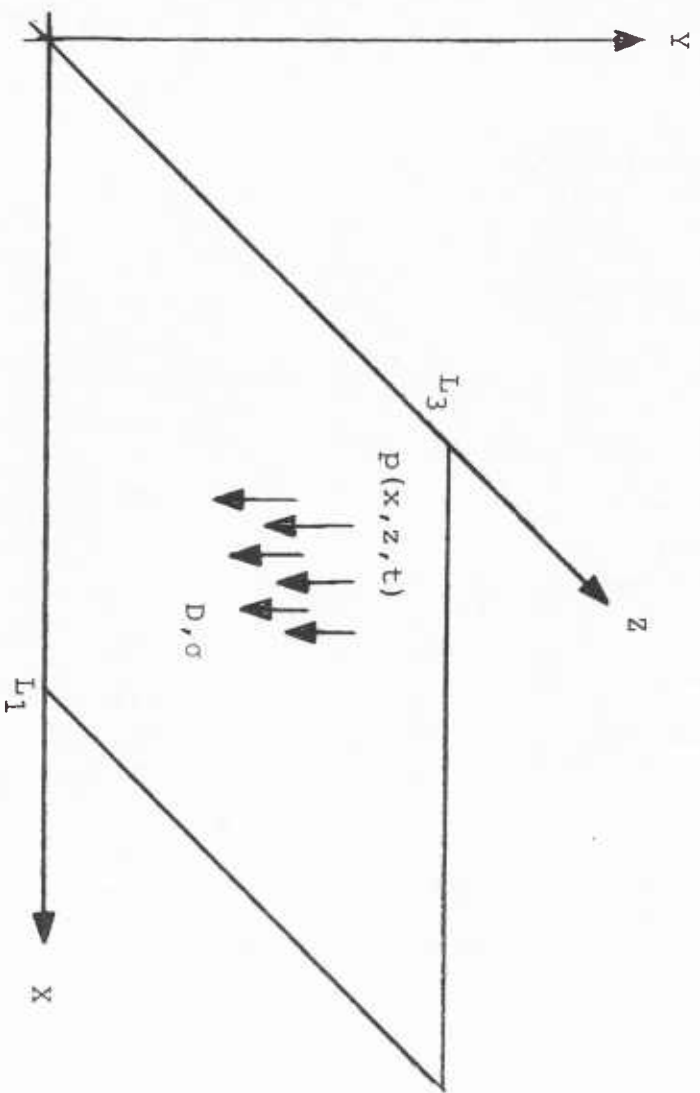
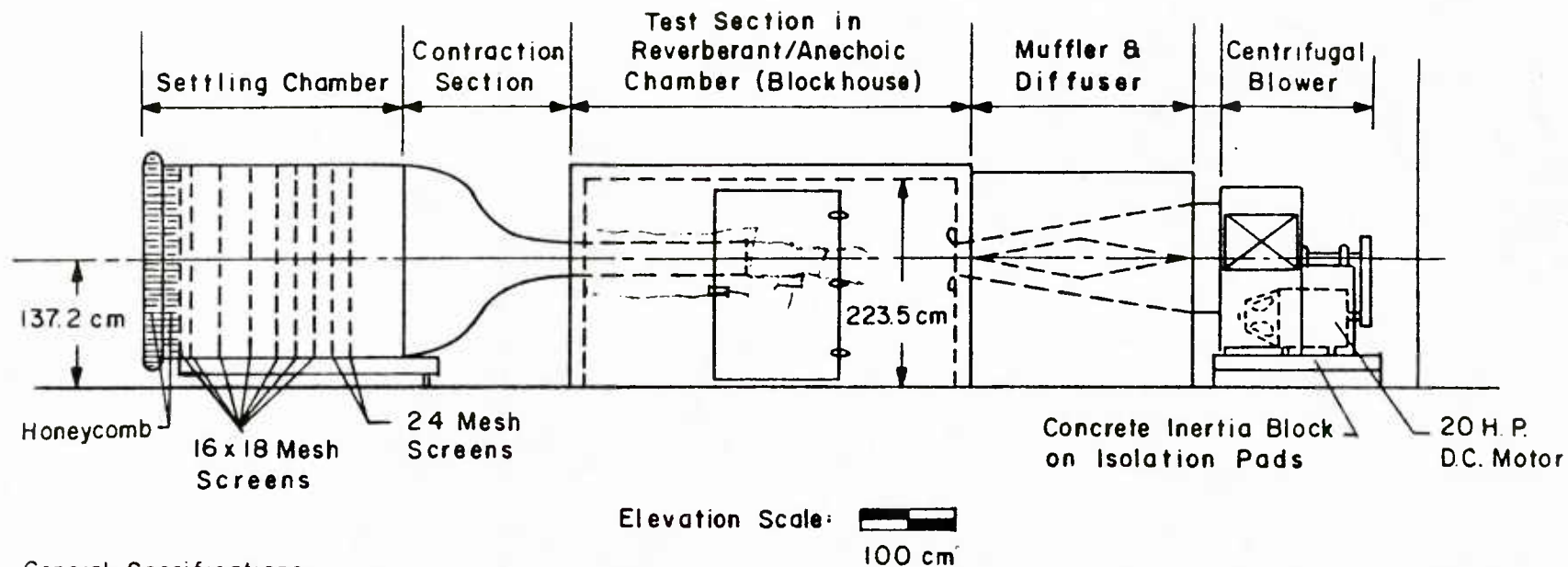


Figure 2.10. Geometric Consideration for plates.



General Specifications:
 Contraction Ratio: 20:1
 Test Section: 38cm x 38cm, shown in
 open duct configuration

WIND TUNNEL FACILITY — ROOM 5-024
 ACOUSTICS & VIBRATIONS LABORATORY
 MASSACHUSETTS INSTITUTE OF TECHNOLOGY

FIGURE 3.1

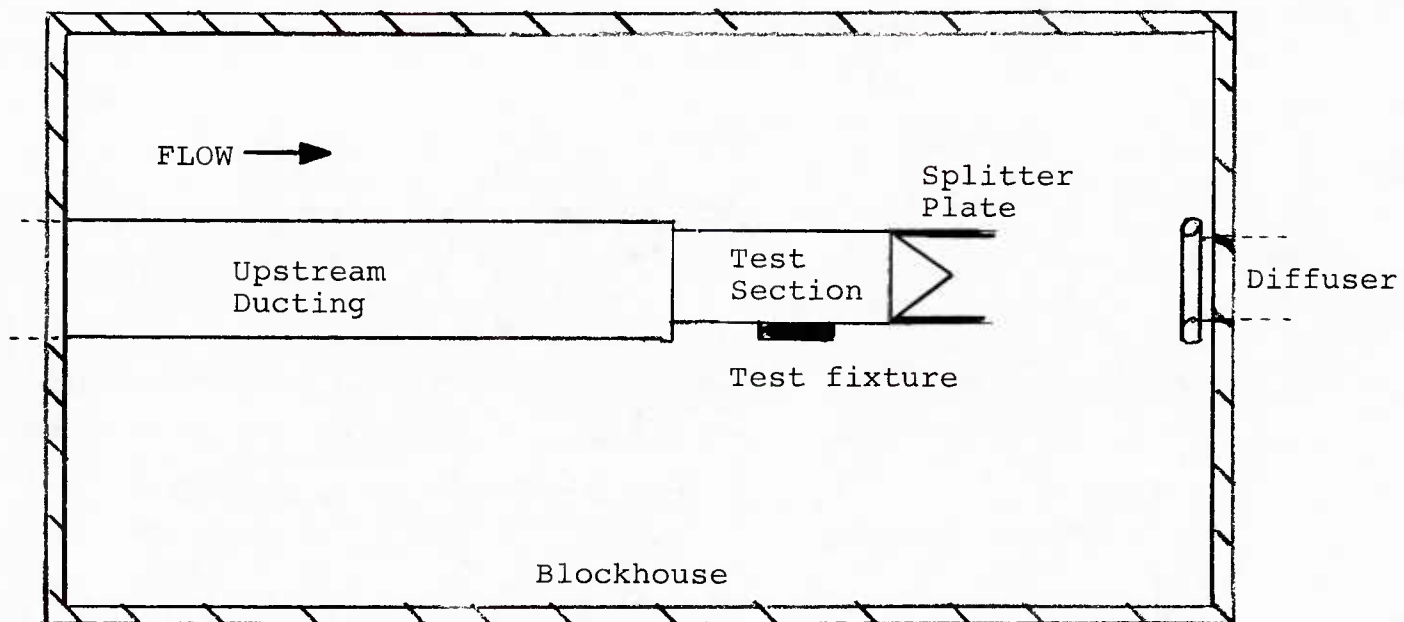


Figure 3.2. Hardwalled Duct Configuration.

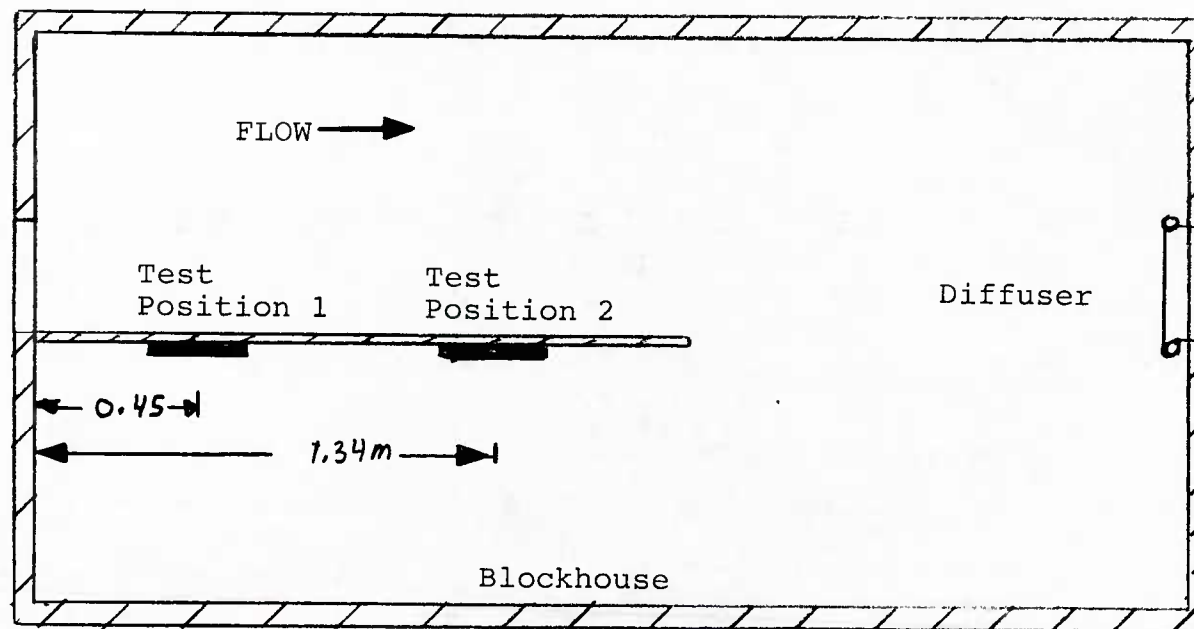


Figure 3.3. Wall Jet Configuration (side view).

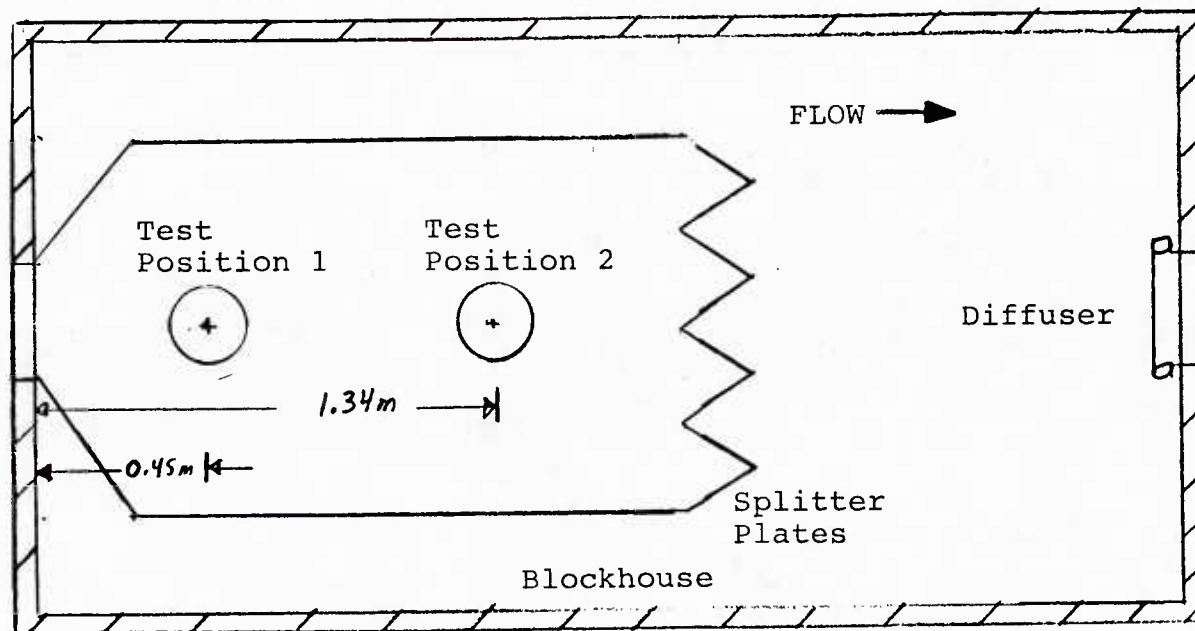


Figure 3.4. Wall Jet Configuration (top view).

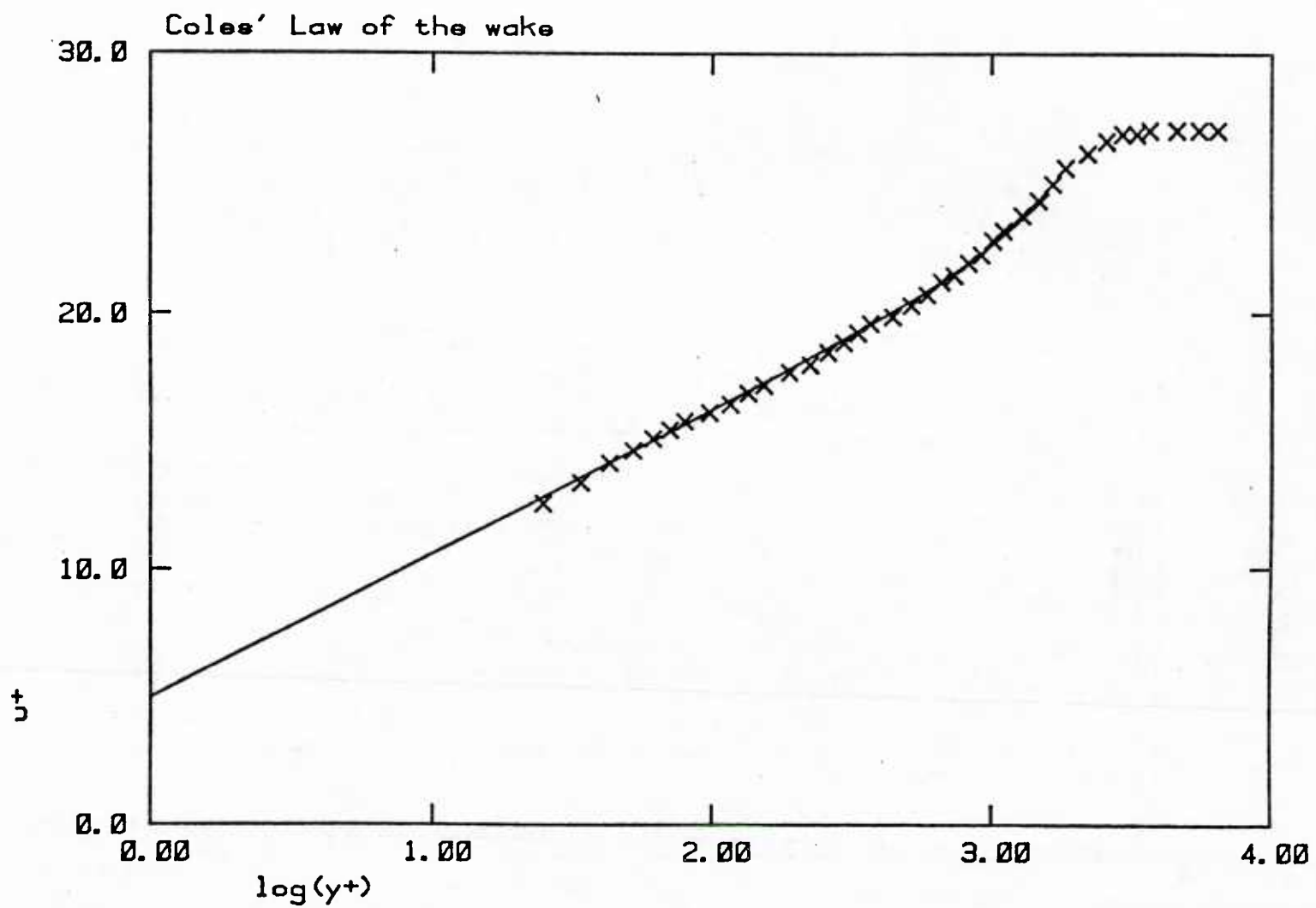


FIGURE 3.5 Boundary Layer Measurement Comparison

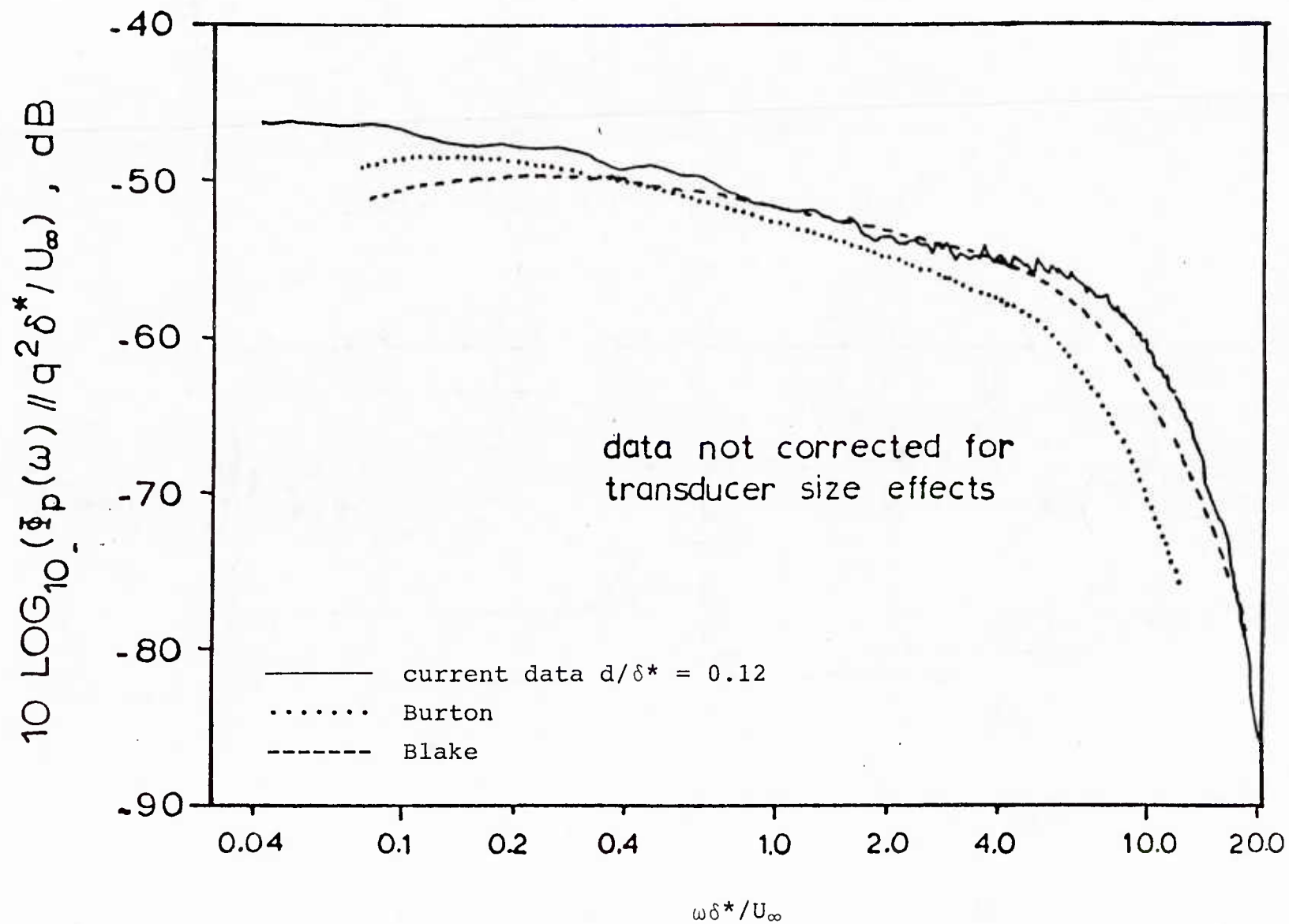


Figure 3.6. Single Point Wall Pressure Spectrum.

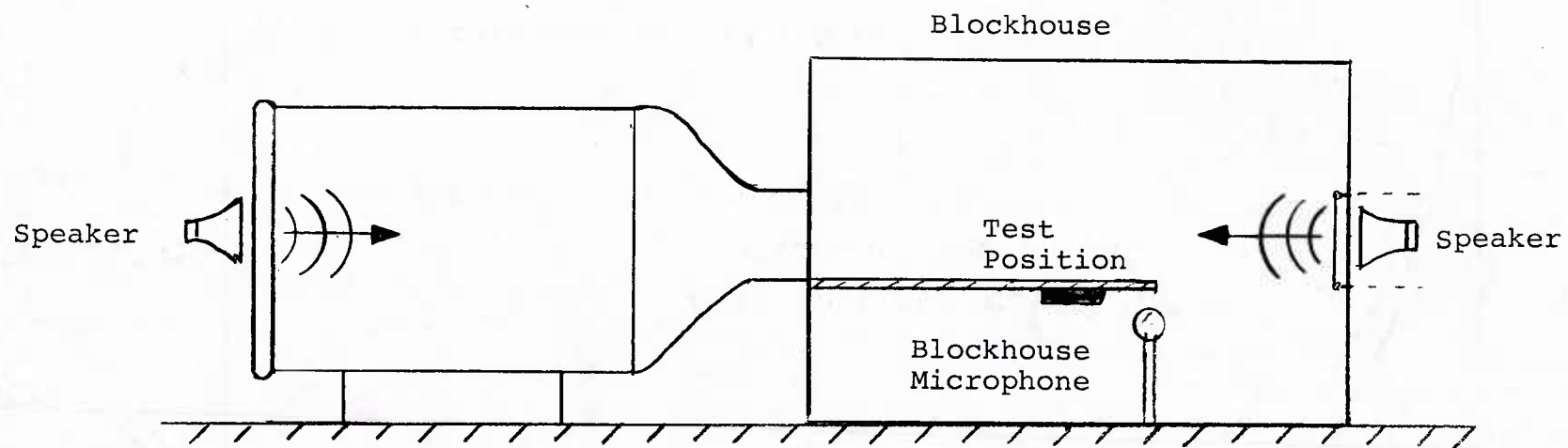


Figure 3.7. Acoustic Measurement Setup.

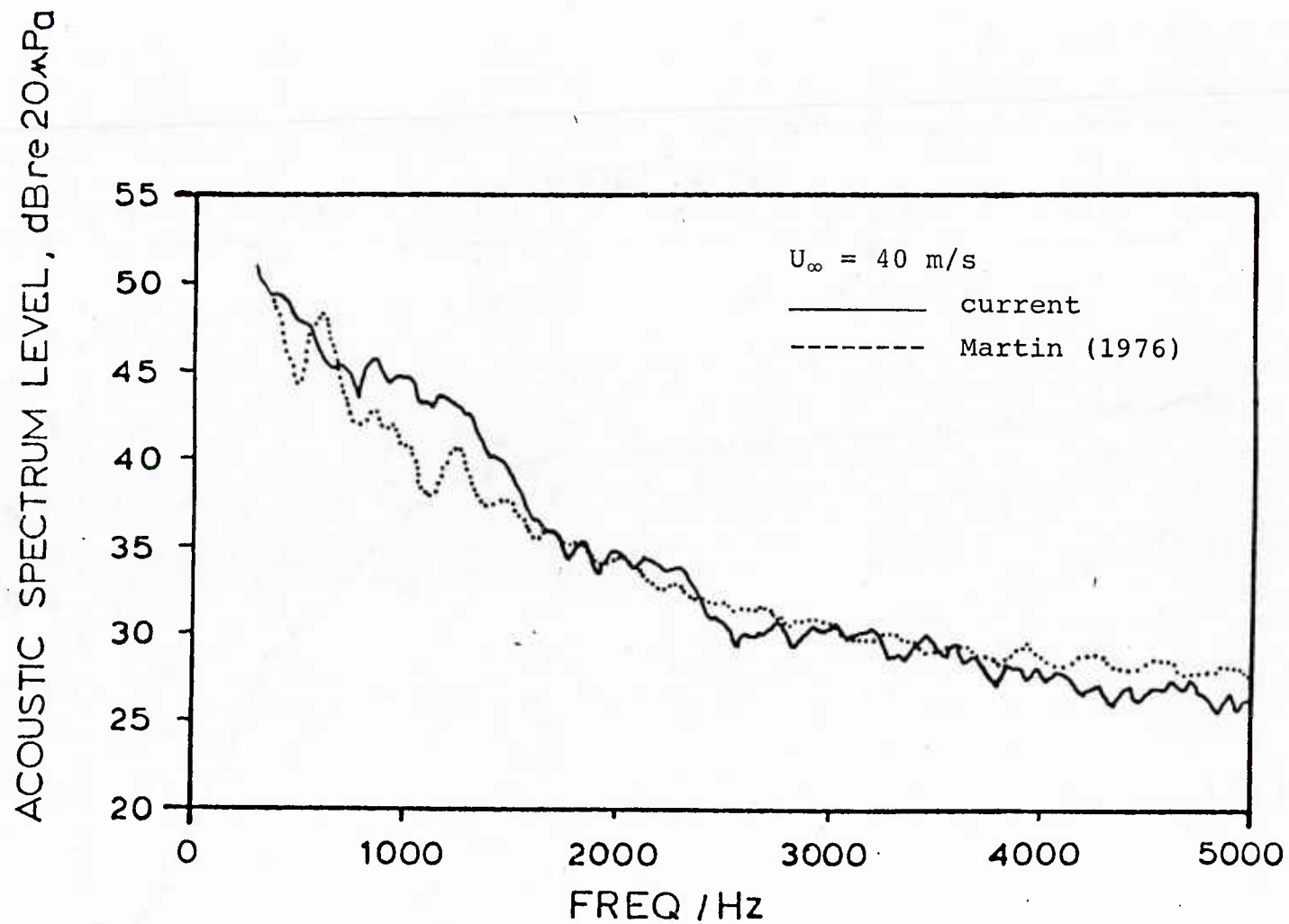


Figure 3.8. Spectrum Level Background Noise.

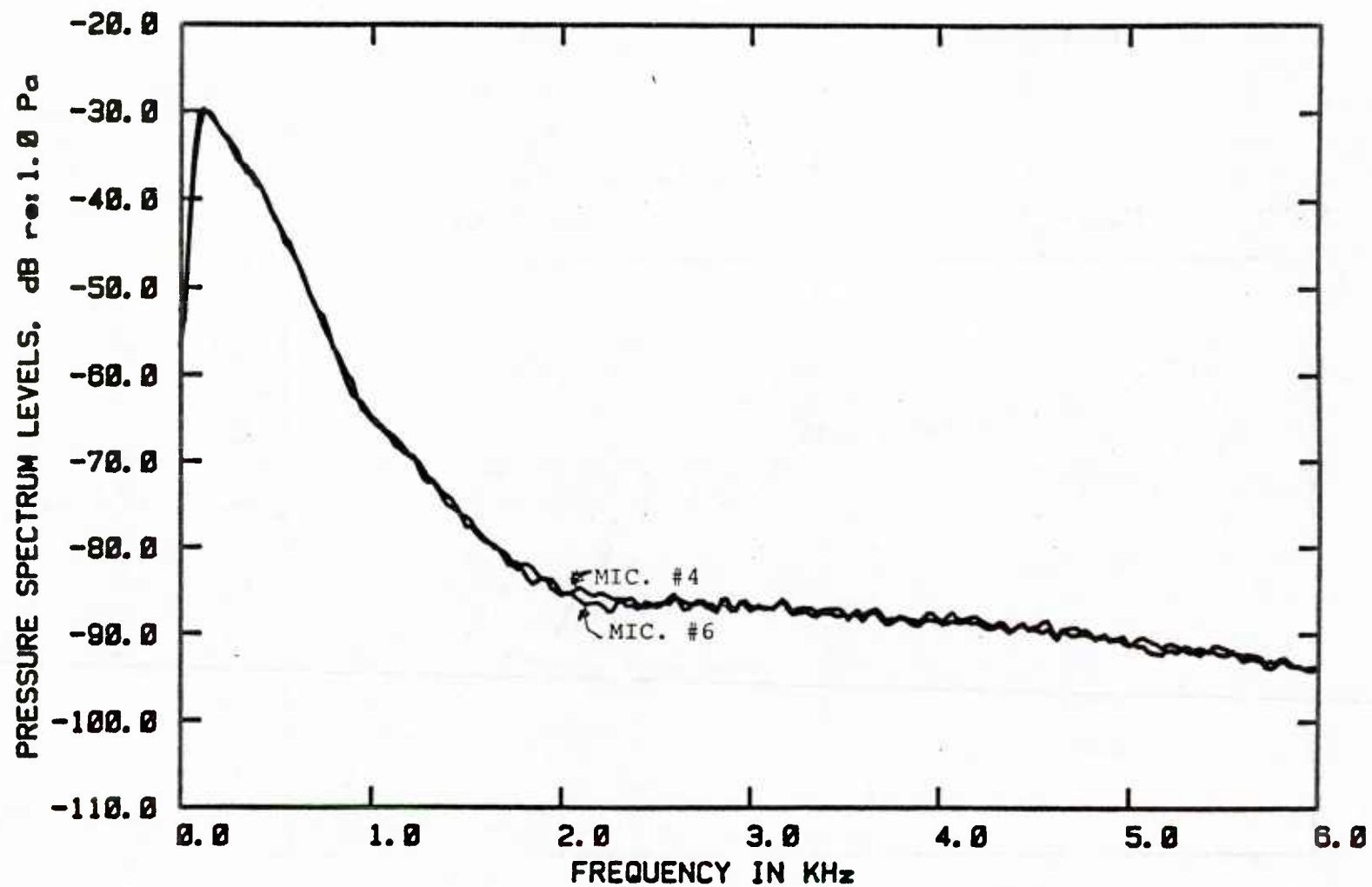


FIGURE 3.9 Comparison Between Two Flushed Mounted 1" Microphones @ 15 M/S.

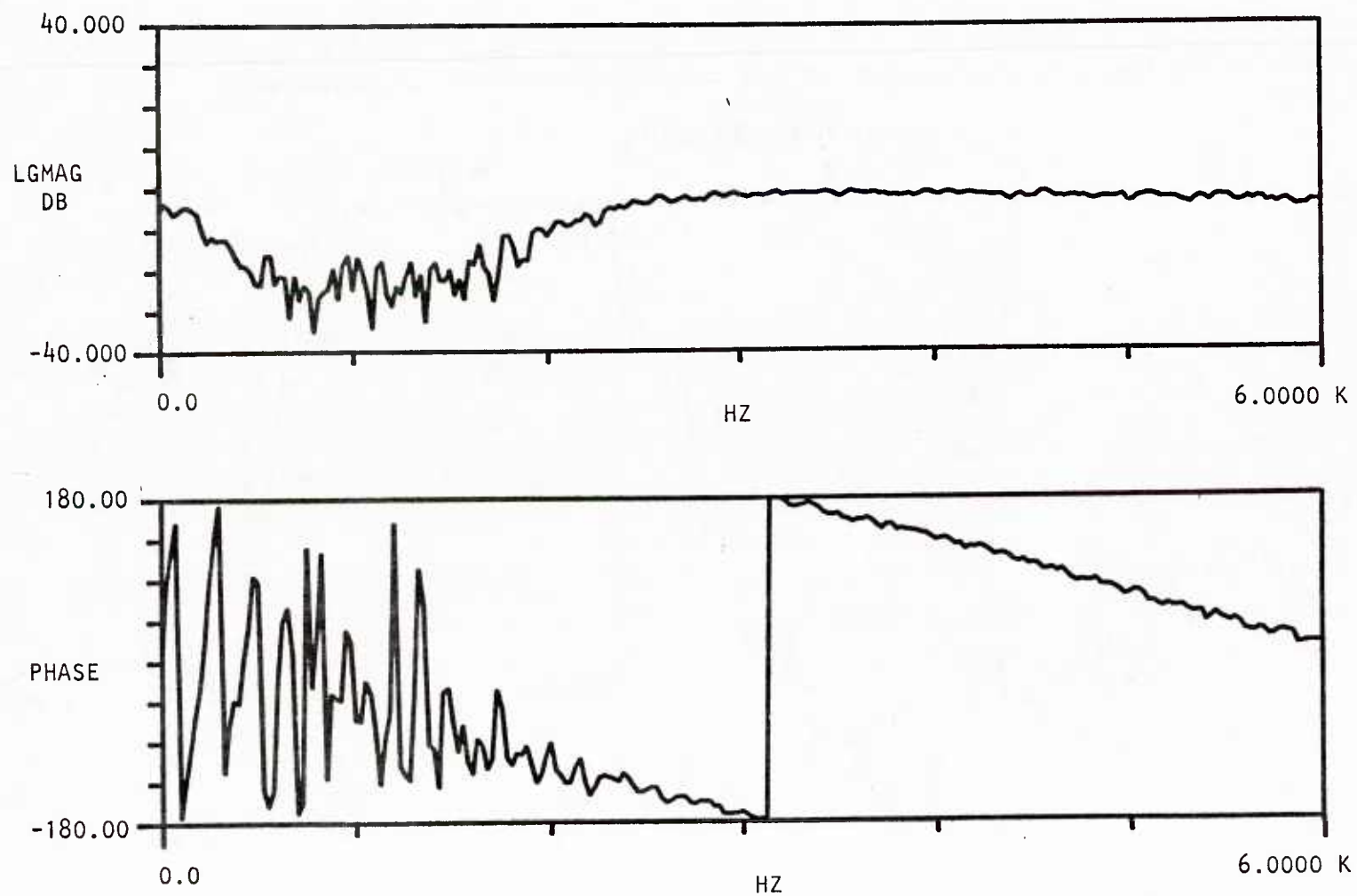


FIGURE 3.10 Cross Spectrum and Phase Between Two 1" Microphones @ 15 M/S.

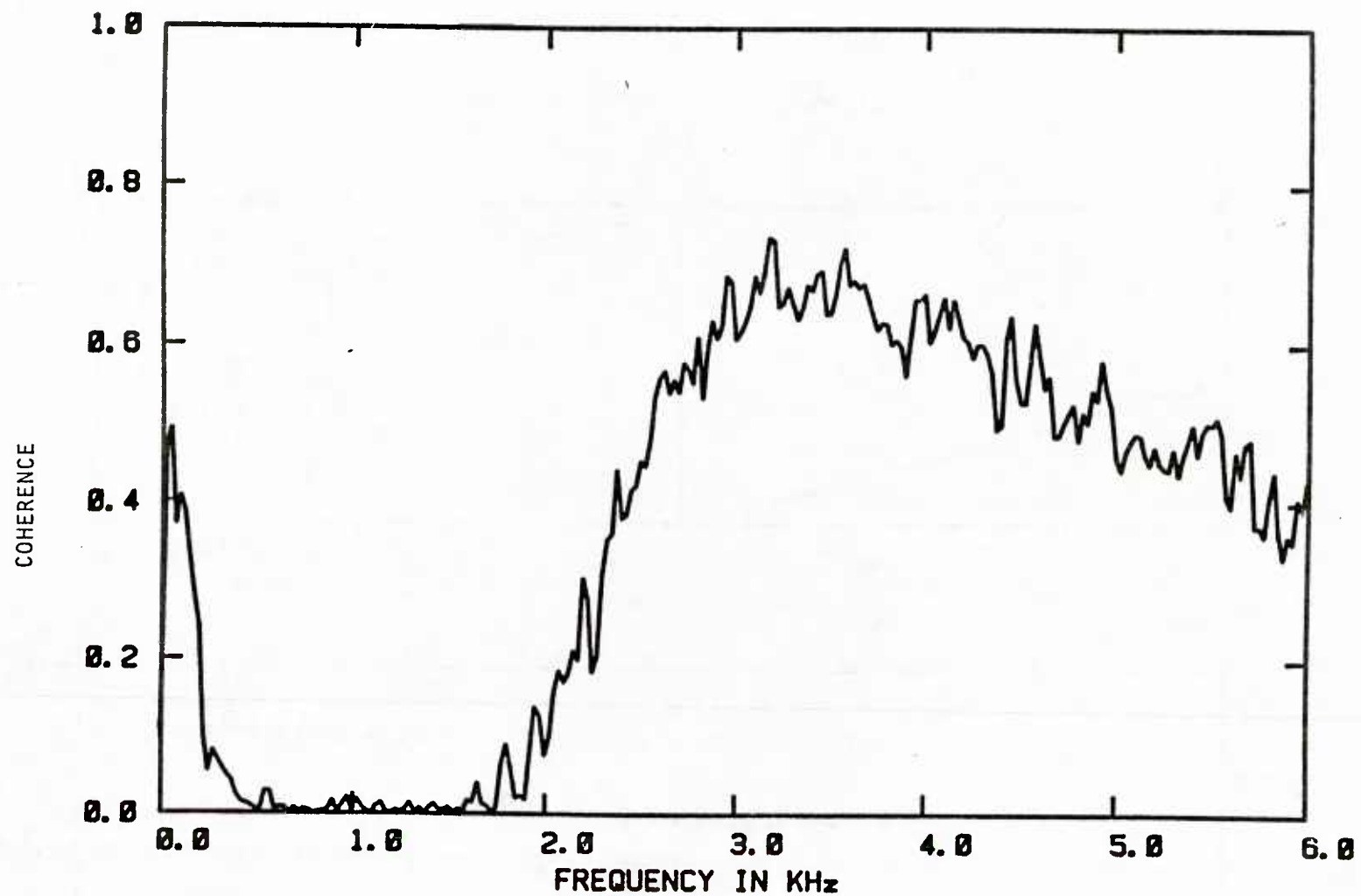


FIGURE 3.11 Coherence Between Two 1" Microphones @ 15 M/S.

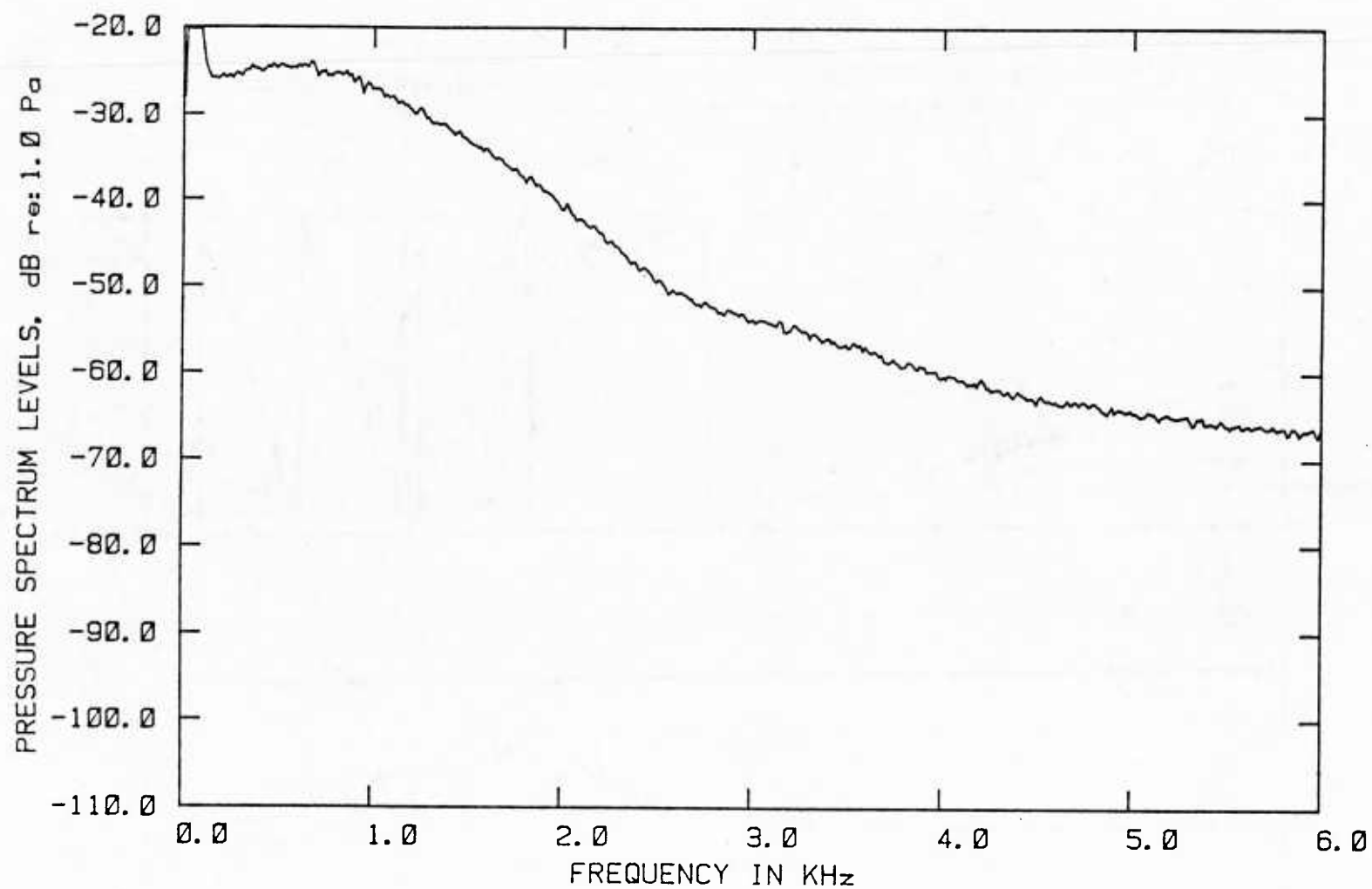


FIGURE 3.12 Single Point Wall Pressure Measurement @ 40 M/S.

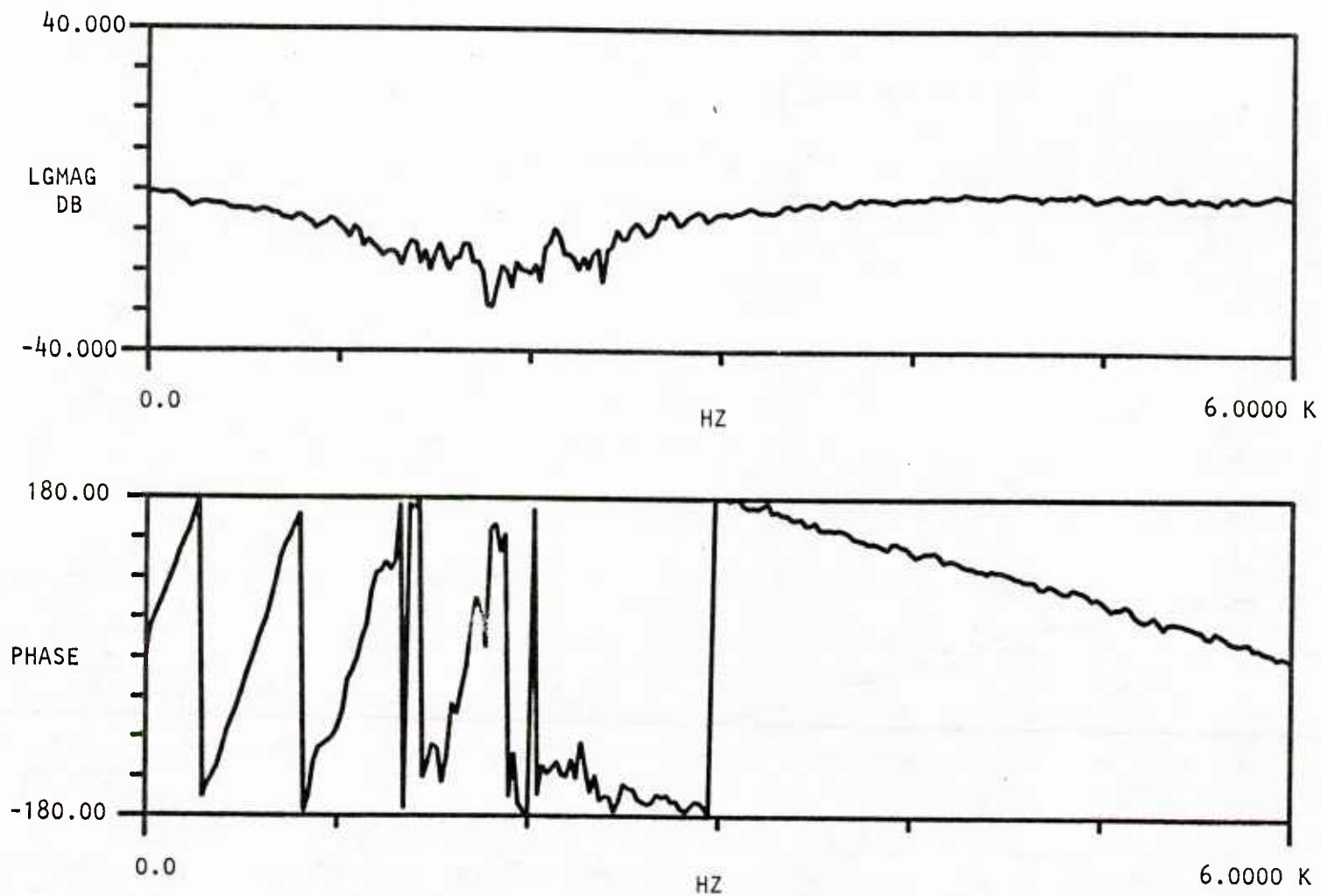


FIGURE 3.13 Cross Spectrum and Phase Relation Between Two Microphones
@ 40 M/S.

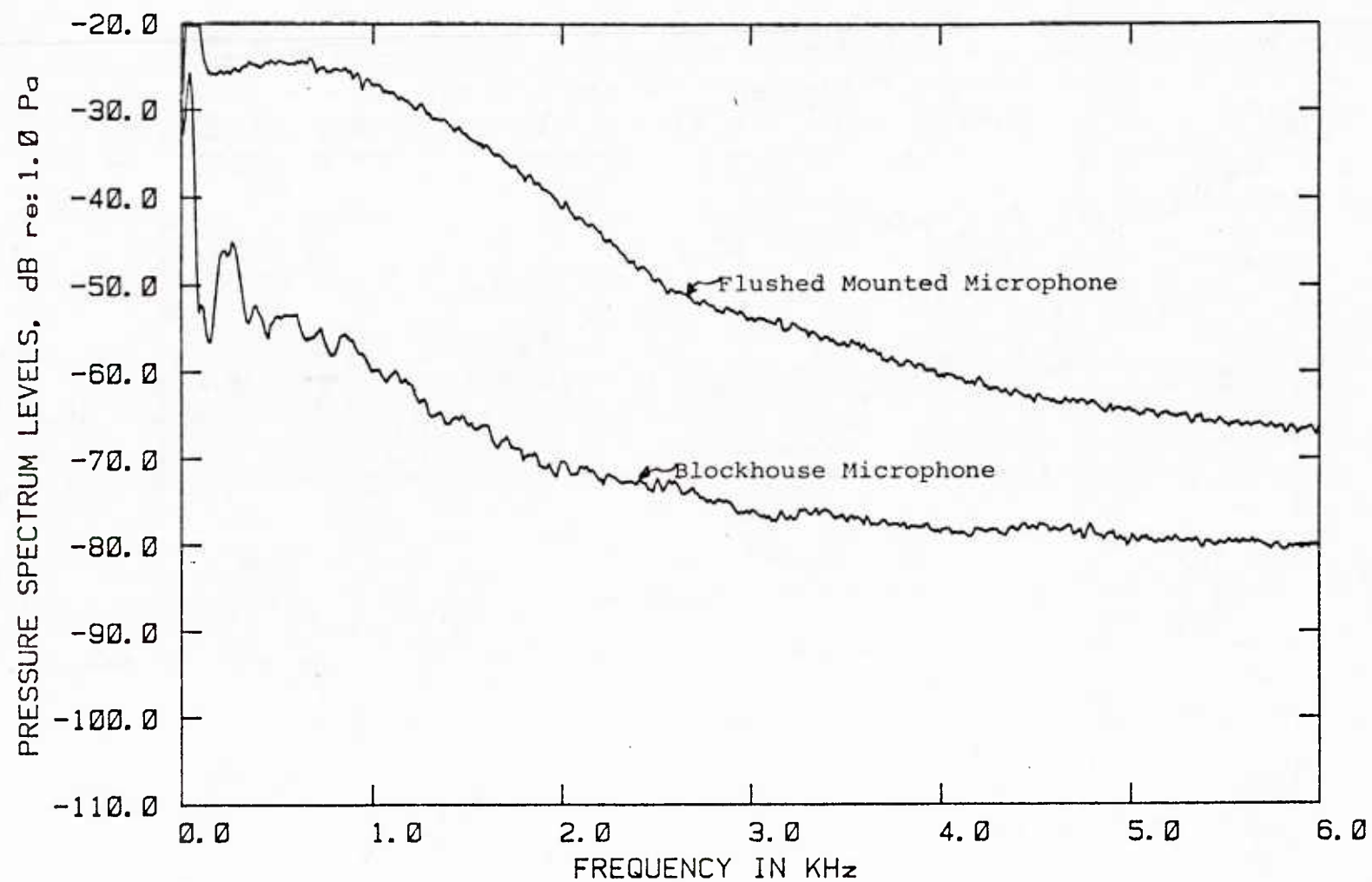


FIGURE 3.14 Comparison Between Blockhouse Noise Measurements and Flush Mounted Microphone @ 40 M/S.

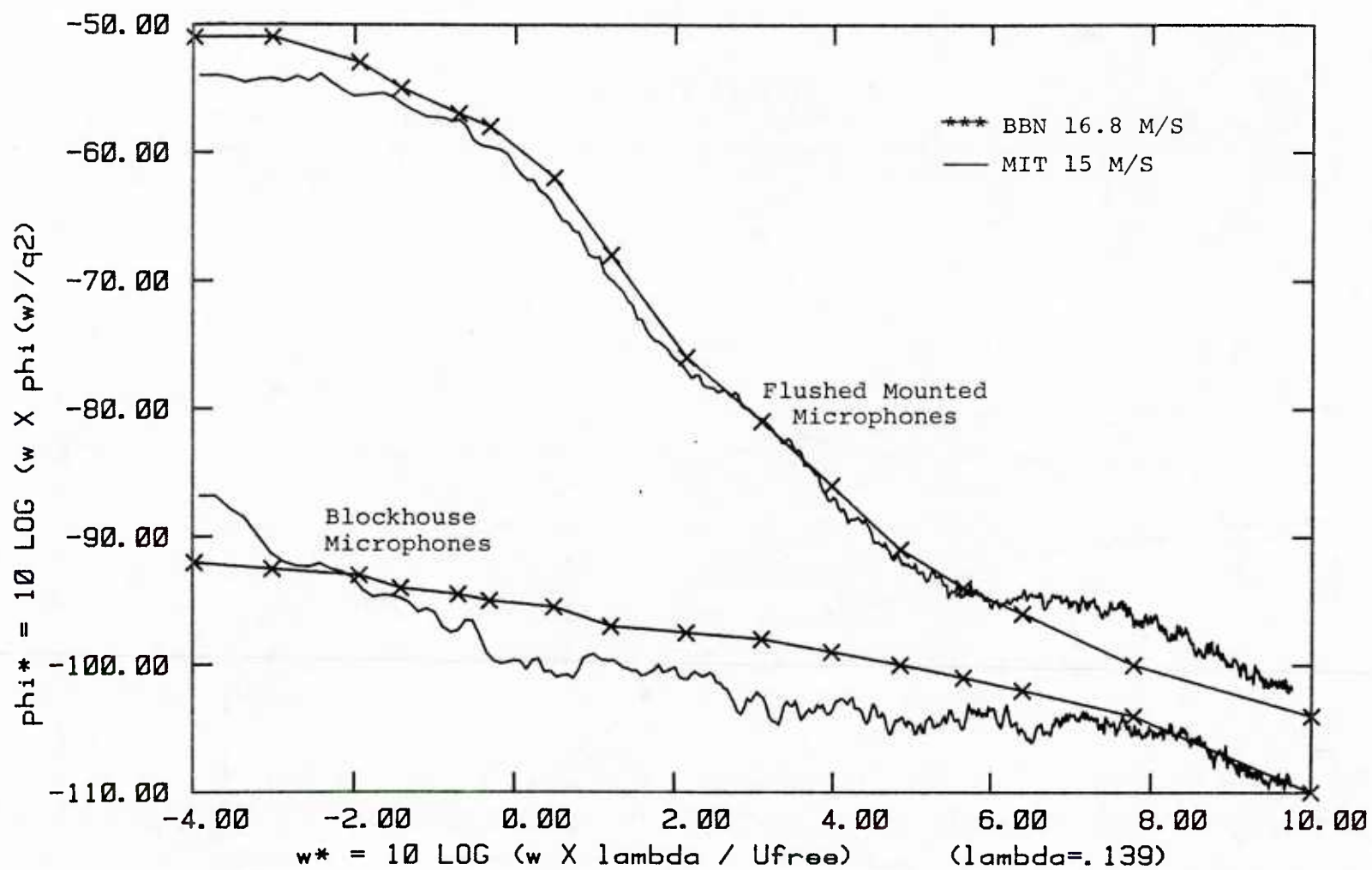


FIGURE 3.15 Comparison of M.I.T. Facility With BBN Facility.

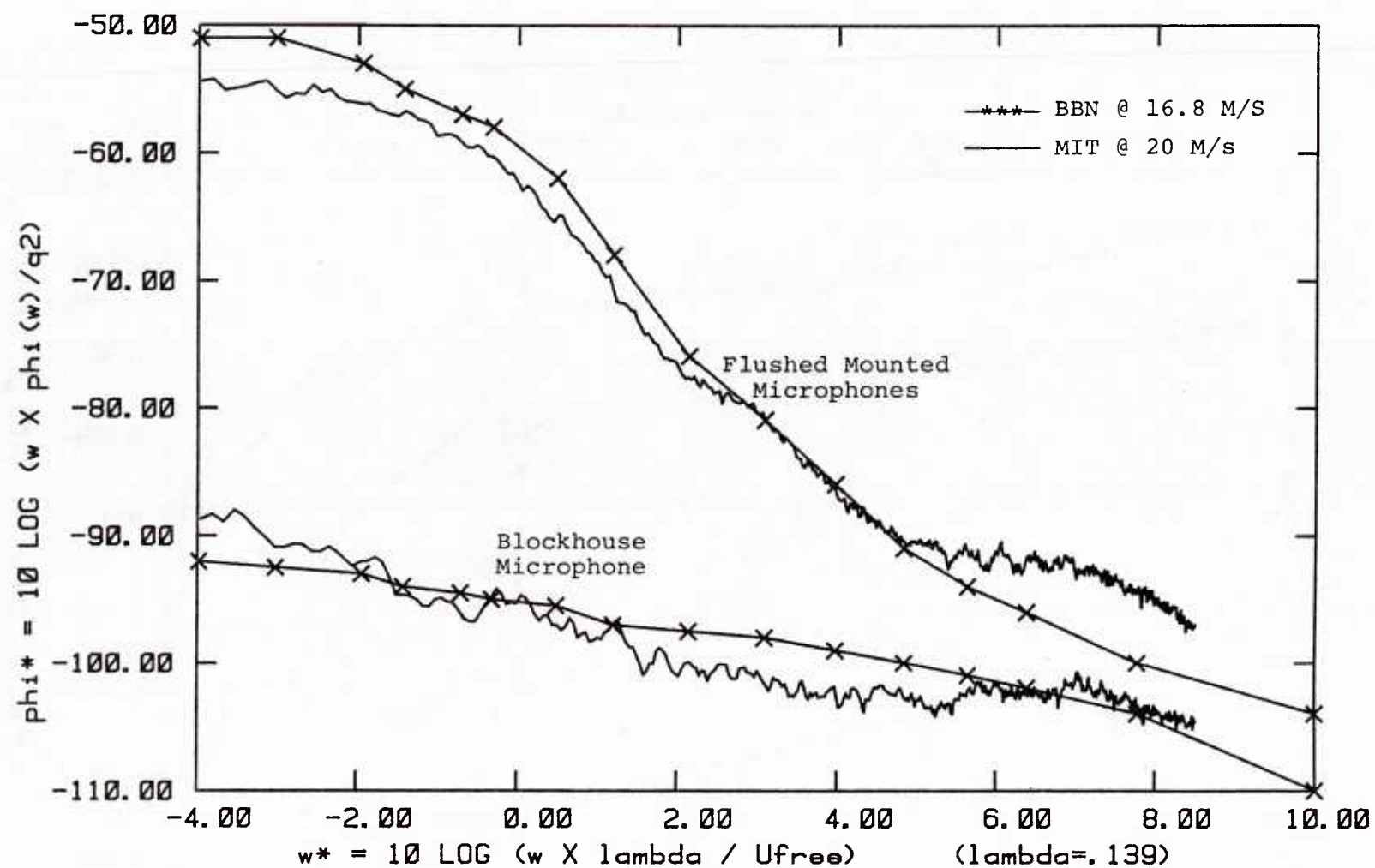


FIGURE 3.16 Comparison of M.I.T. Facility With BBN Facility.

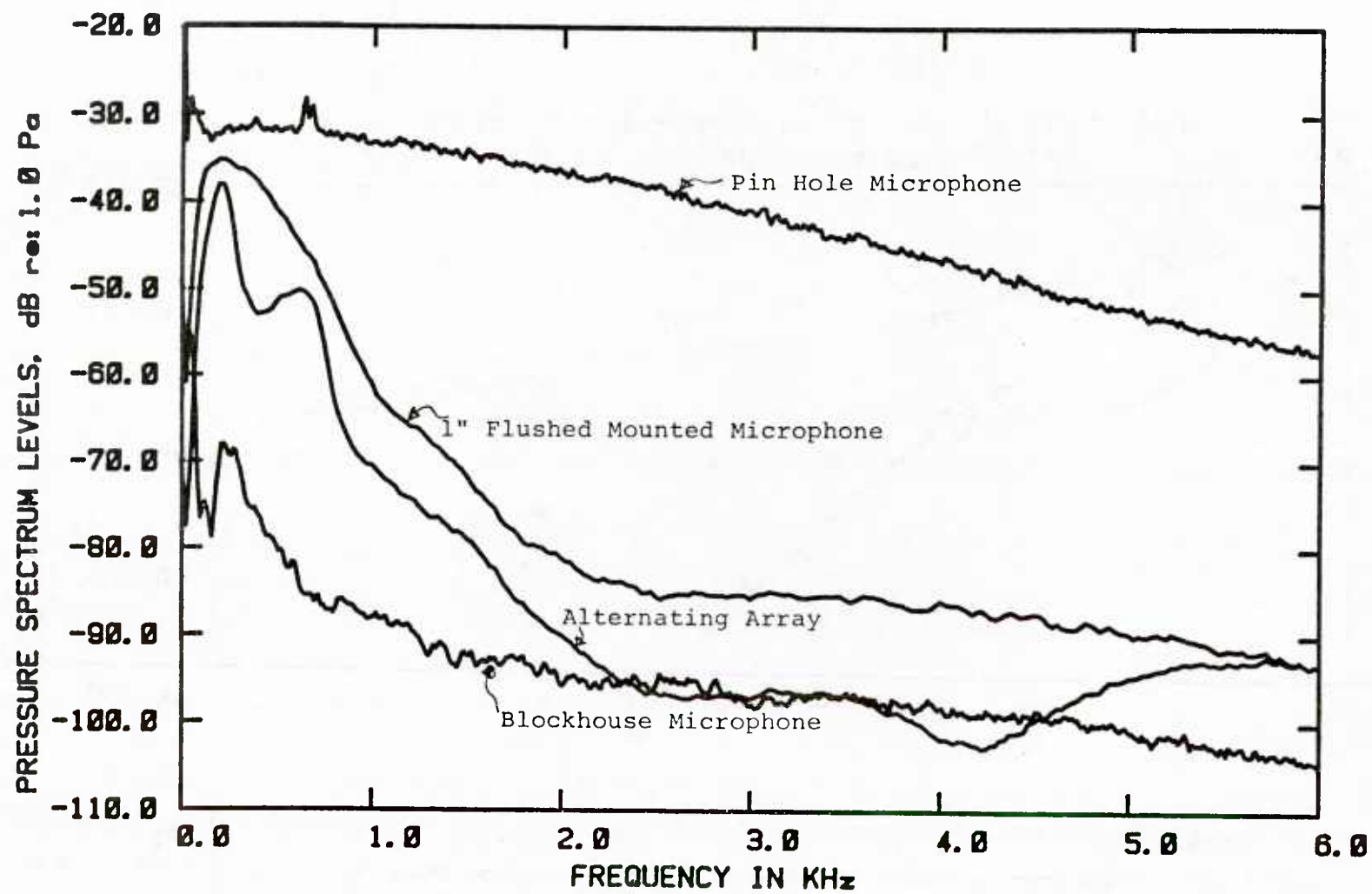


FIGURE 4.1 Comparison of Various Microphone Measurements @ 15 M/S.

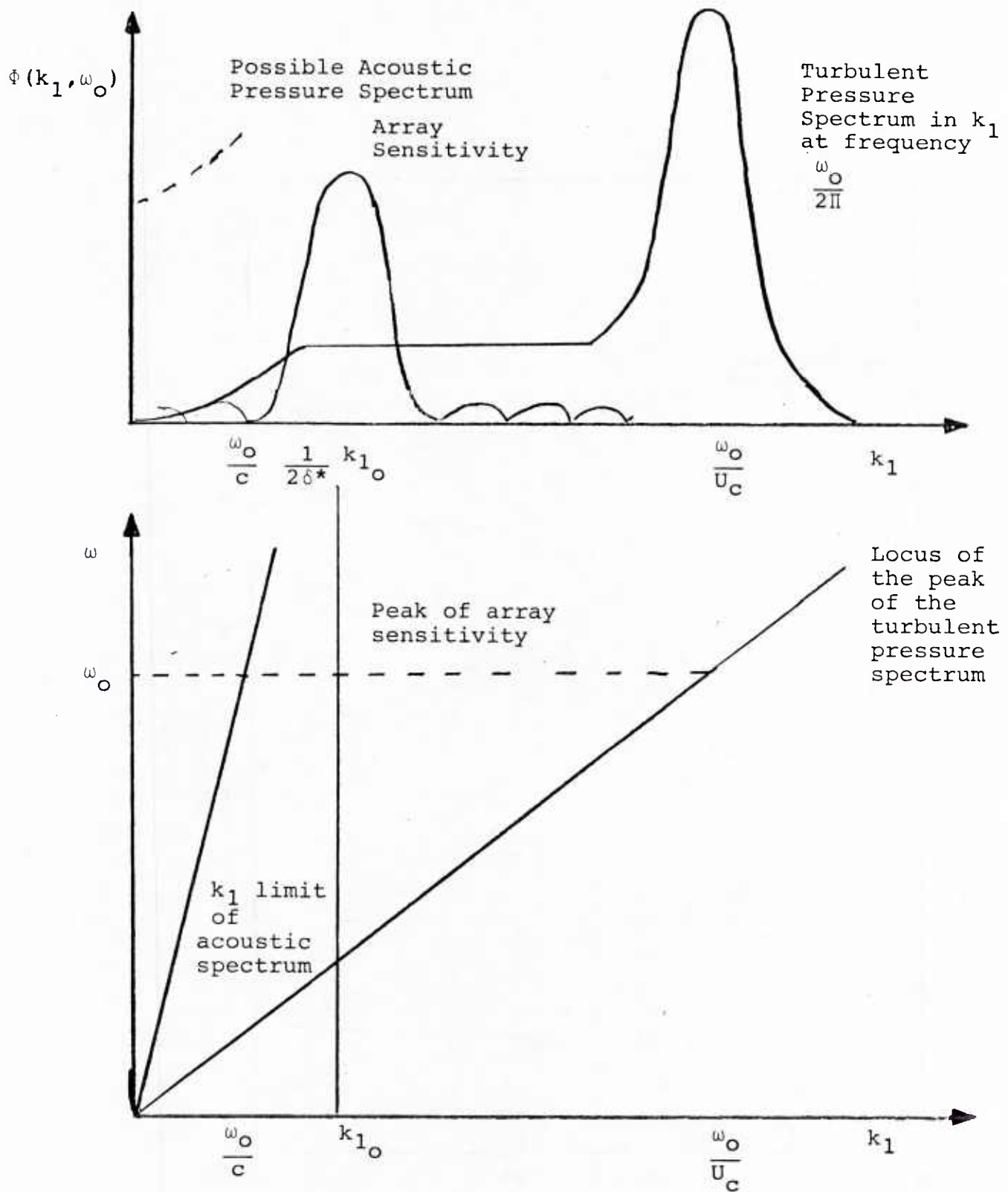


Figure 4.2. Schematic of the Relationship among the Turbulent, Array, and Acoustic Pressure Spectra at Fixed Frequency $\omega_0/2\pi$.

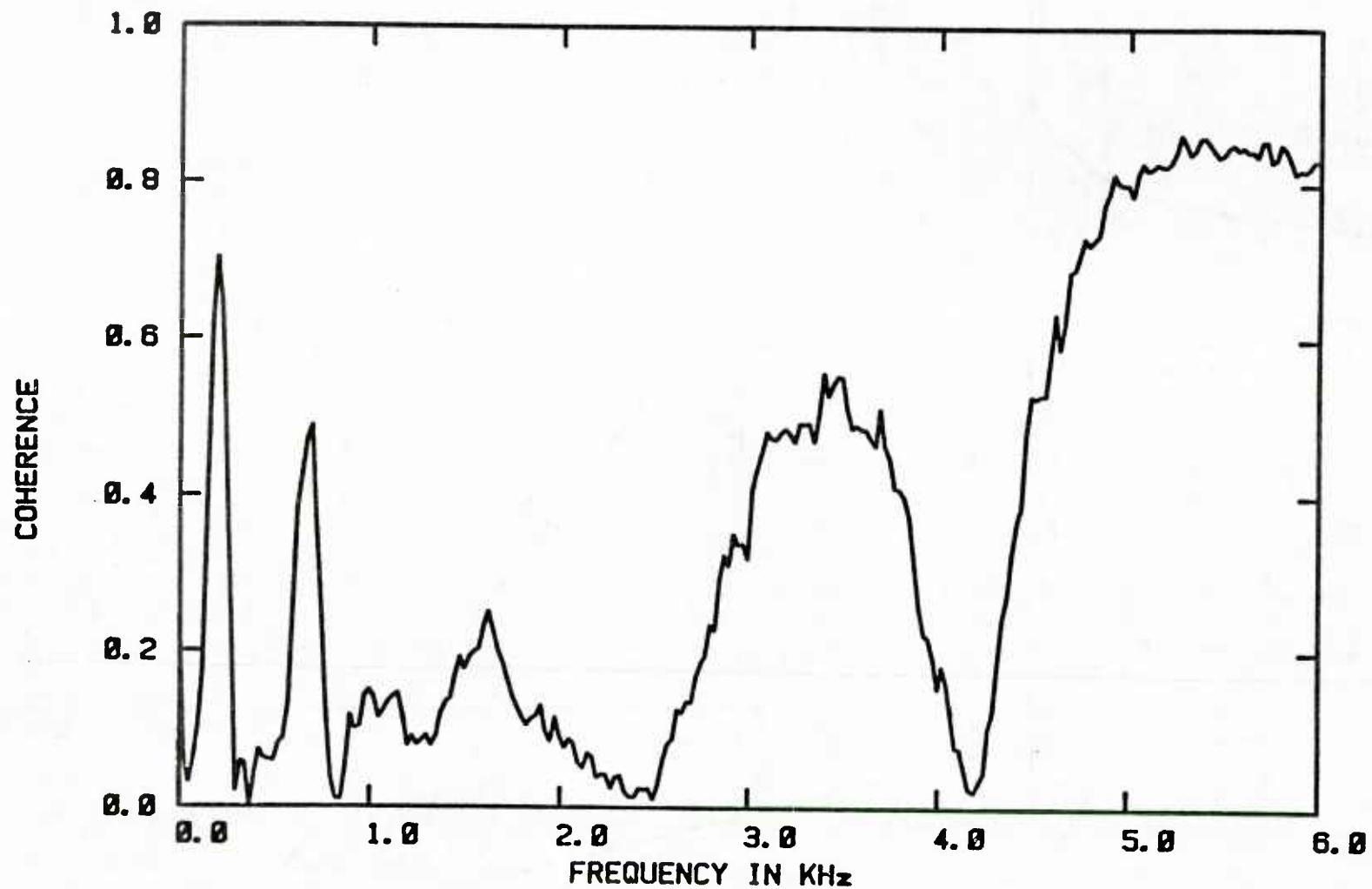


FIGURE 4.3 Coherence Between the Array and a Single Microphone in the Array @ 15 M/S.

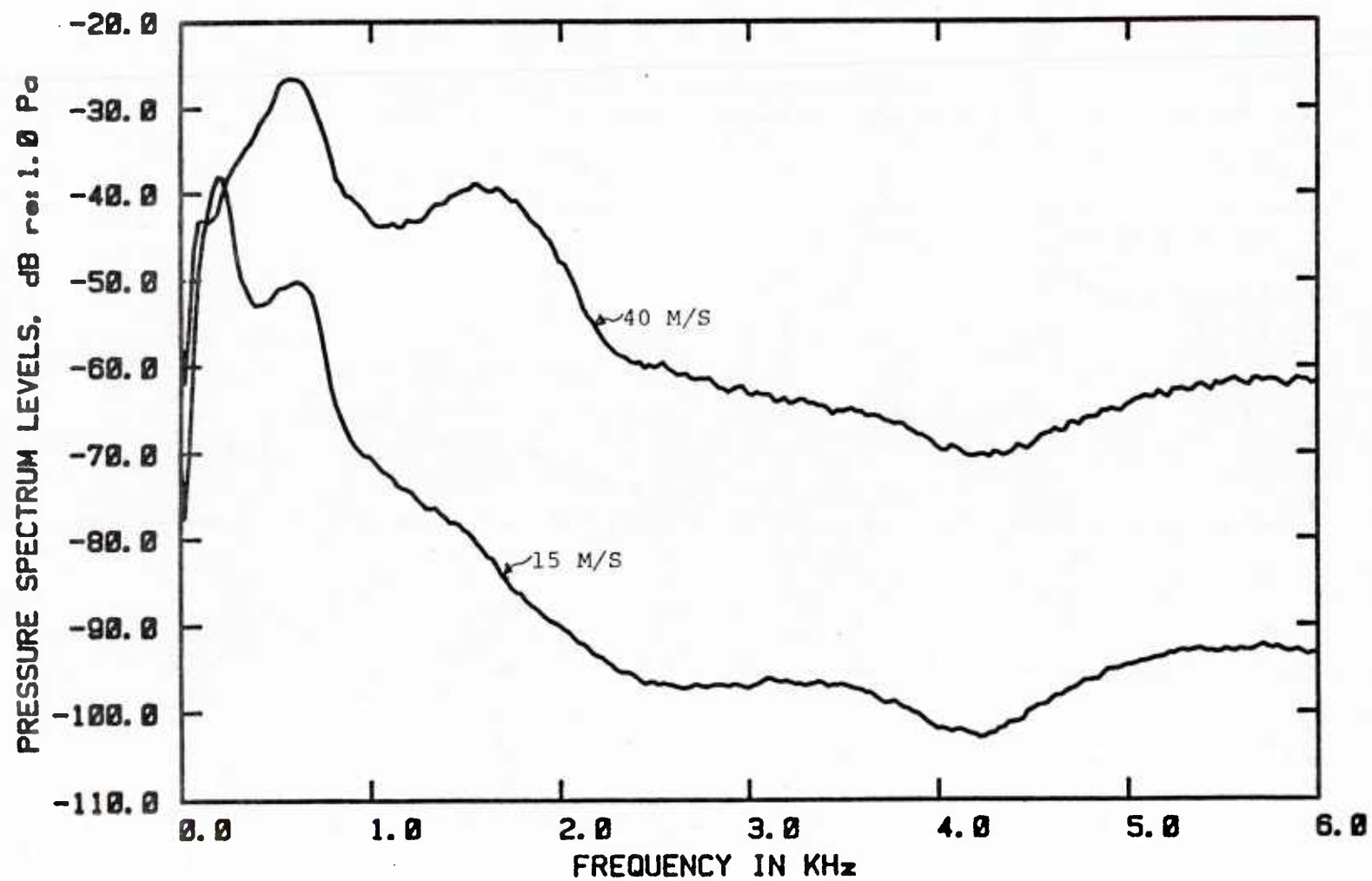


FIGURE 4.4 Comparison of Alternating Phased Array @ 15 M/S and 40 M/S.

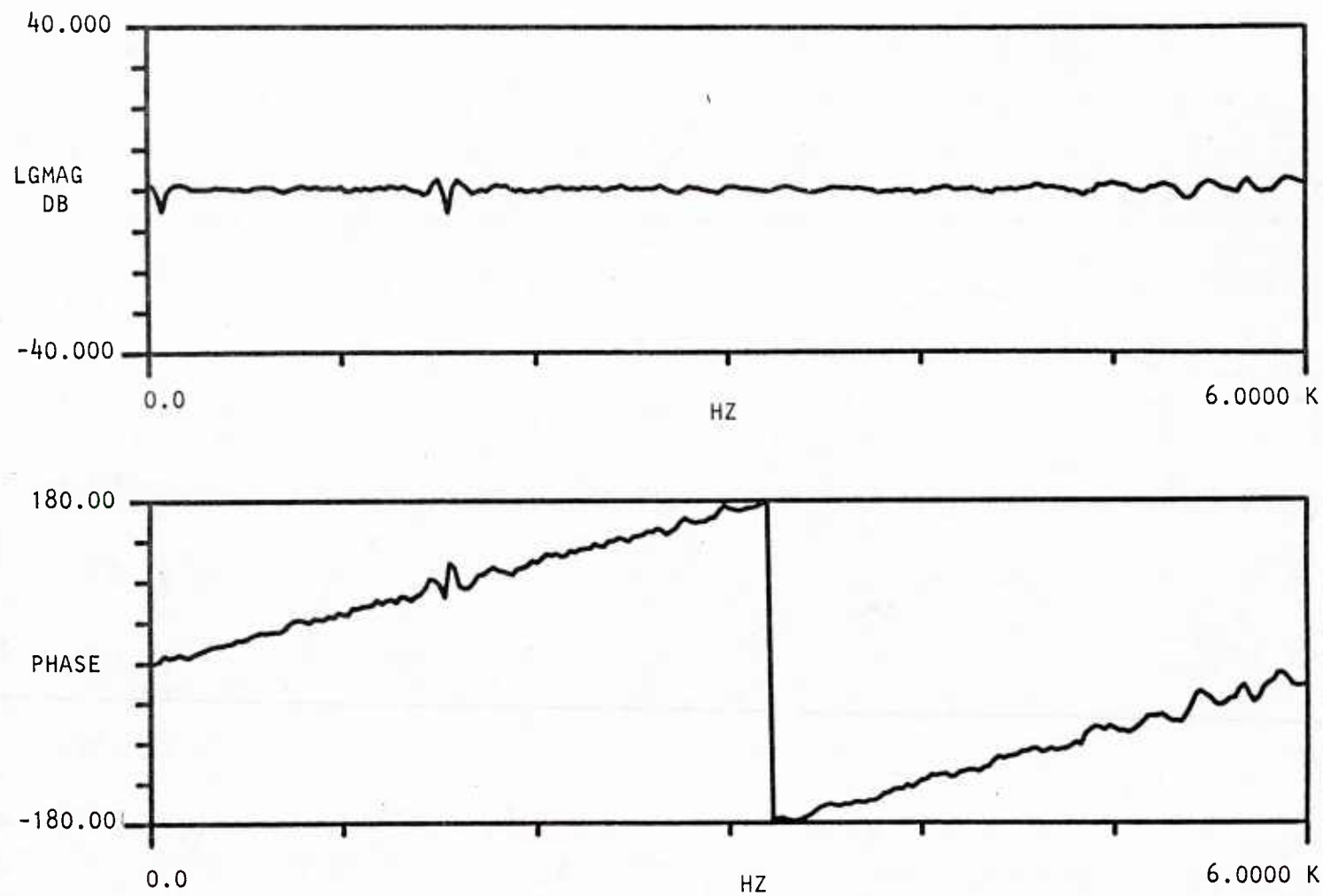


FIGURE 4.5 Cross Spectrum and Phase Relation Between Two Microphones
Excited by a Plane Acoustic Wave.

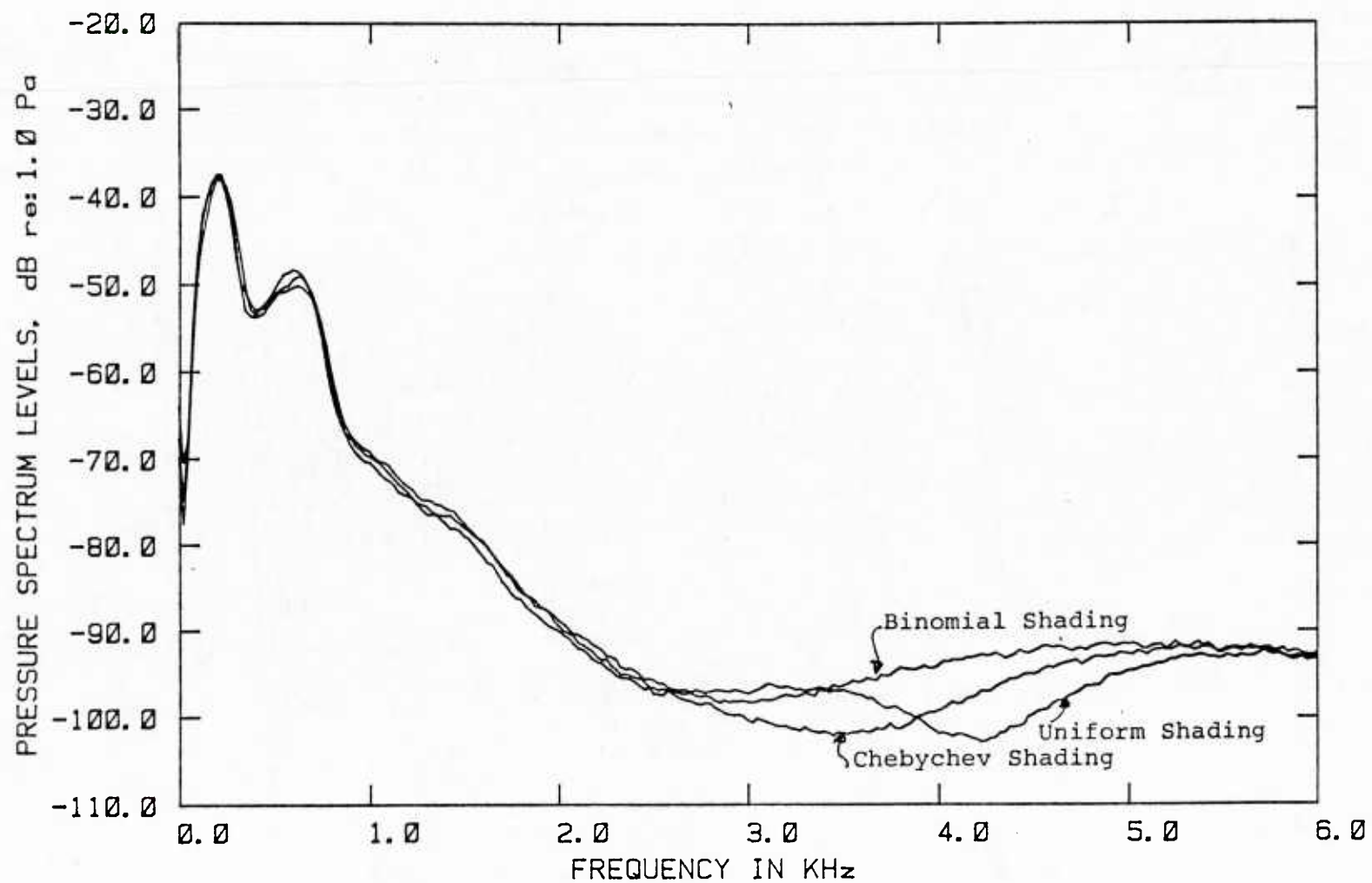


FIGURE 4.6 Comparison of the Alternating Phased Array Response for Various Shading @ 15 M/S.

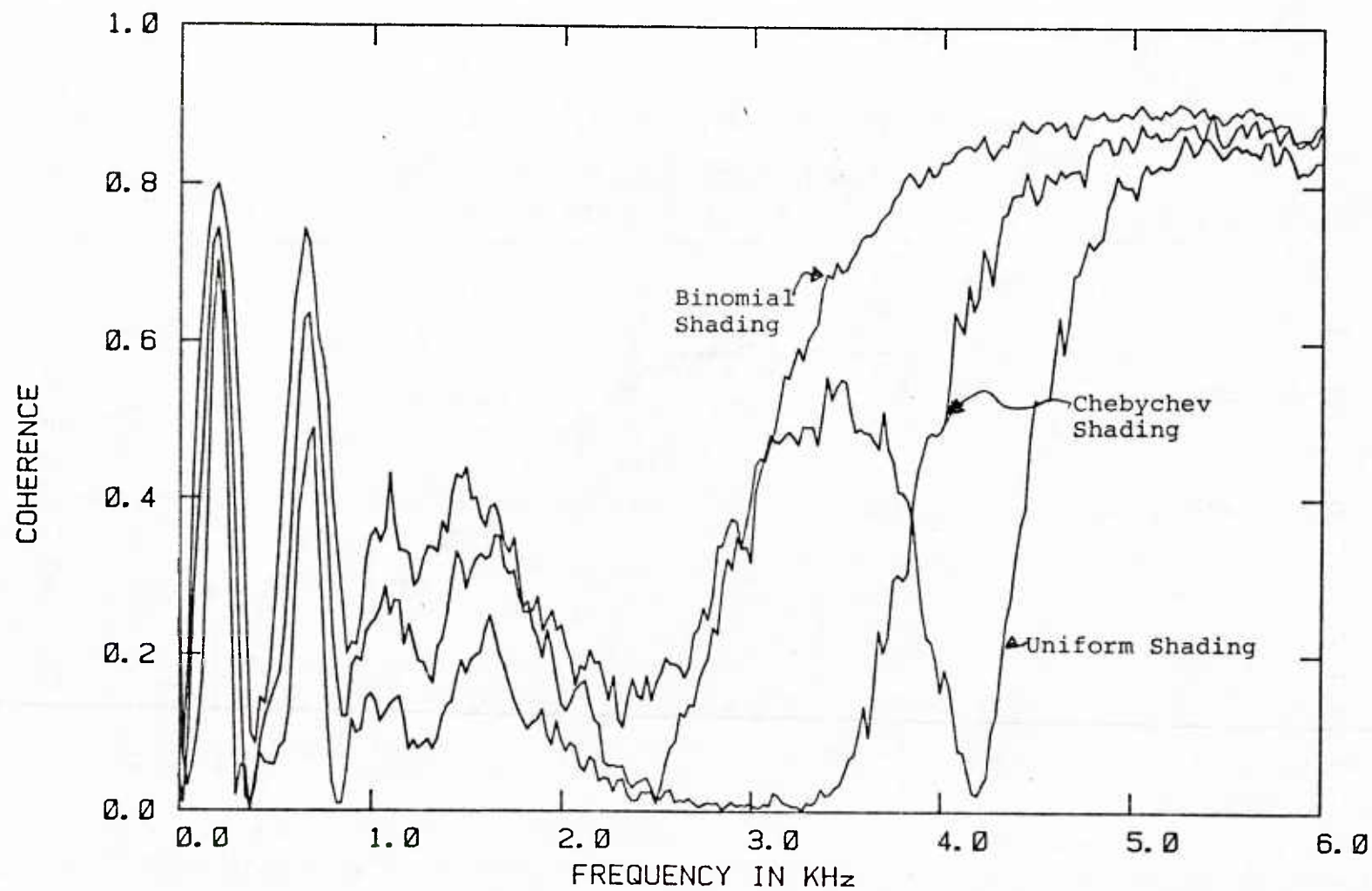


FIGURE 4.7 Comparison of Coherence for Various Shadings.

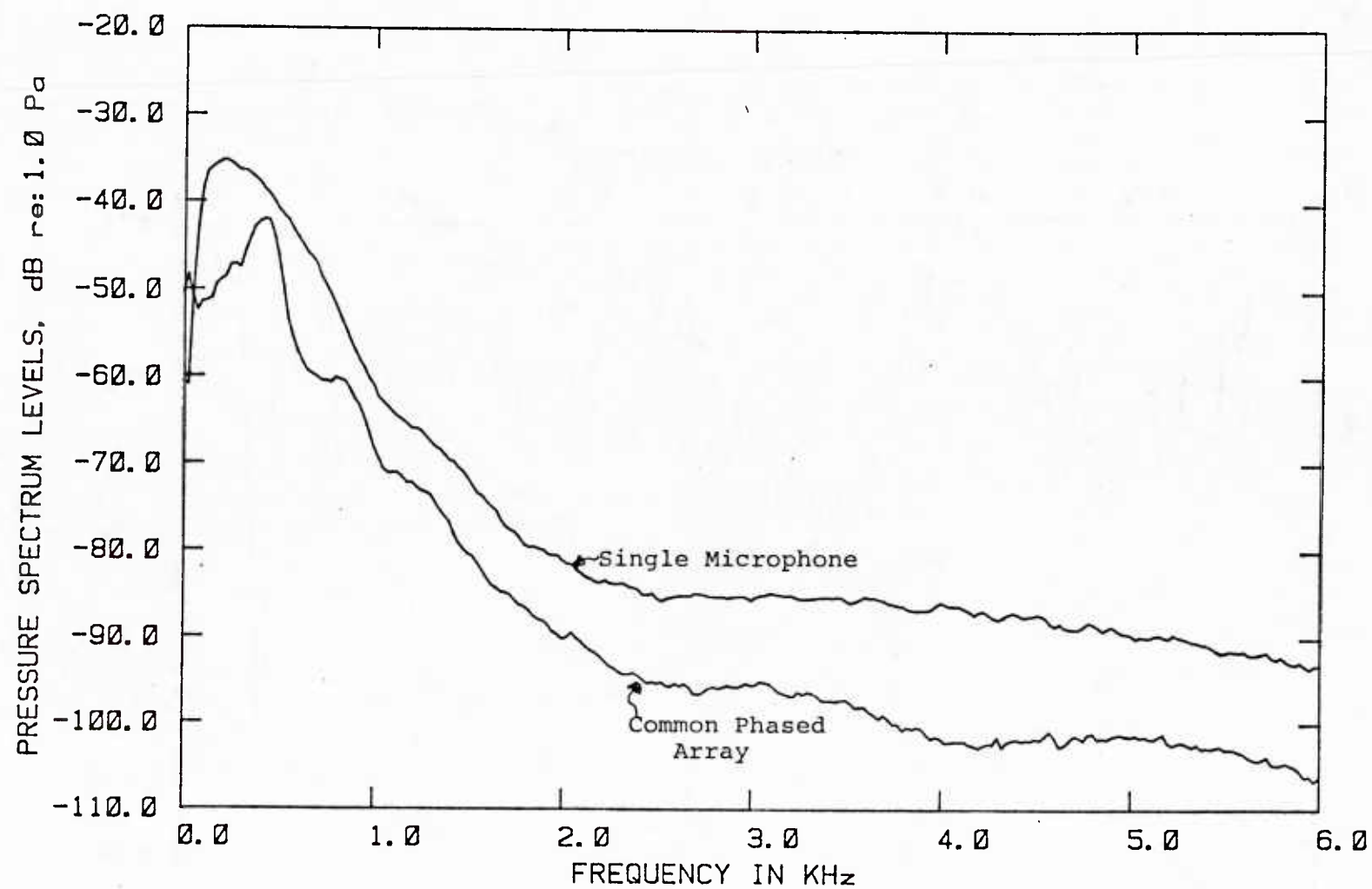


FIGURE 4.8 The Common Phased Array Response @ 15 M/S.

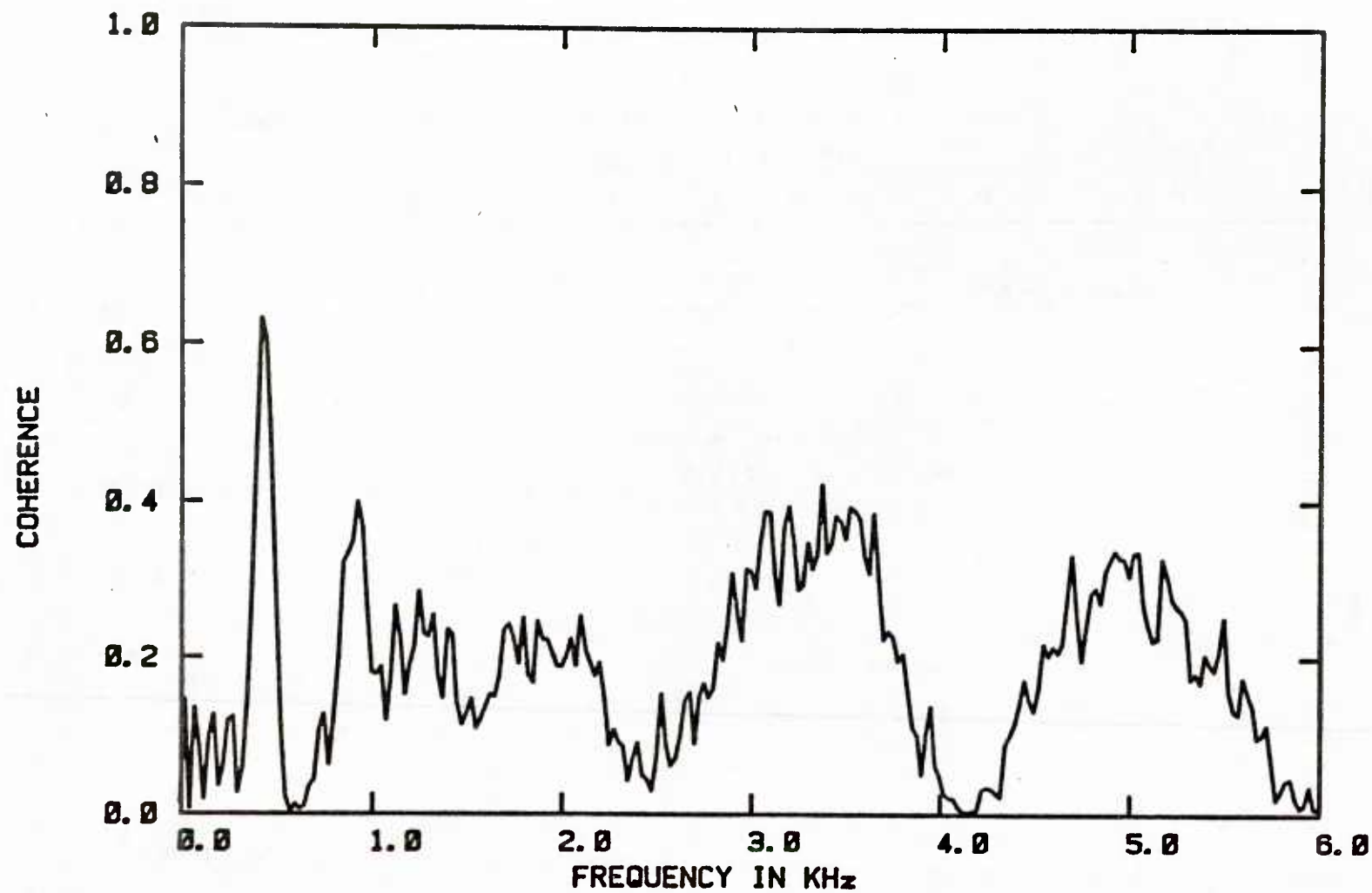


FIGURE 4.9 Coherence of Common Phased Array @ 15 M/S.

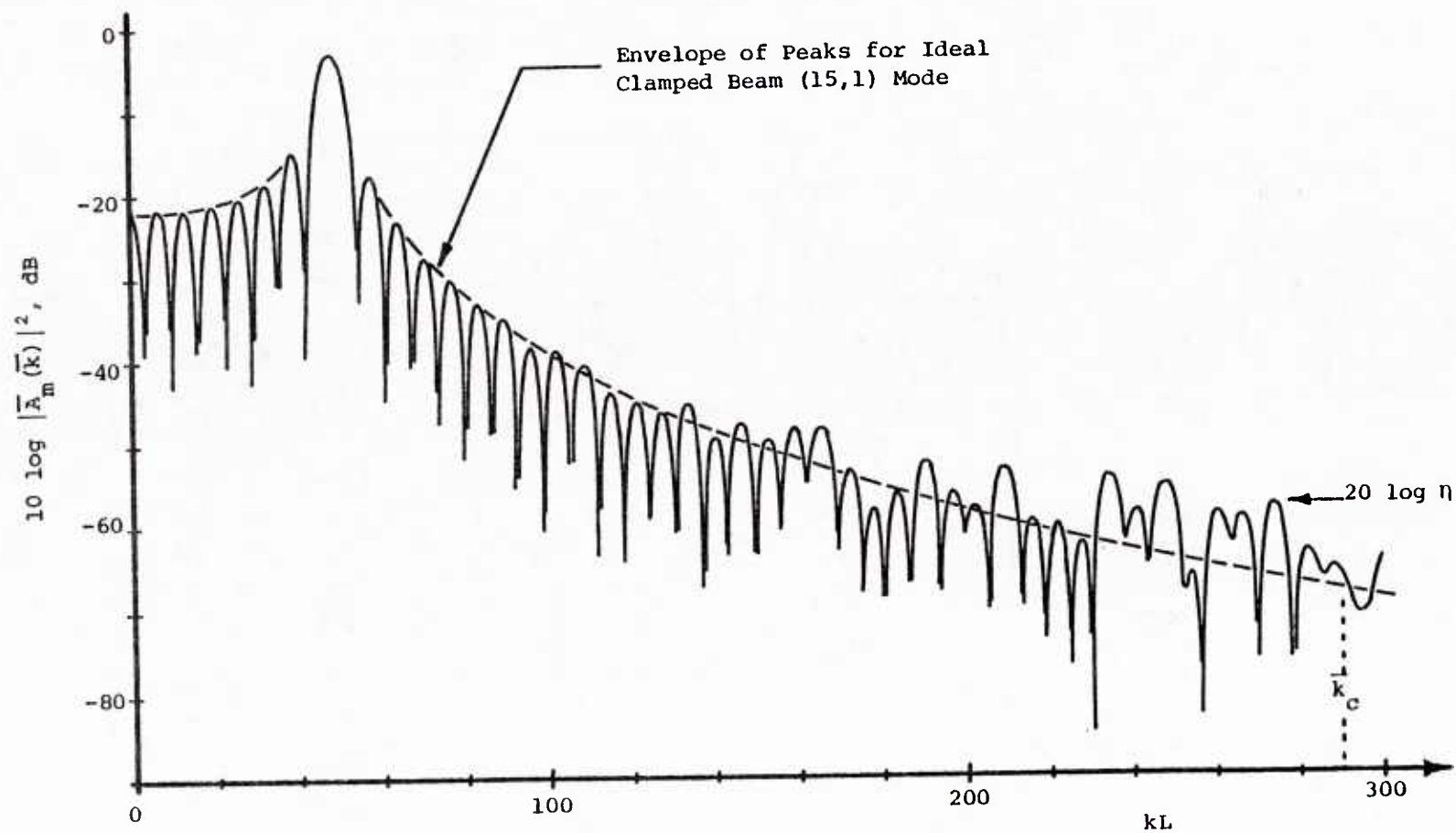


FIGURE 4.10 Measured $|\bar{A}_m(\bar{k})|^2$: (15,1) Mode of the Clamped Plate,
 \bar{k}_c = Typical Convective Wavenumber ($U_\infty = 40$ m/sec).
 (By Permission from Martin)

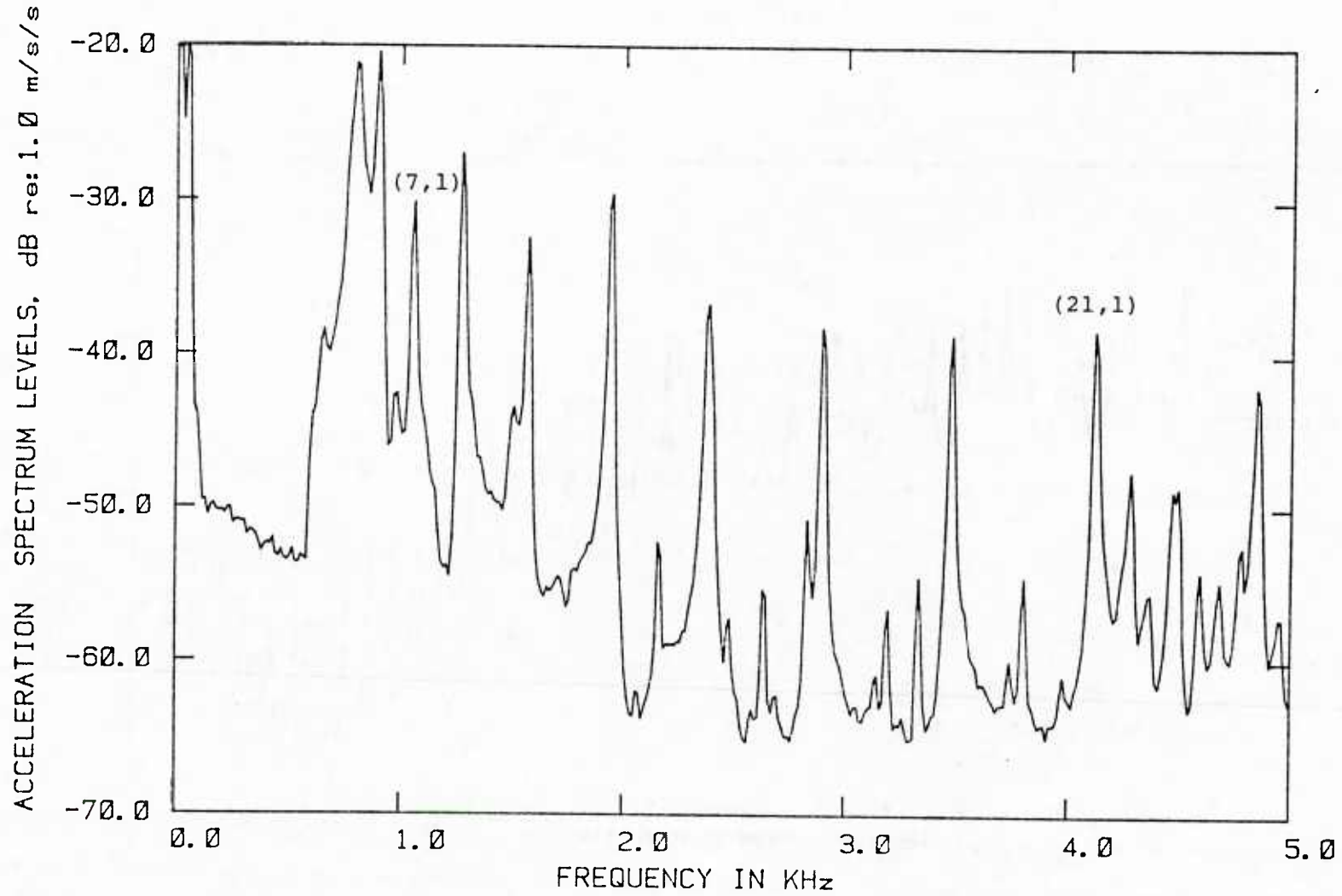


FIGURE 4.11 Measured Acceleration Spectrum of Martin Plate @ 40 M/S.

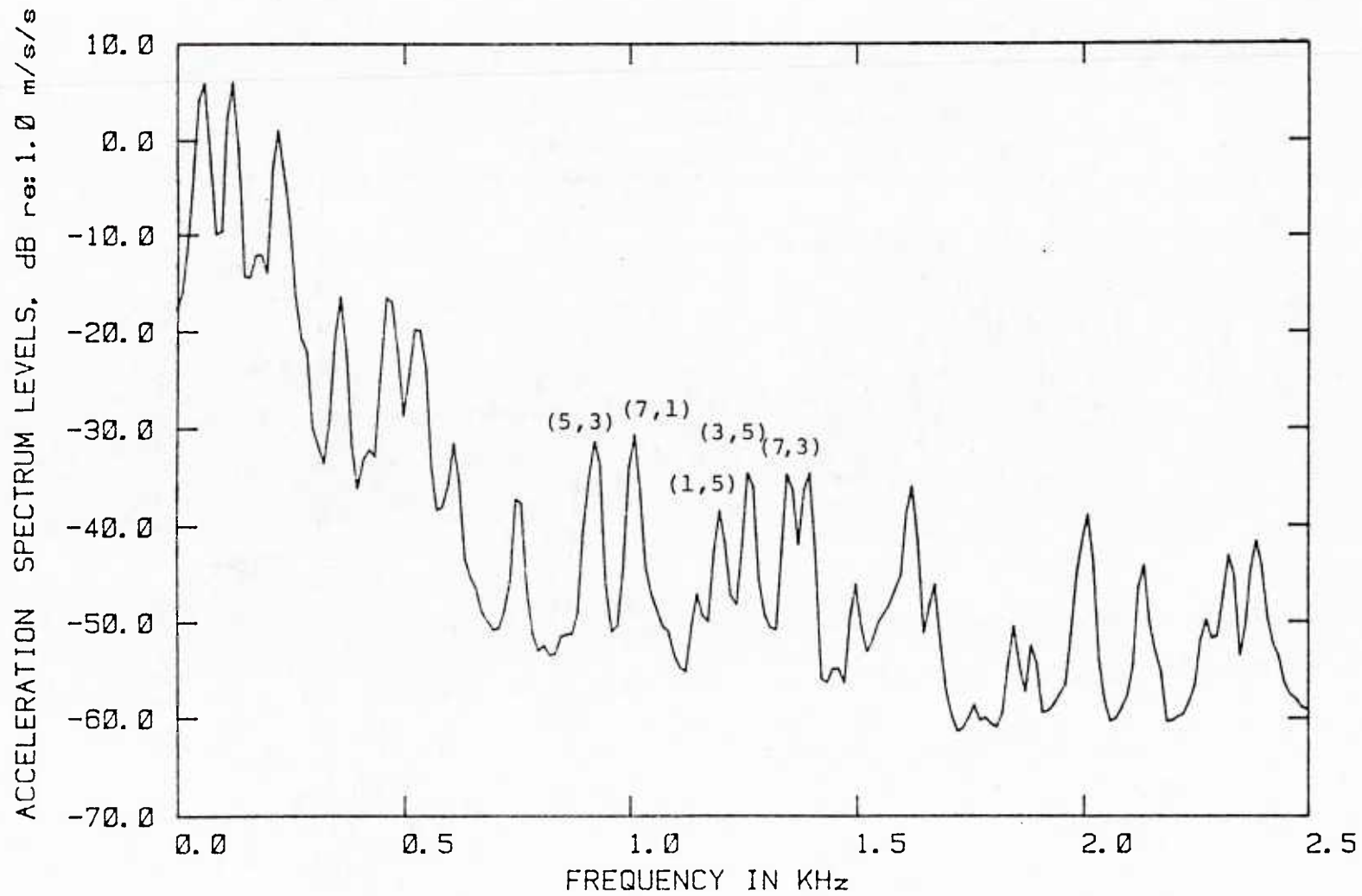


FIGURE 4.12 Measured Acceleration Spectrum of (odd,odd) Modes of Jameson Plate @ 40 M/S.

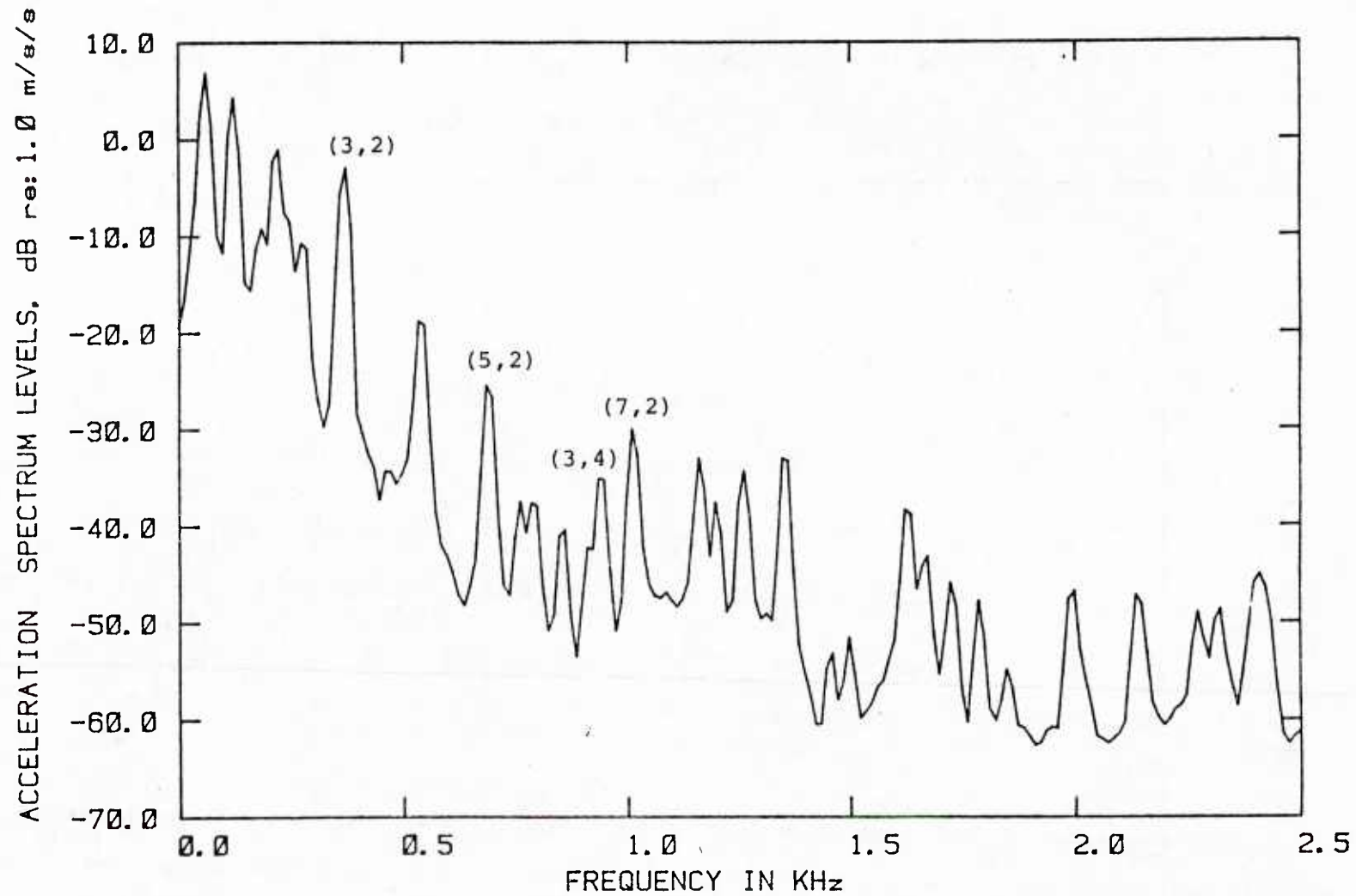


FIGURE 4.13 Measured Acceleration Spectrum of (odd,2) Modes of Jameson Plate @ 40 M/S.

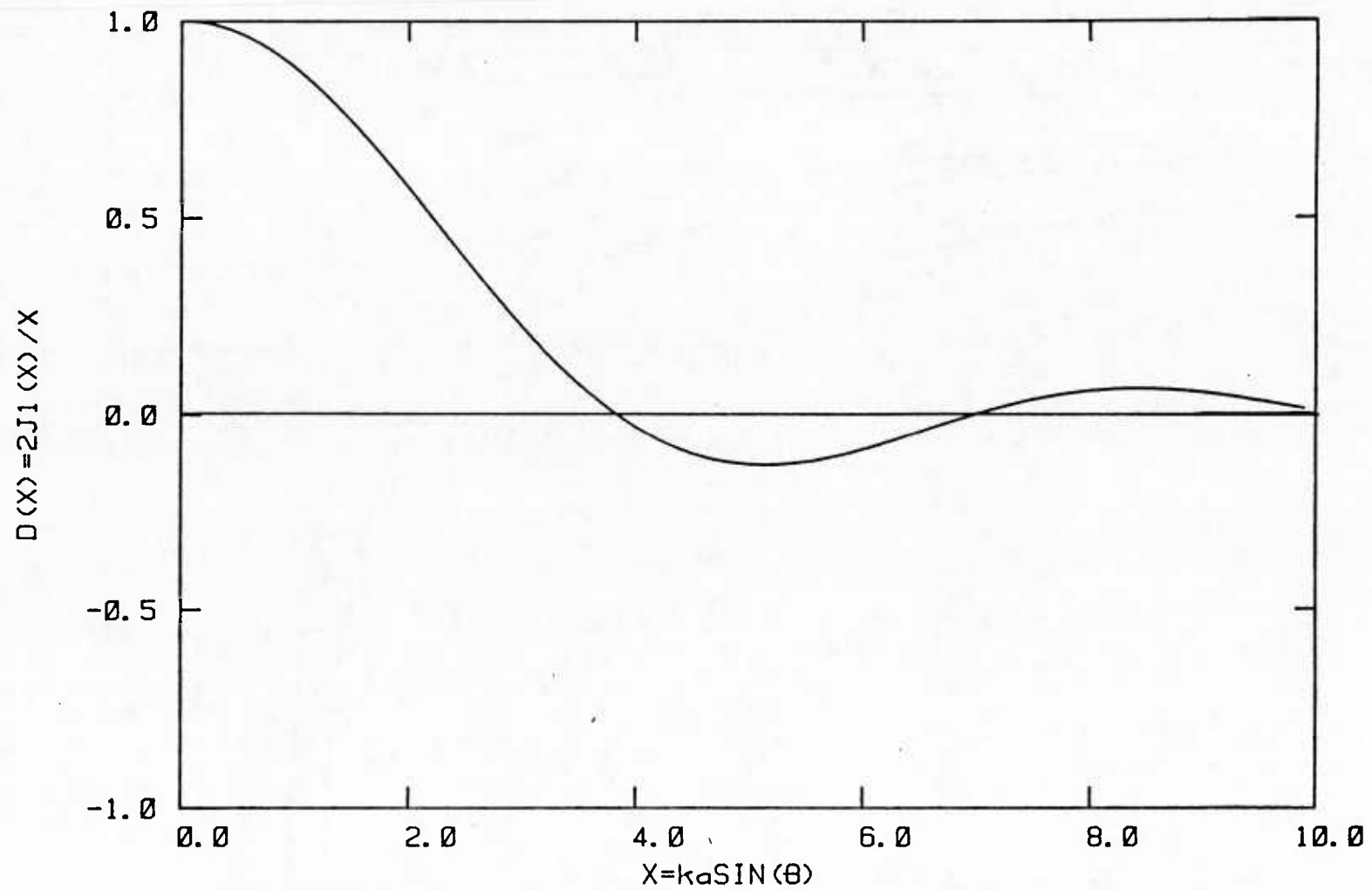


FIGURE 4.14 Directivity Pattern for Rigid Circular Piston.

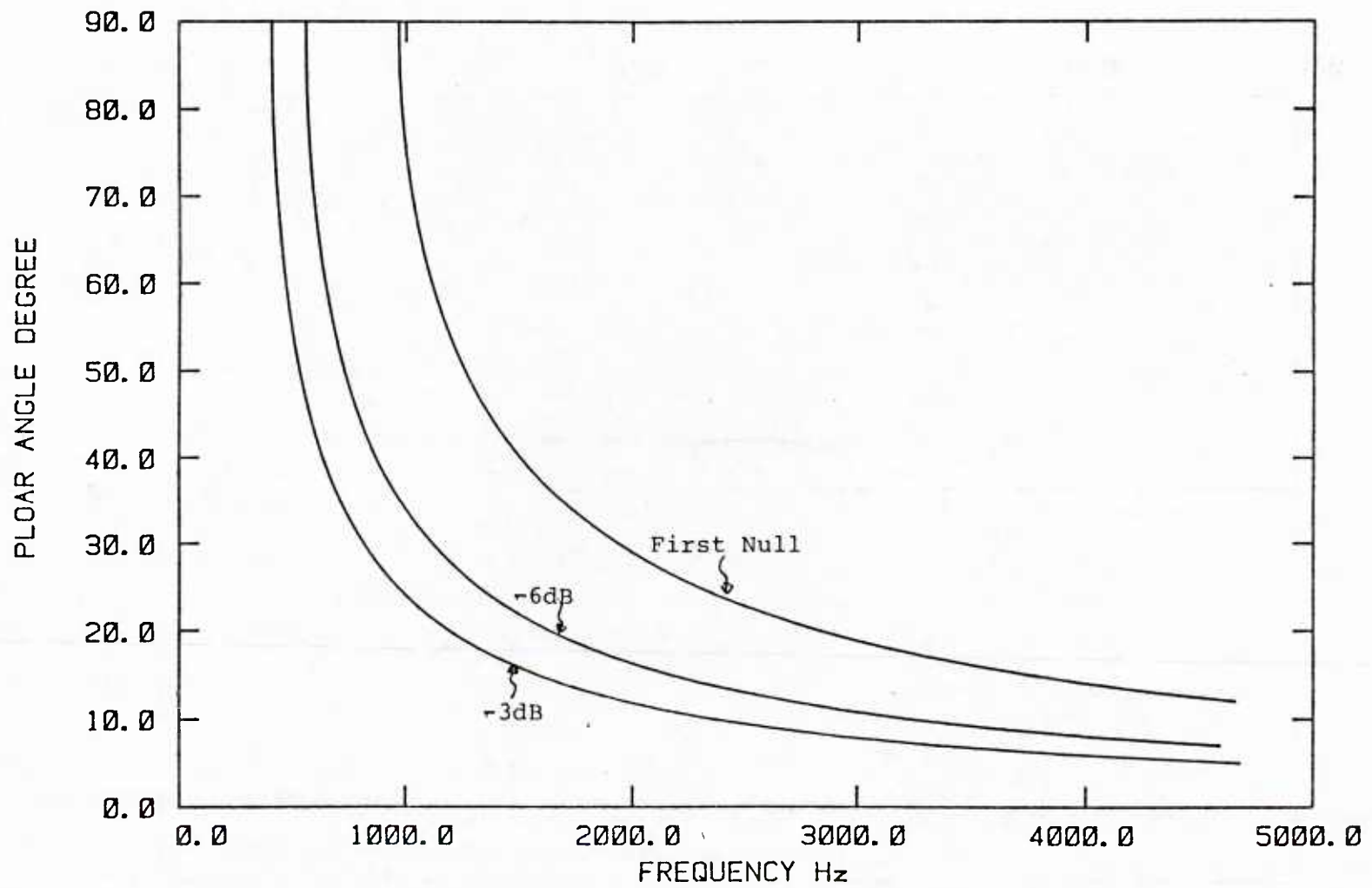


FIGURE 4.15 Directivity Beam Width @ -3dB, -6dB, and First Null.

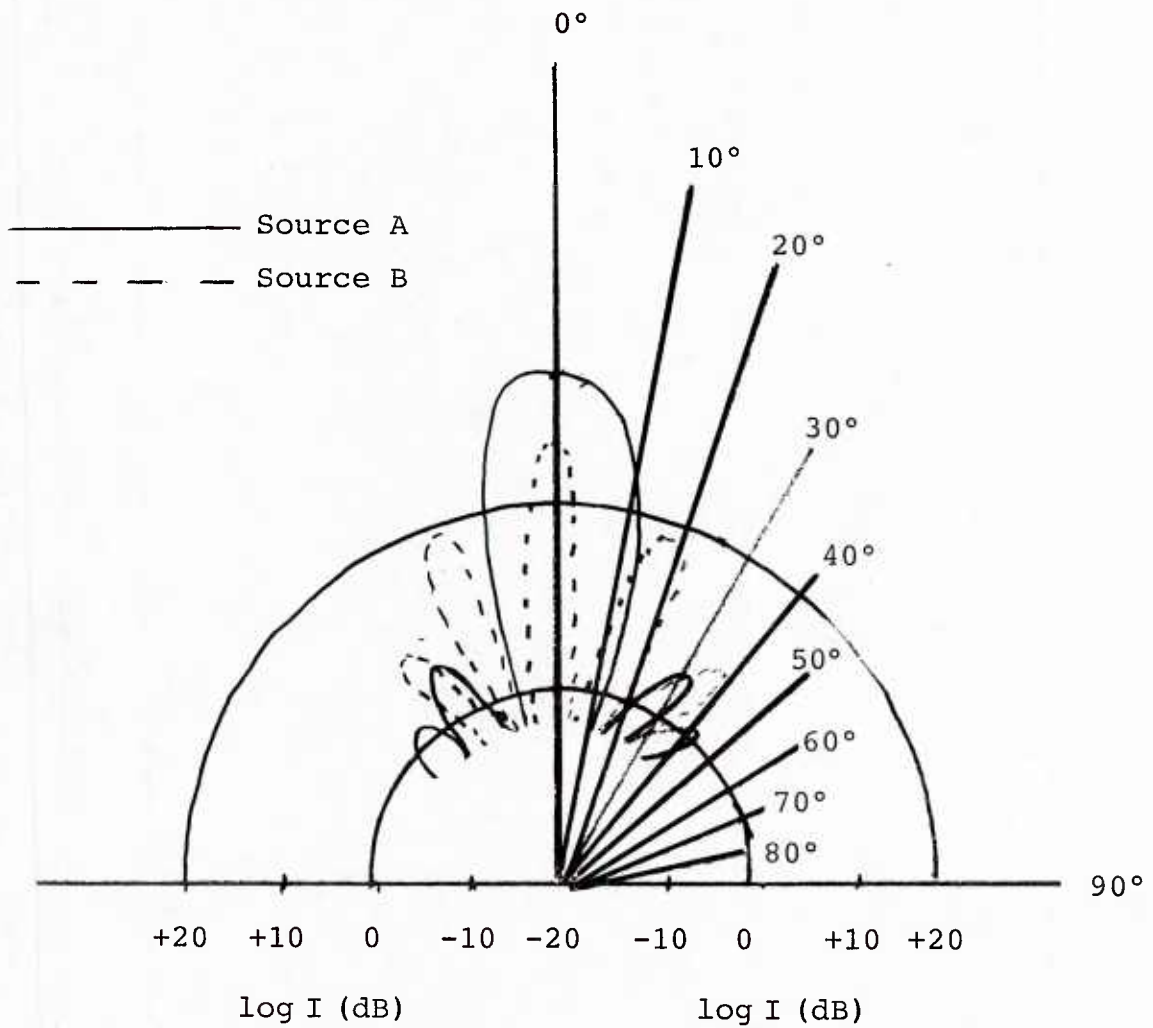


Figure 4.16. Polar Radiation Patterns of two Hypothetical Sources ($\log I$ is plotted against θ).

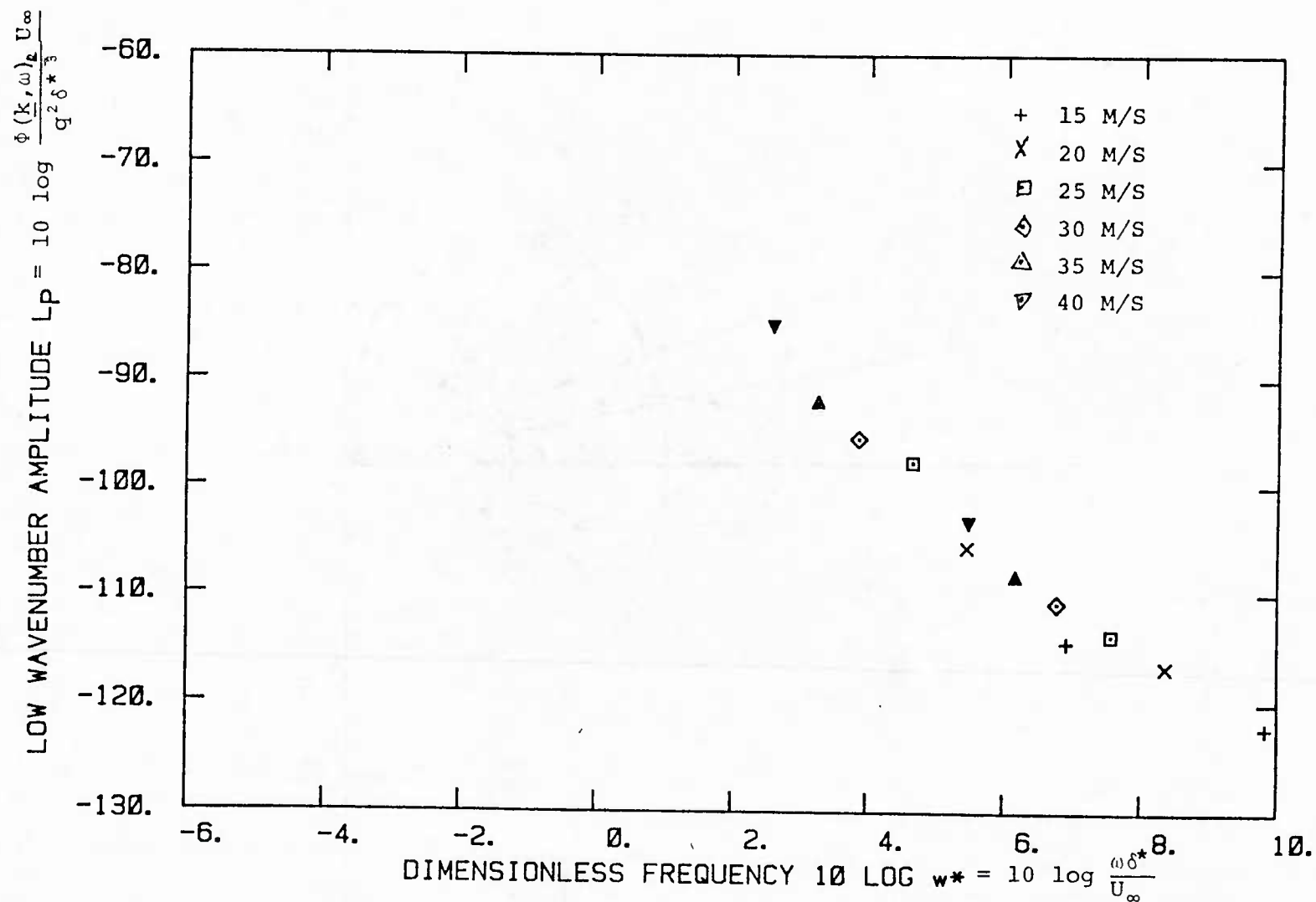


FIGURE 5.1 Low Wavenumber Results for Alternating Phase Uniform Shaded Array at Position 1.

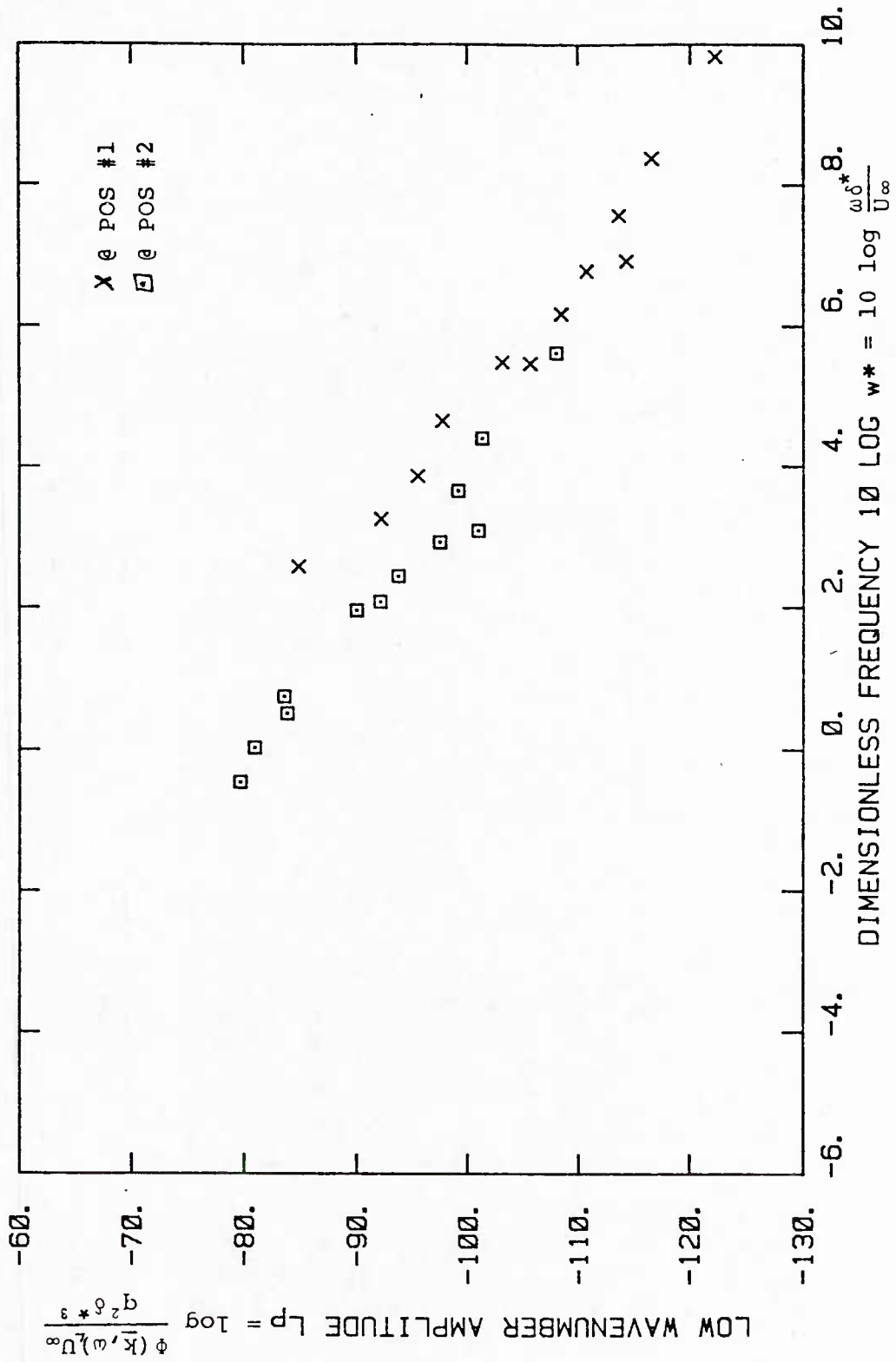


FIGURE 5.2 Comparison of Low Wavenumber Results for Alternating Phased Uniform Shaded Array at Two Positions.

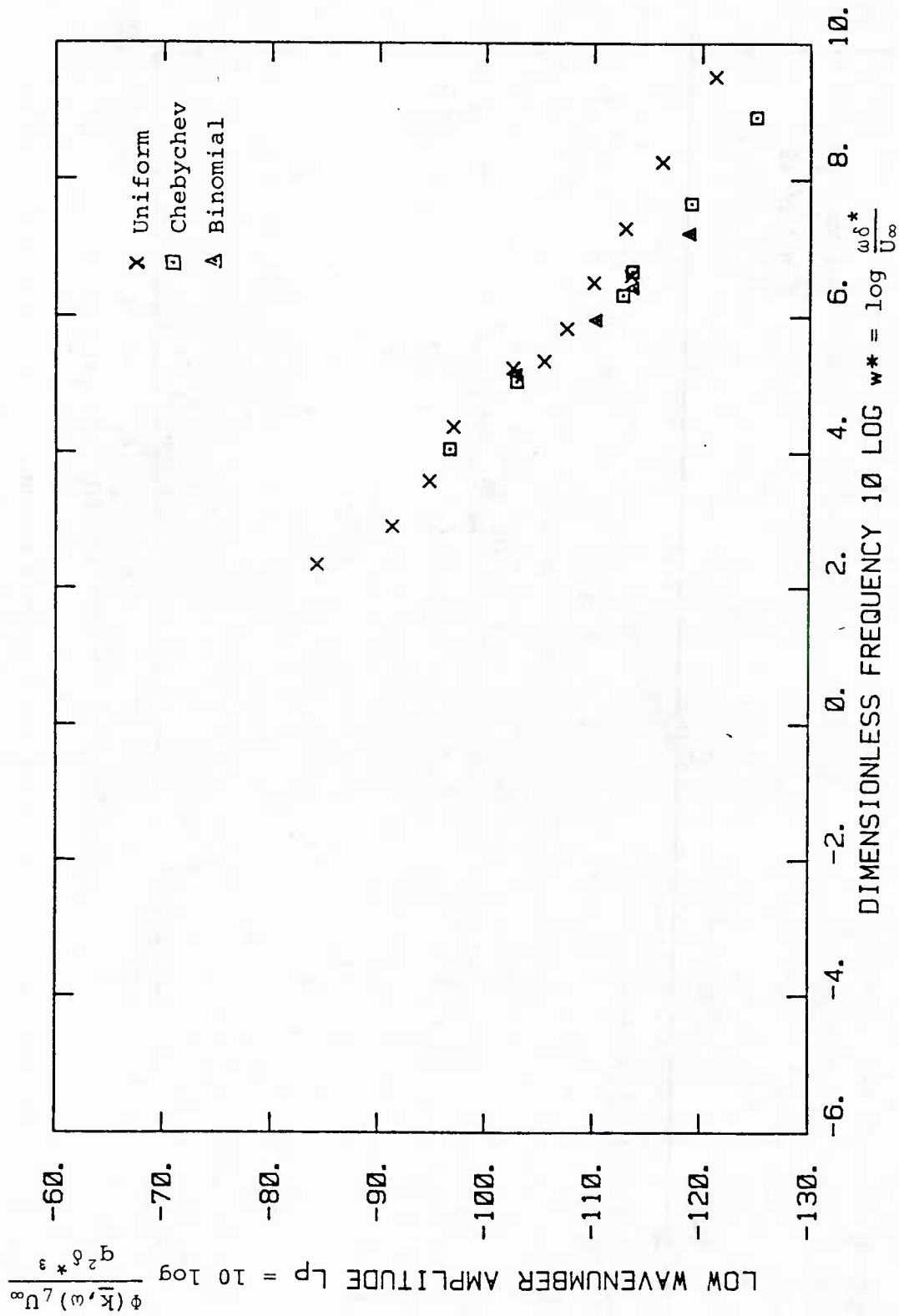


FIGURE 5.3 Comparison of Low Wavenumber Results for Uniform, Chebyshev, Binomial Shading of Alternating Phase Array.

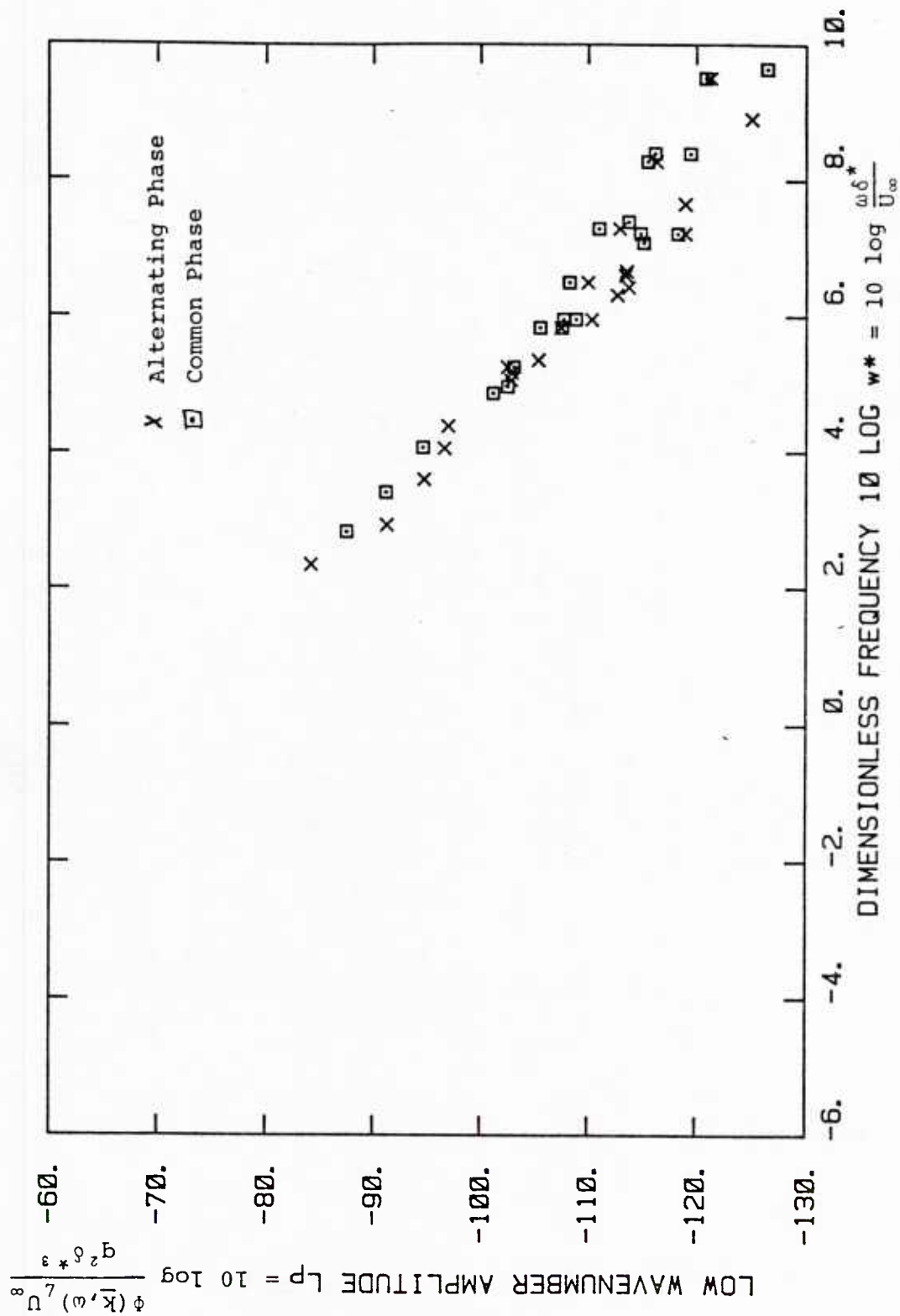


FIGURE 5.4 Comparison of Low Wavenumber Results for Alternating and Common Phased Array (all shadings).

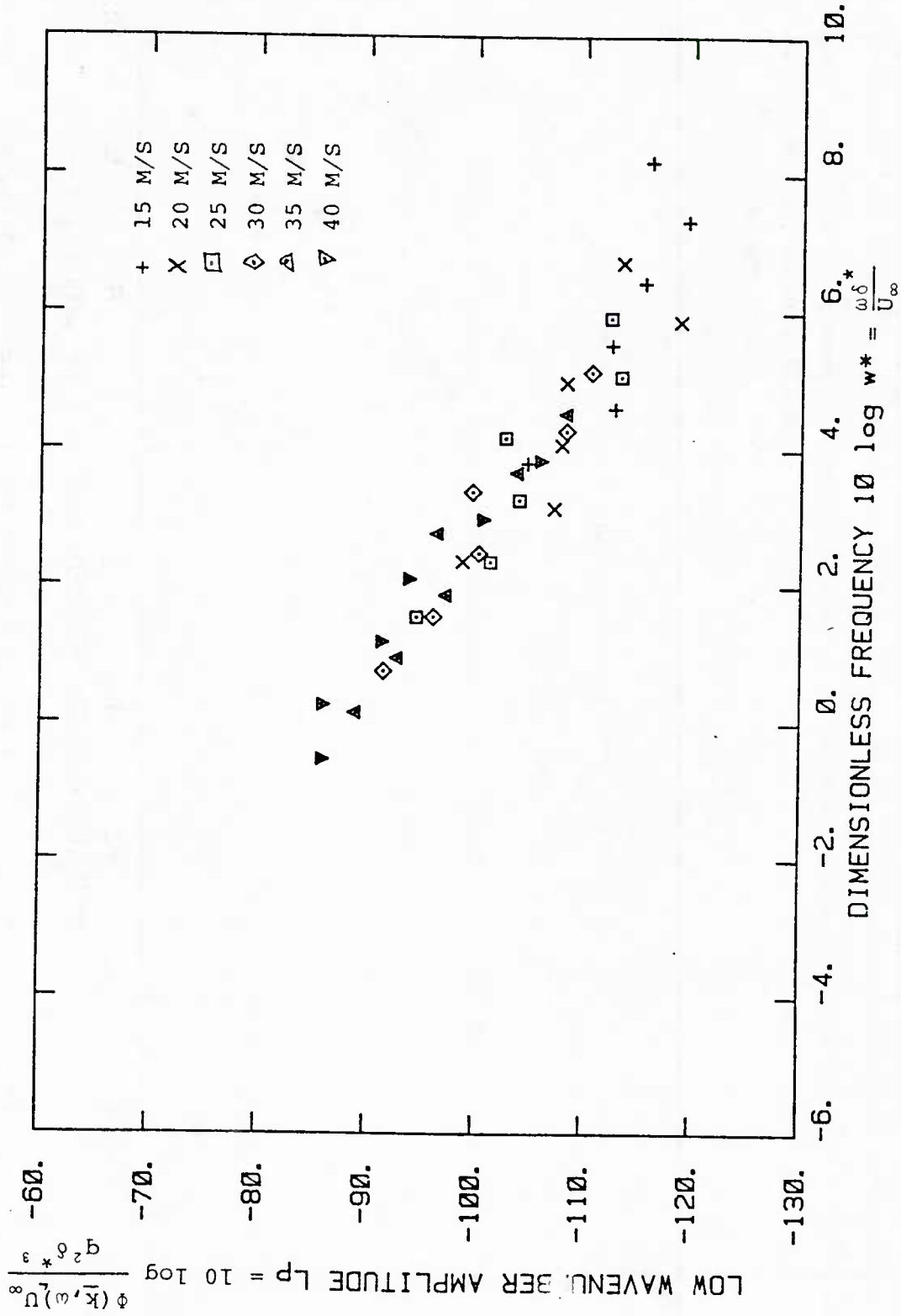


FIGURE 5.5 Low Wavenumber Results for Martin Plate @ Position #1.

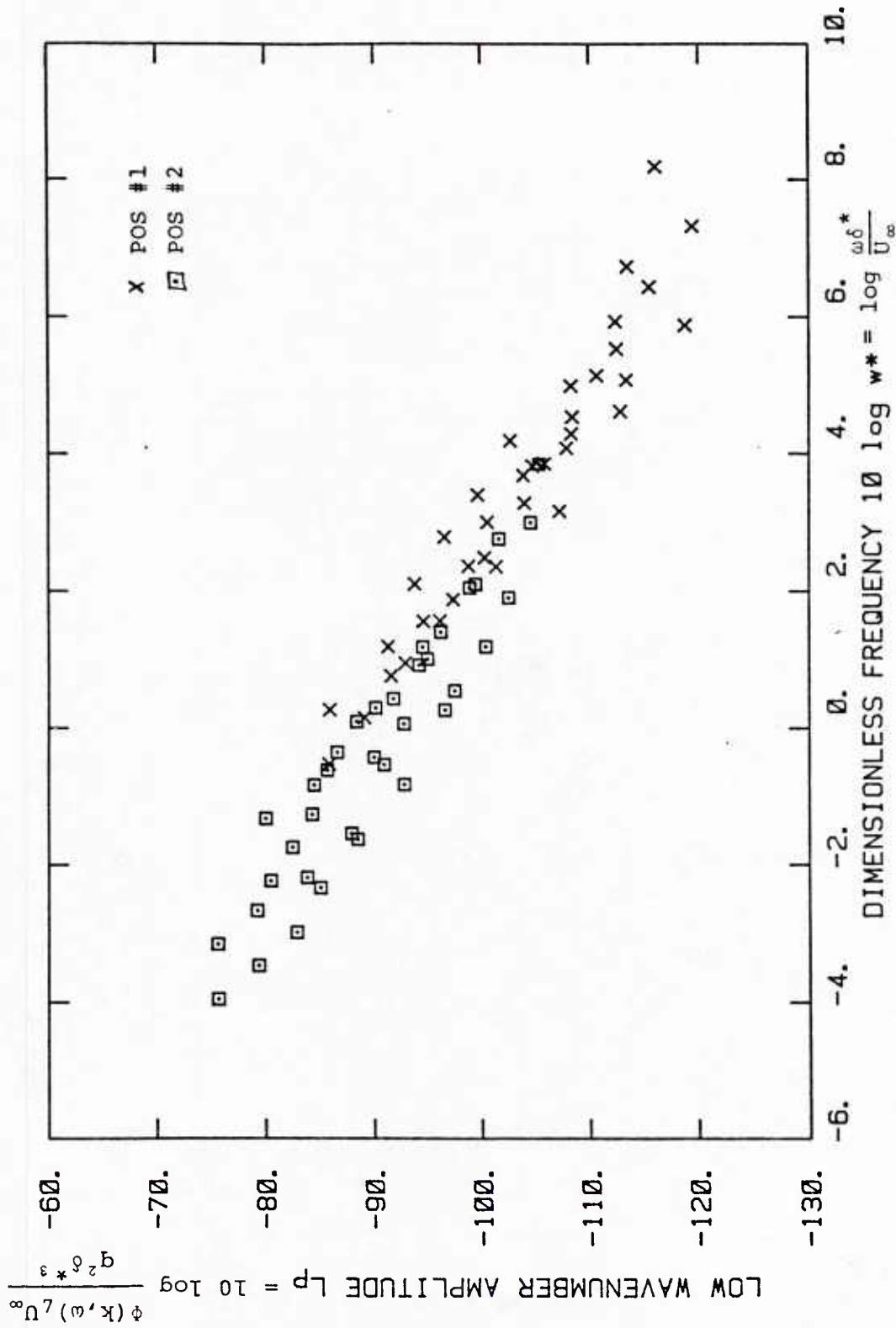


FIGURE 5.6 Comparison of Low Wavenumber Results for Martin Plate at Two Different Locations.

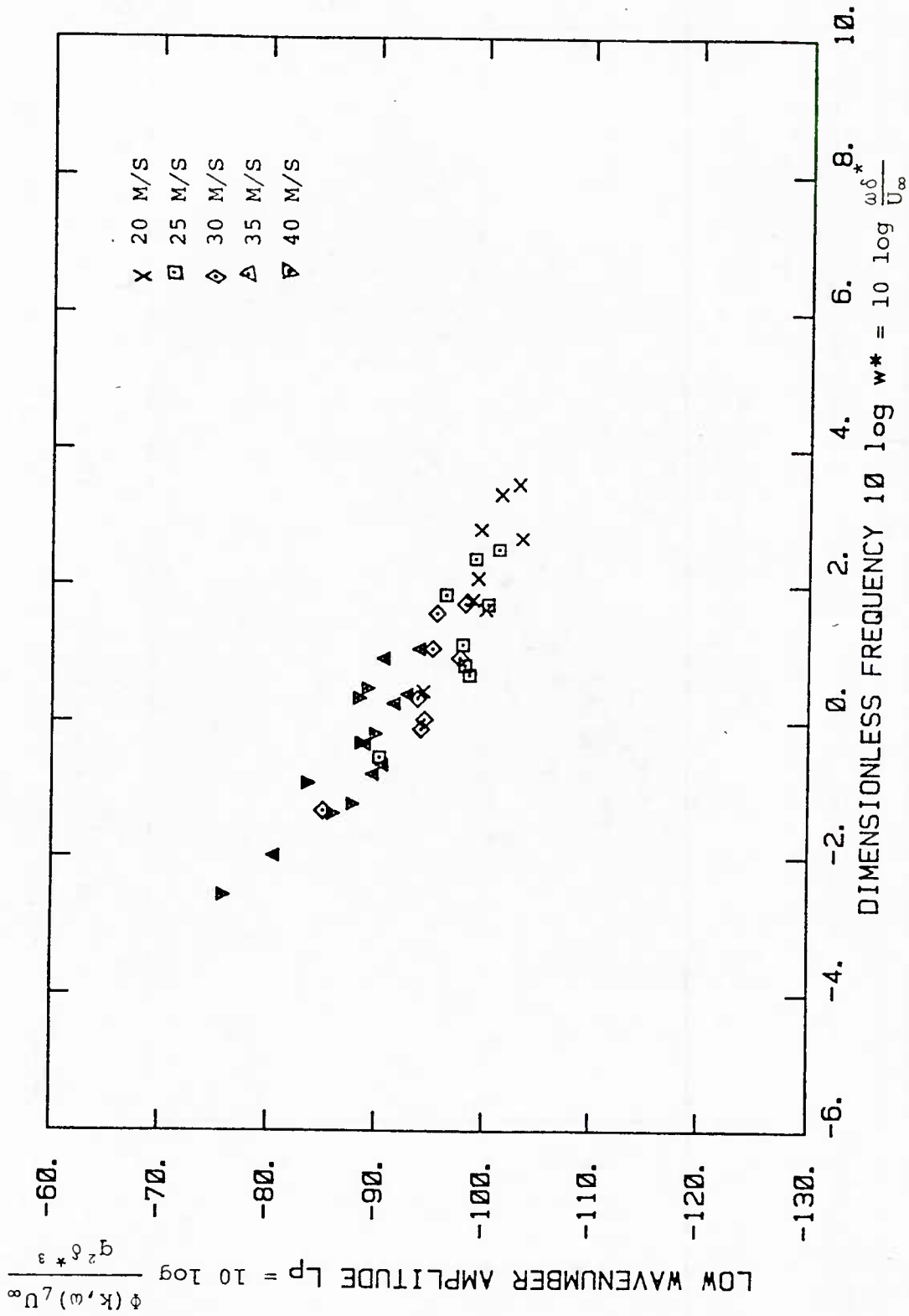


FIGURE 5.7 Low Wavenumber Results for Jameson Plate @ Position #1.

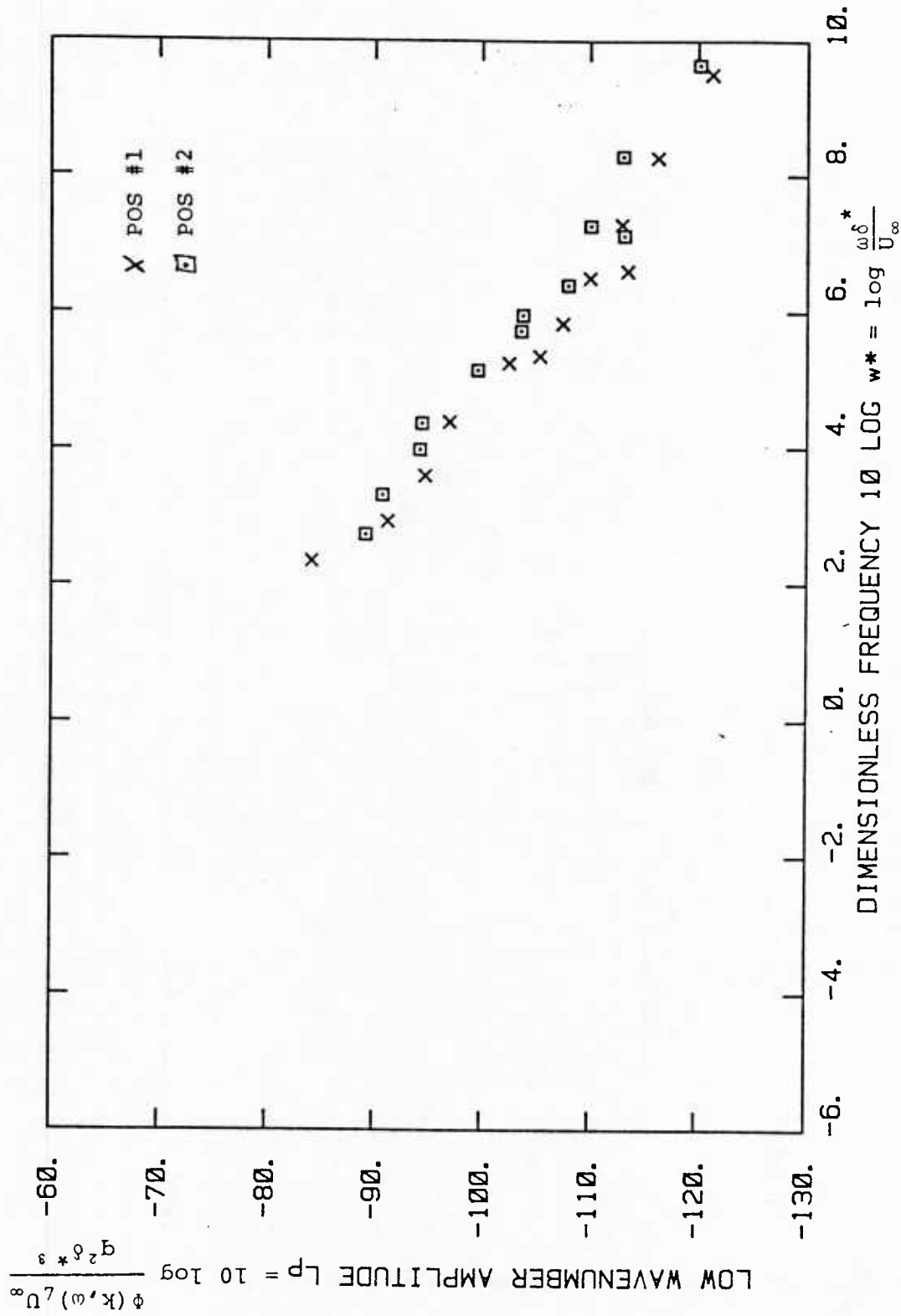


FIGURE 5.8 Comparison of Alternating Array Low Wavenumber Results
 @ Two Position for $\delta^* = \text{constant} = 0.2$ inches.

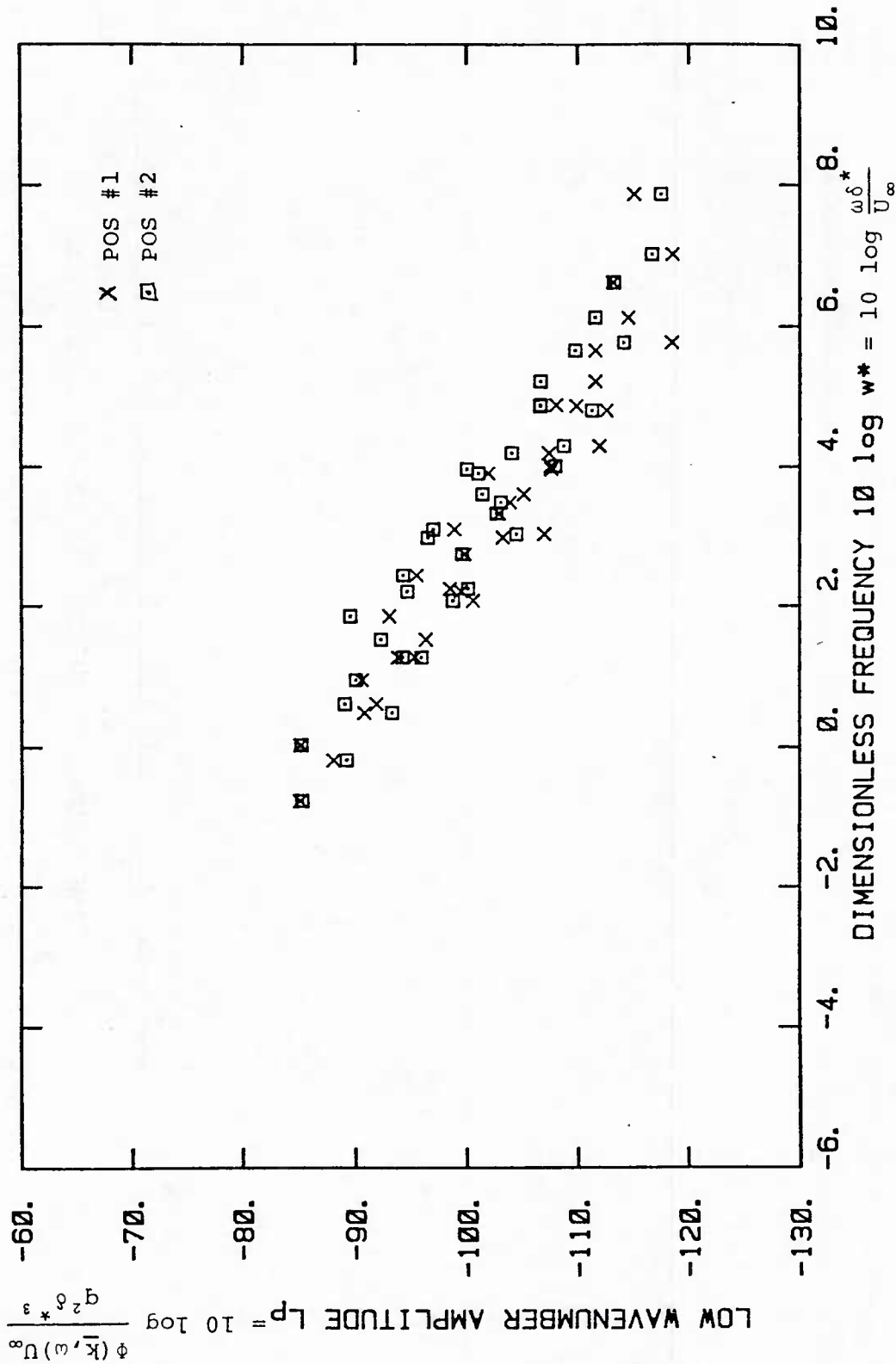


FIGURE 5.9 Comparison of Martin Plate Low Wavenumber Results at Two Position With $\delta^* = \text{constant} = 0.2$ Inches.

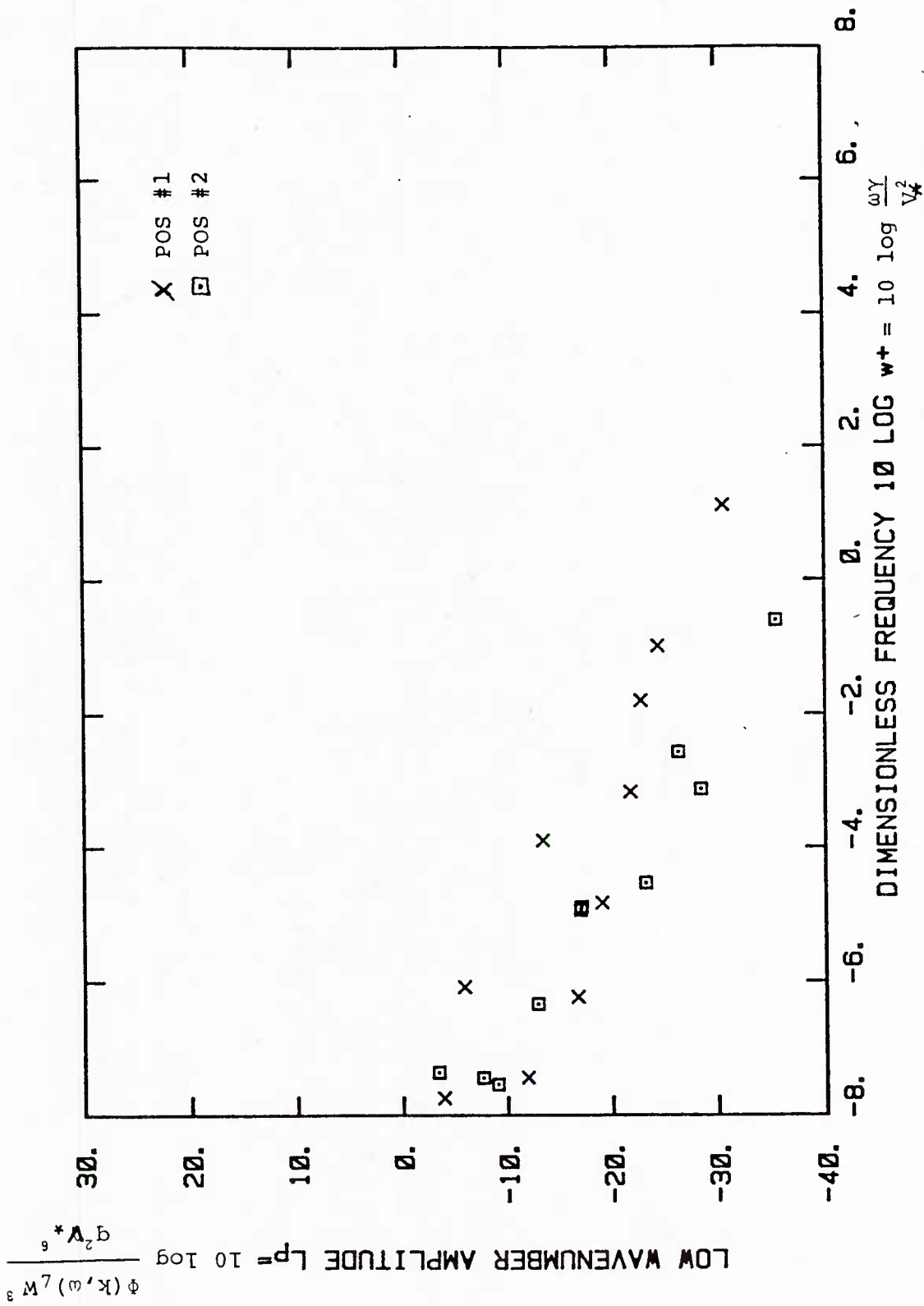


FIGURE 5.10 Alternating Phased Array Low Wavenumber Results at Two Location Non-Dimensionalized on Inner Variables

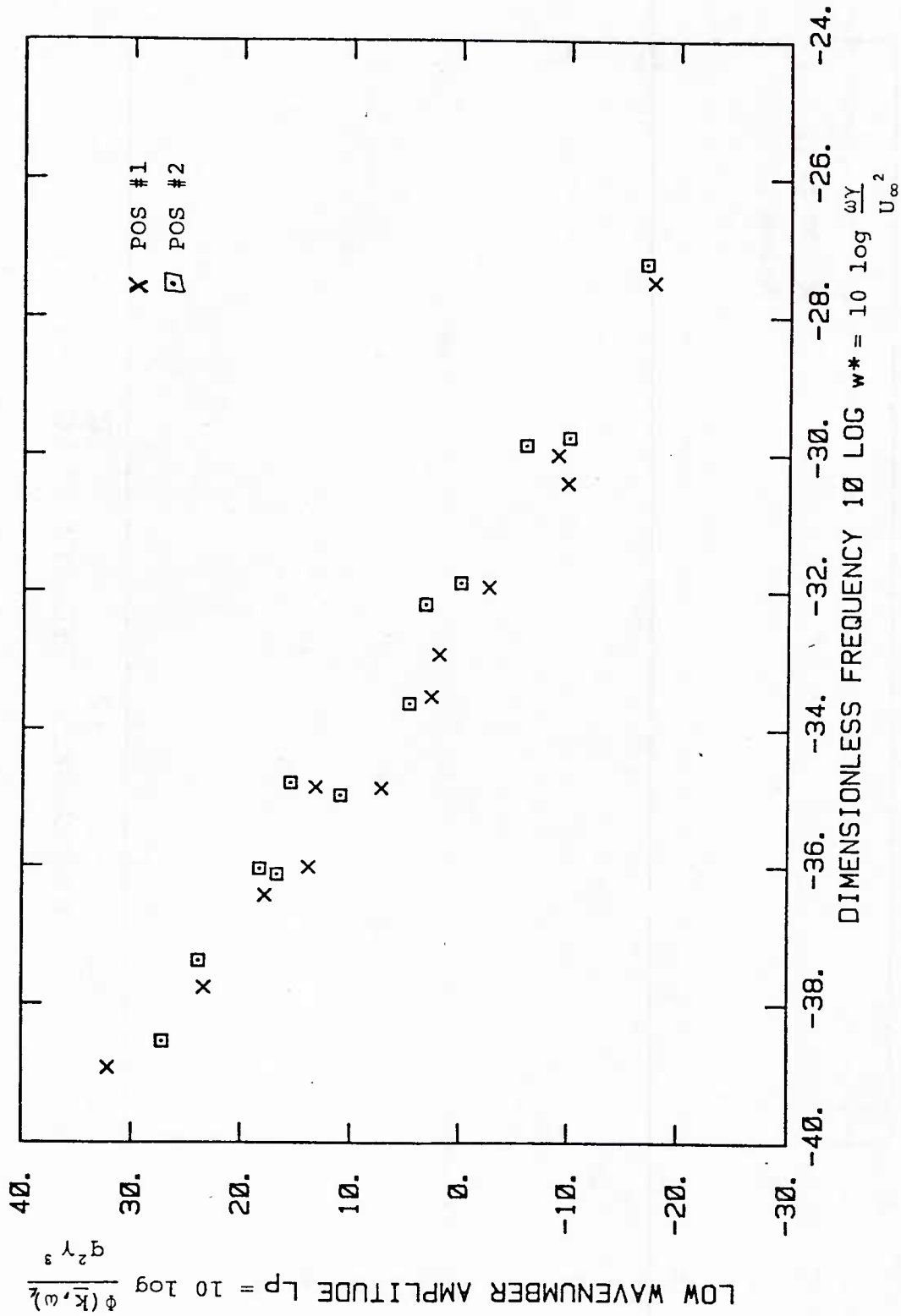


FIGURE 5.11 Alternating Phase Array Low Wavenumber Results at Two Locations Non-Dimensionalized on Flow Variables

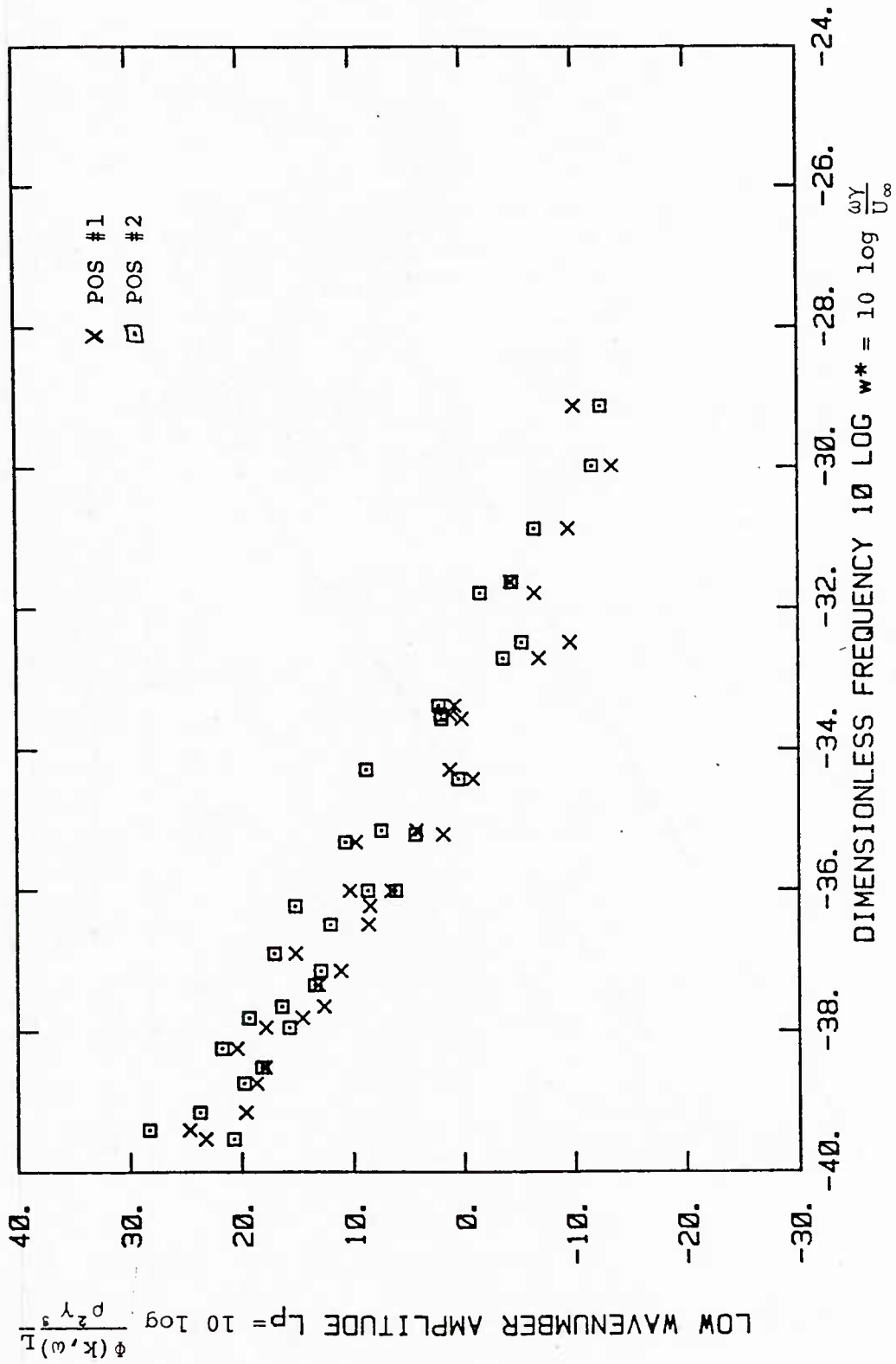


FIGURE 5.12 Martin Plate Low Wavenumber Results at Two Locations Non-Dimensionalized on Flow Variables.

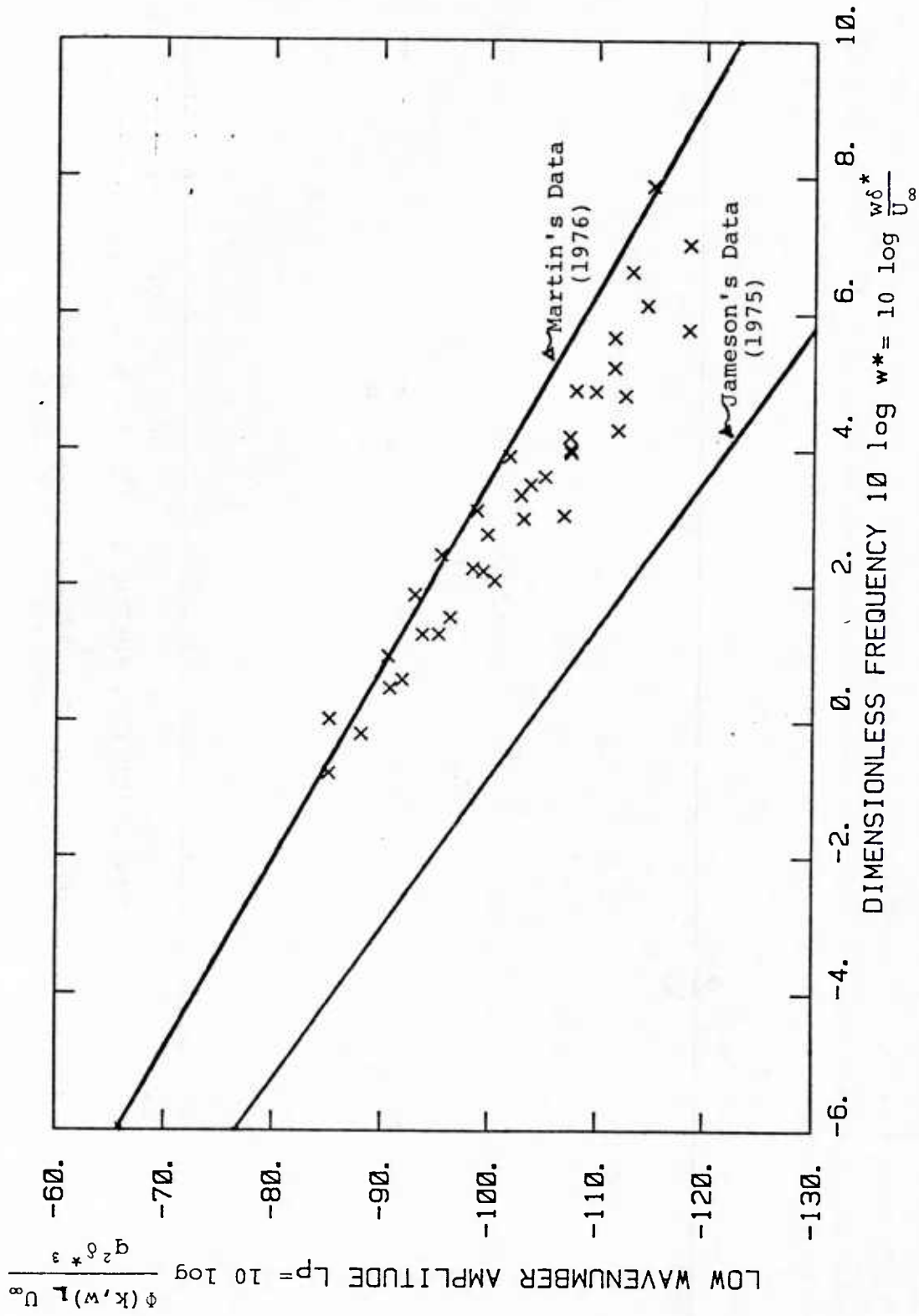


FIGURE 5.13 Martin Plate Low Wavenumber Results Compared to Earlier Investigators.

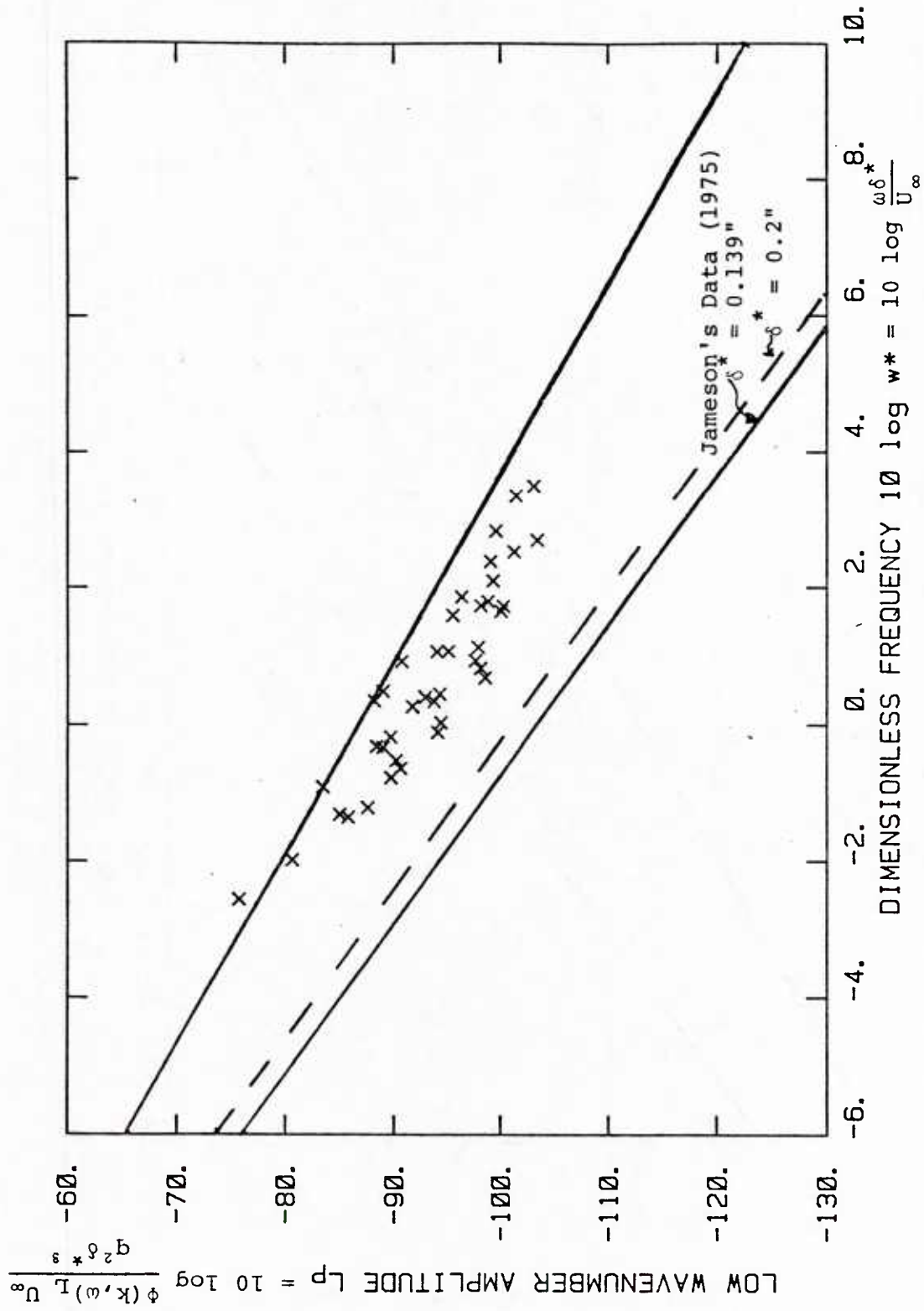


FIGURE 5.14 Jameson Plate Low Wavenumber Results Compared With Earlier Investigators.

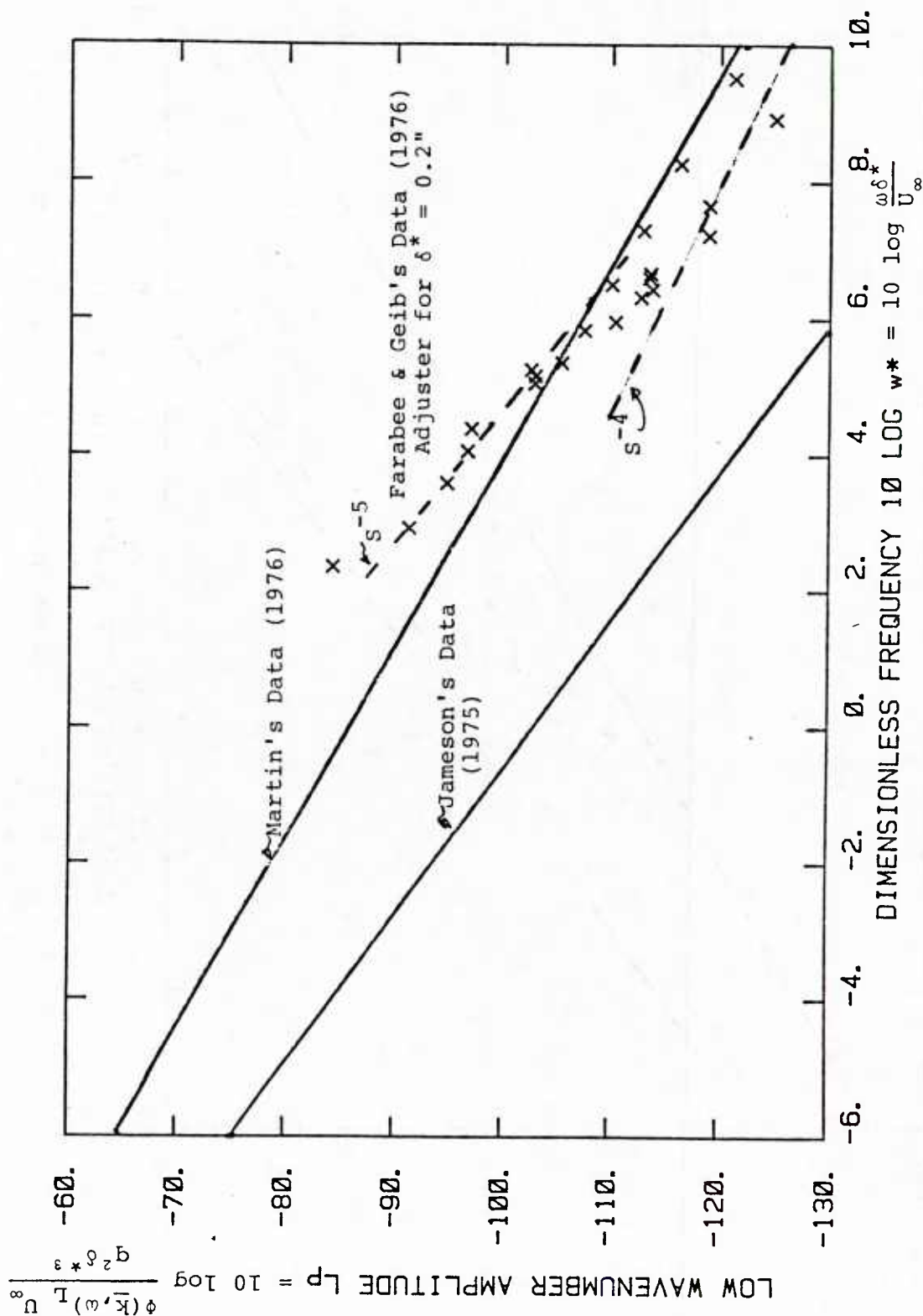


FIGURE 5.15 Microphone Array Low Wavenumber Results Compared to Earlier Investigators.

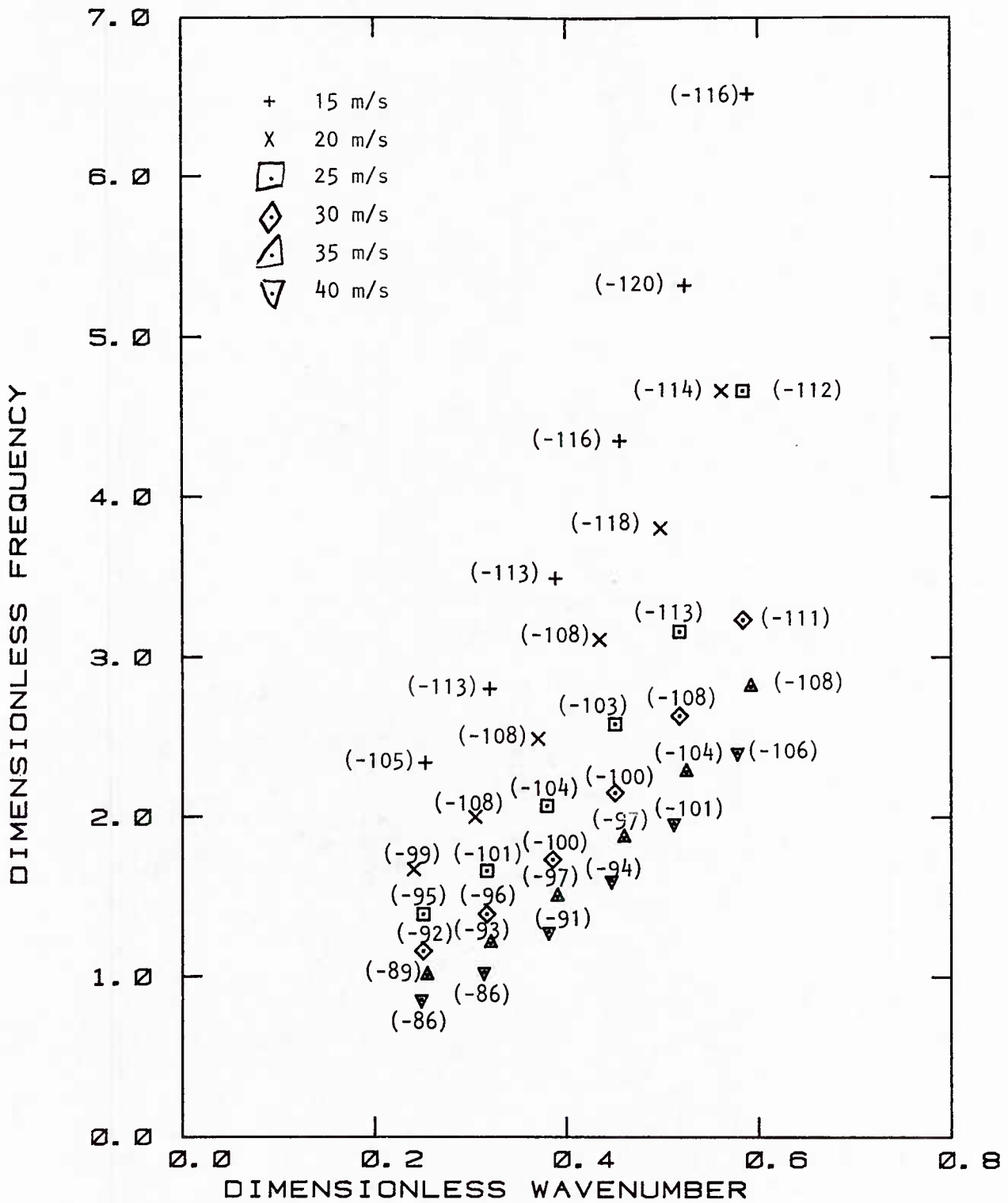


Figure 5.16. Low Wavenumber Result of Martin Plate in ω - k Plane

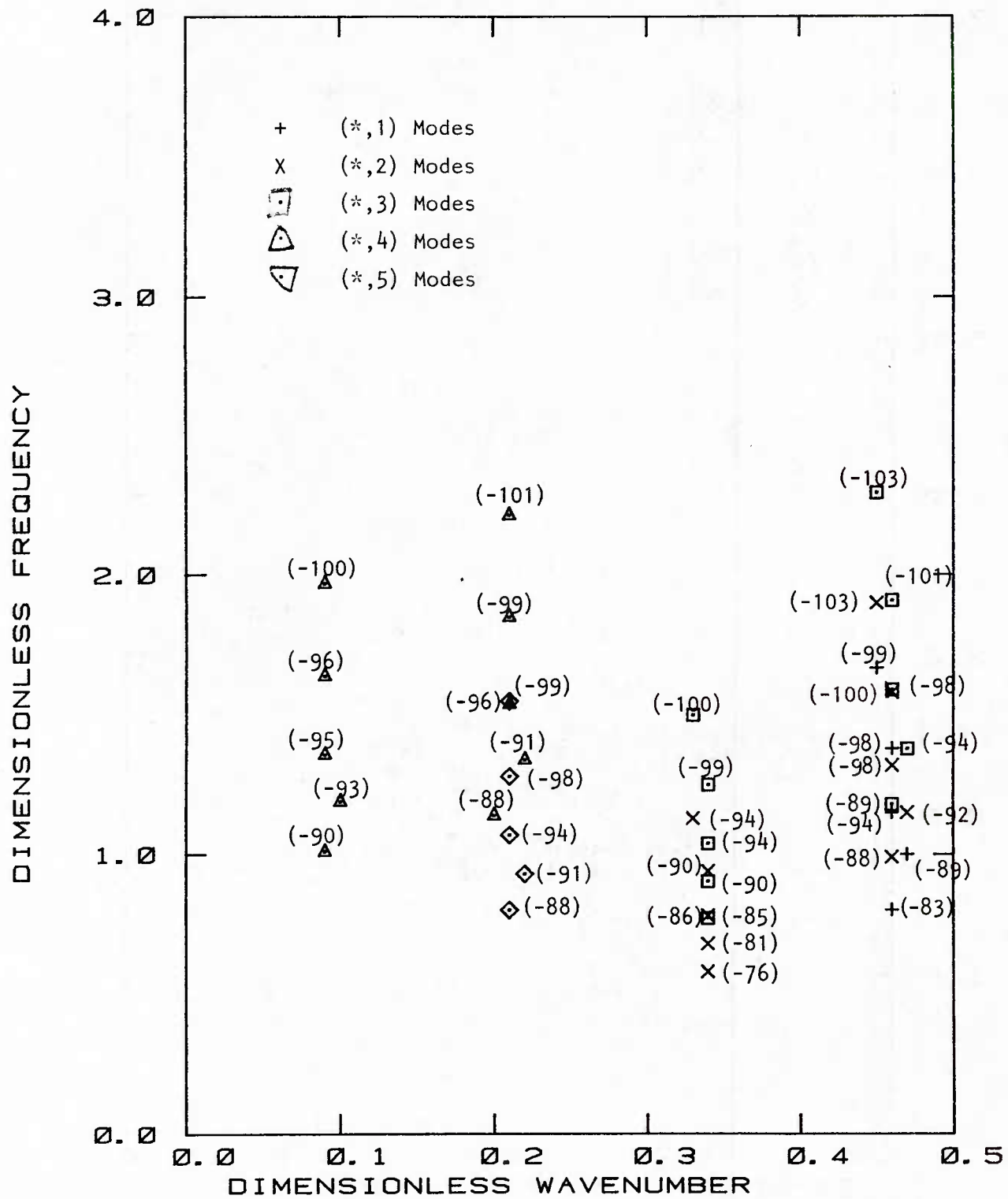


Figure 5.17. Low Wavenumber Results of Jameson Plate in ω -K Plane.

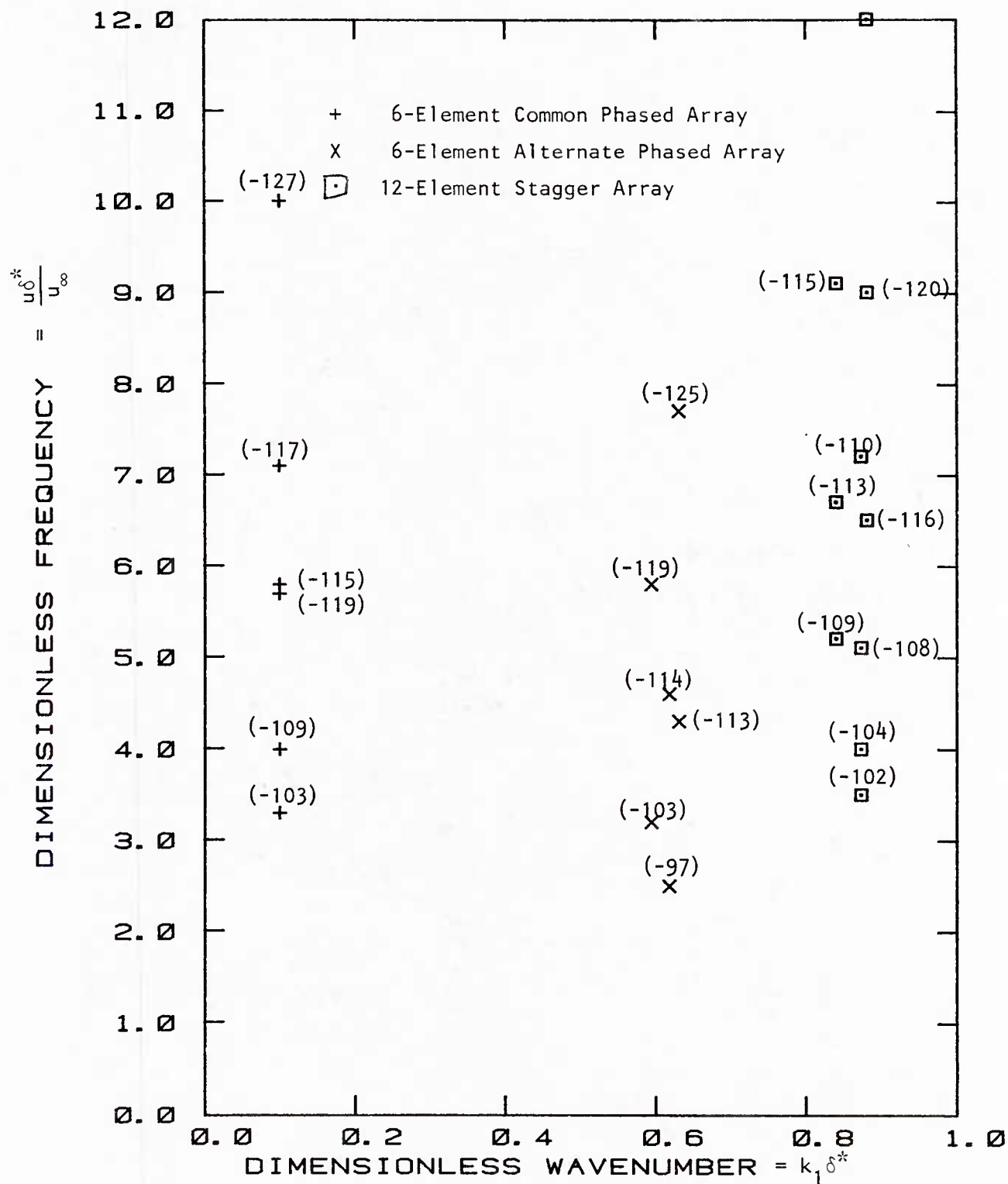


Figure 5.18. Low Wavenumber Results of Microphone Arrays in $\omega-k_1$ Plane

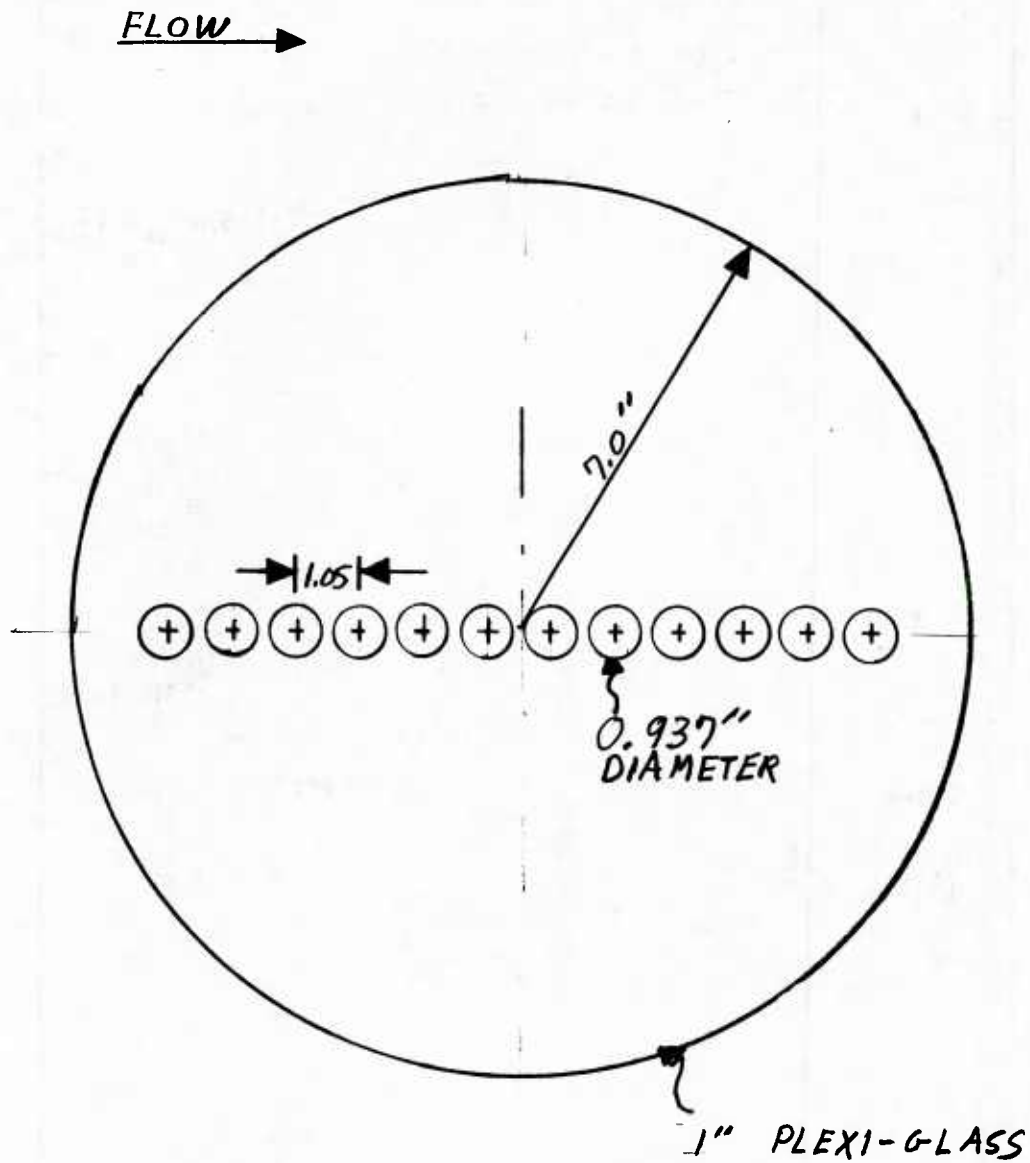


Figure A1. 12-Element Collinear Array Test Fixture

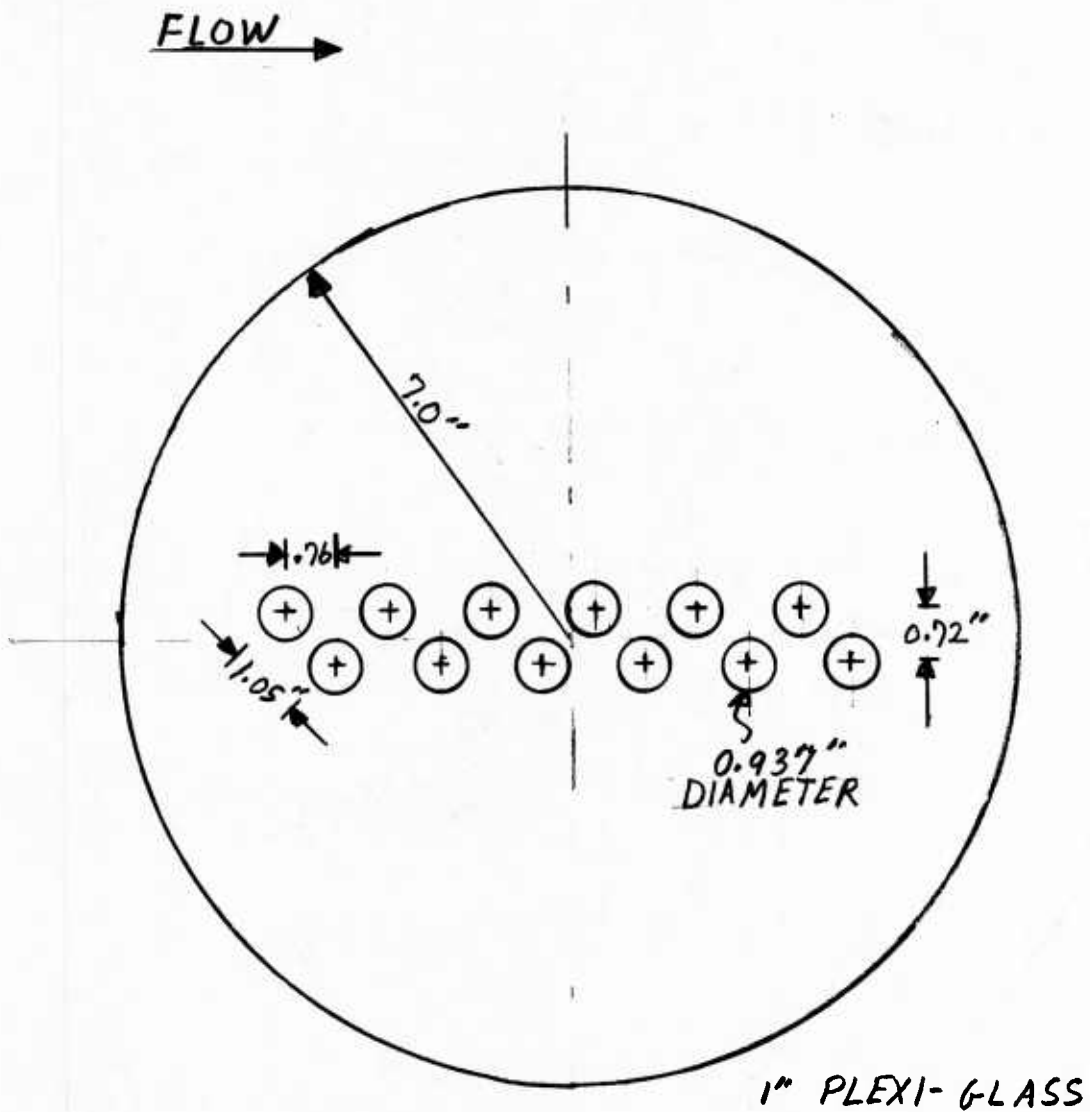


Figure A2. 12-Element Stagger Array Test
Fixture

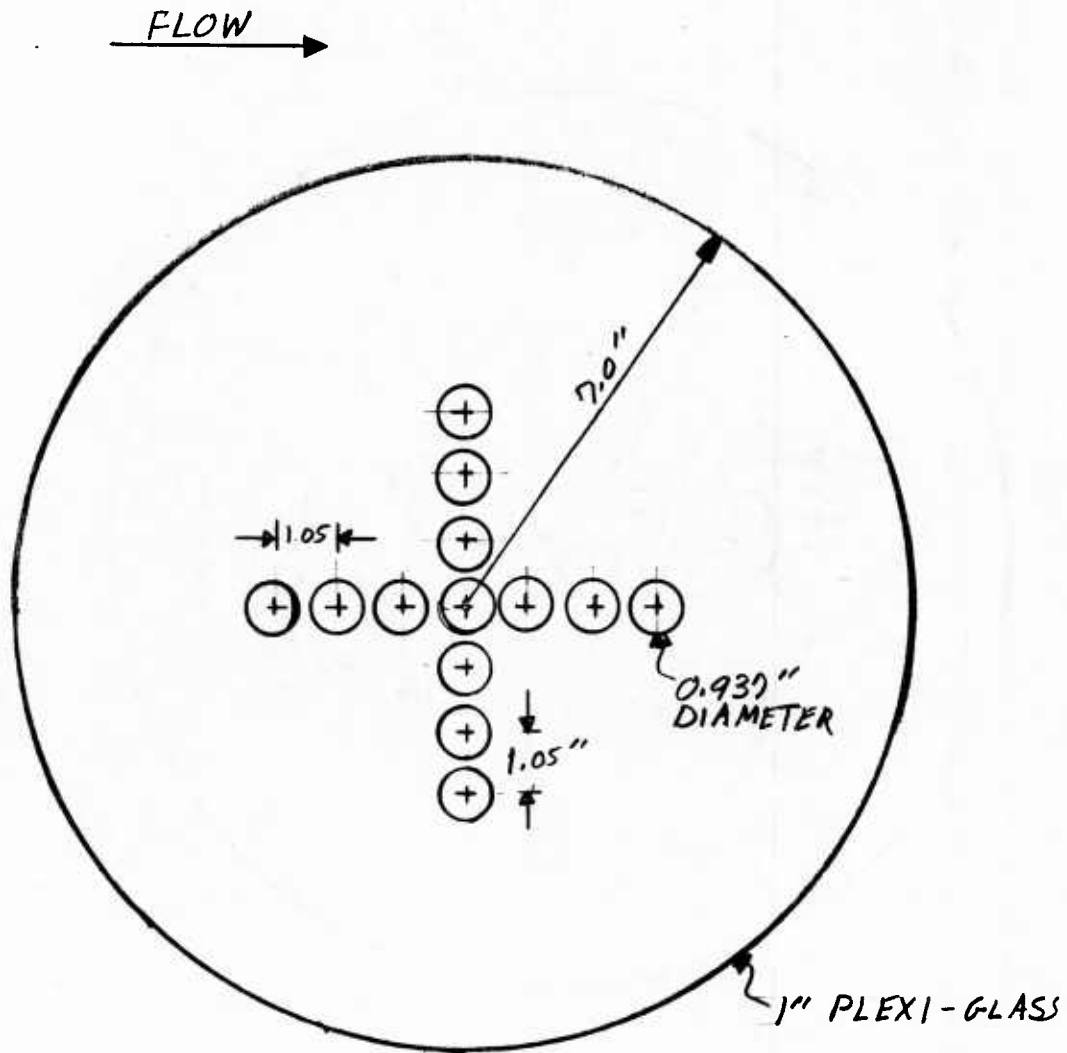


Figure A3. Cross Array Test Fixture

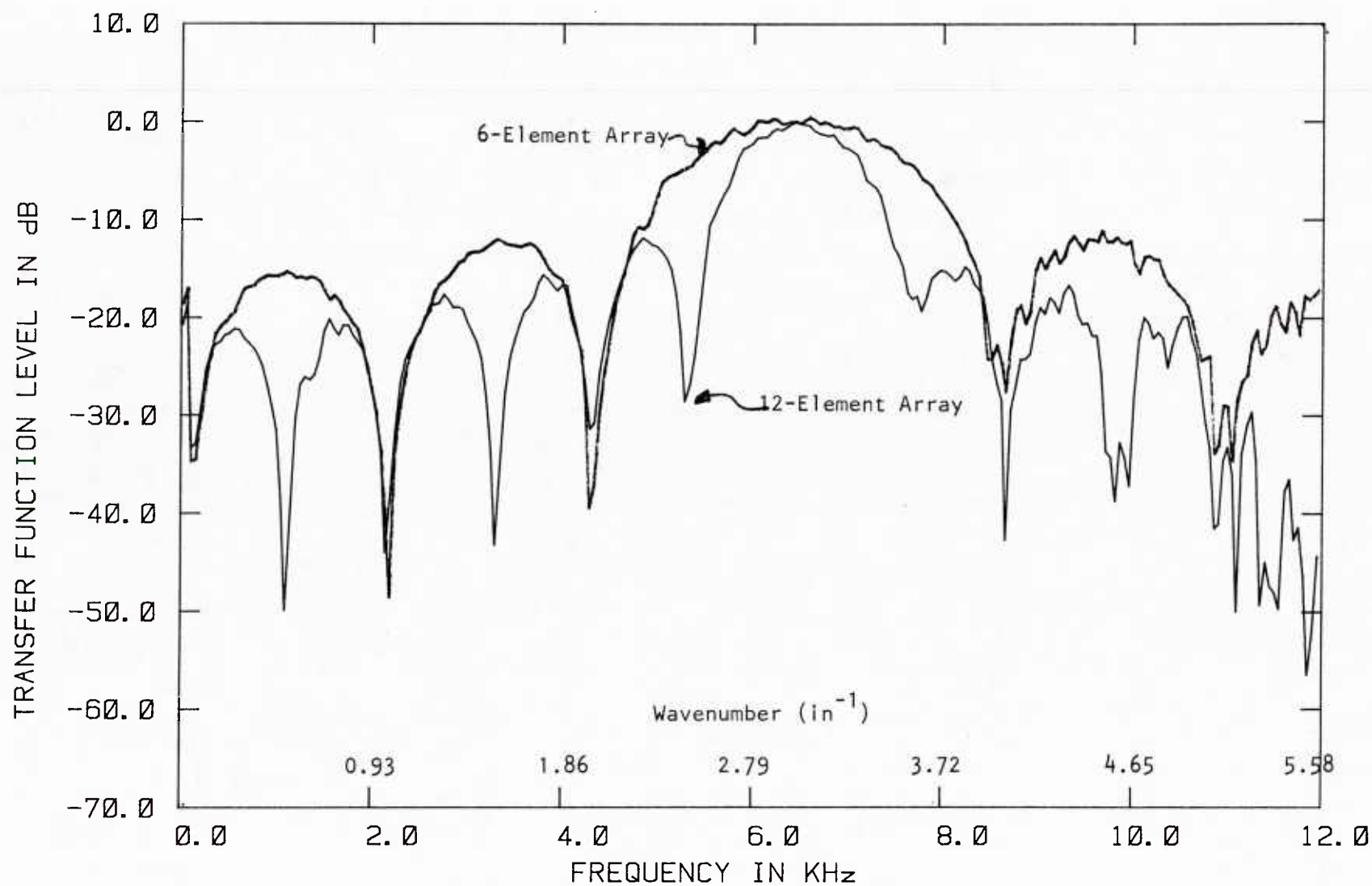


Figure A4. Comparison of 6 and 12-Element Alternating Phased Wavenumber Response

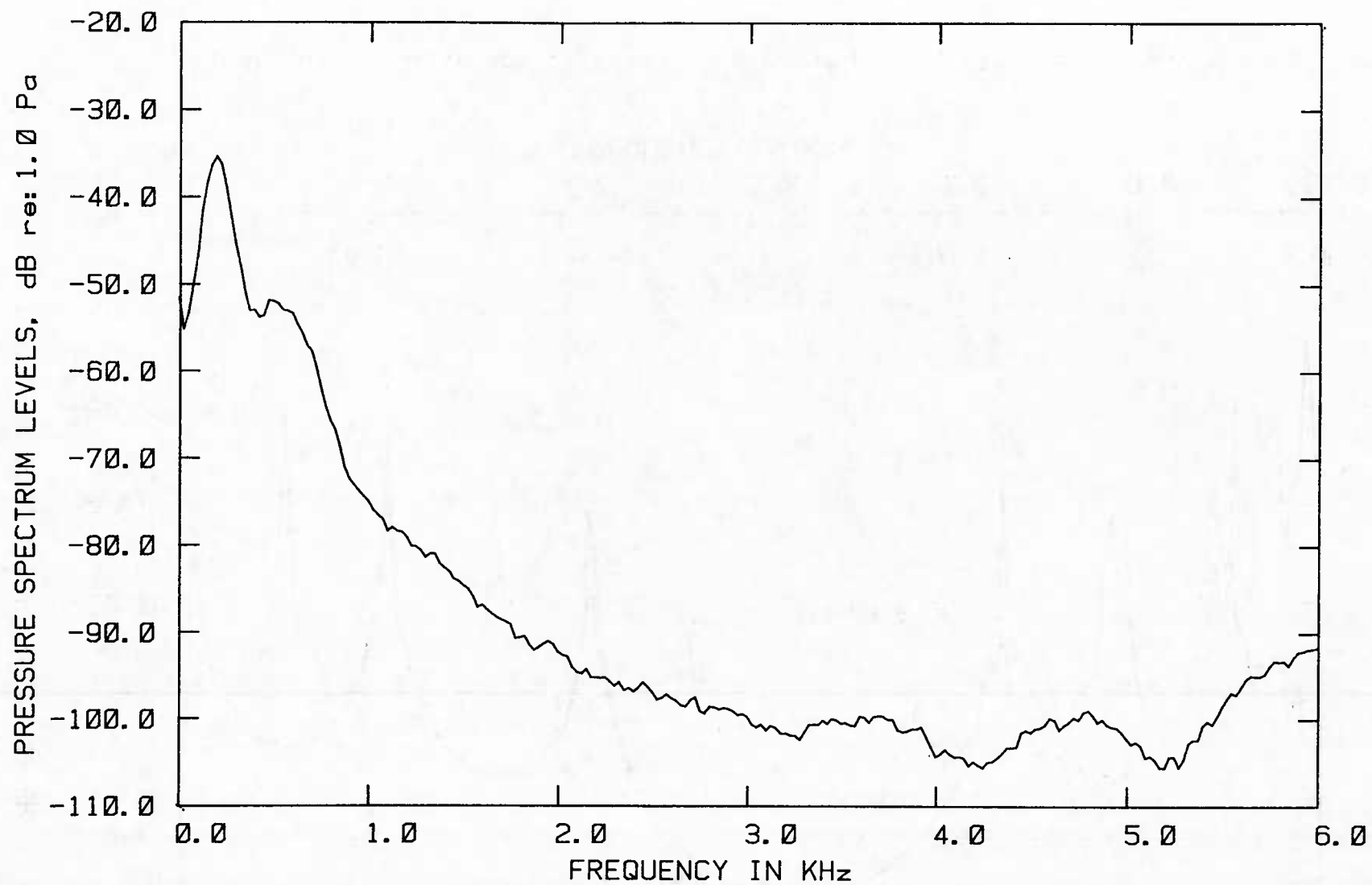


Figure A5. 12-Element Alternate Phased Array @ 15 m/s

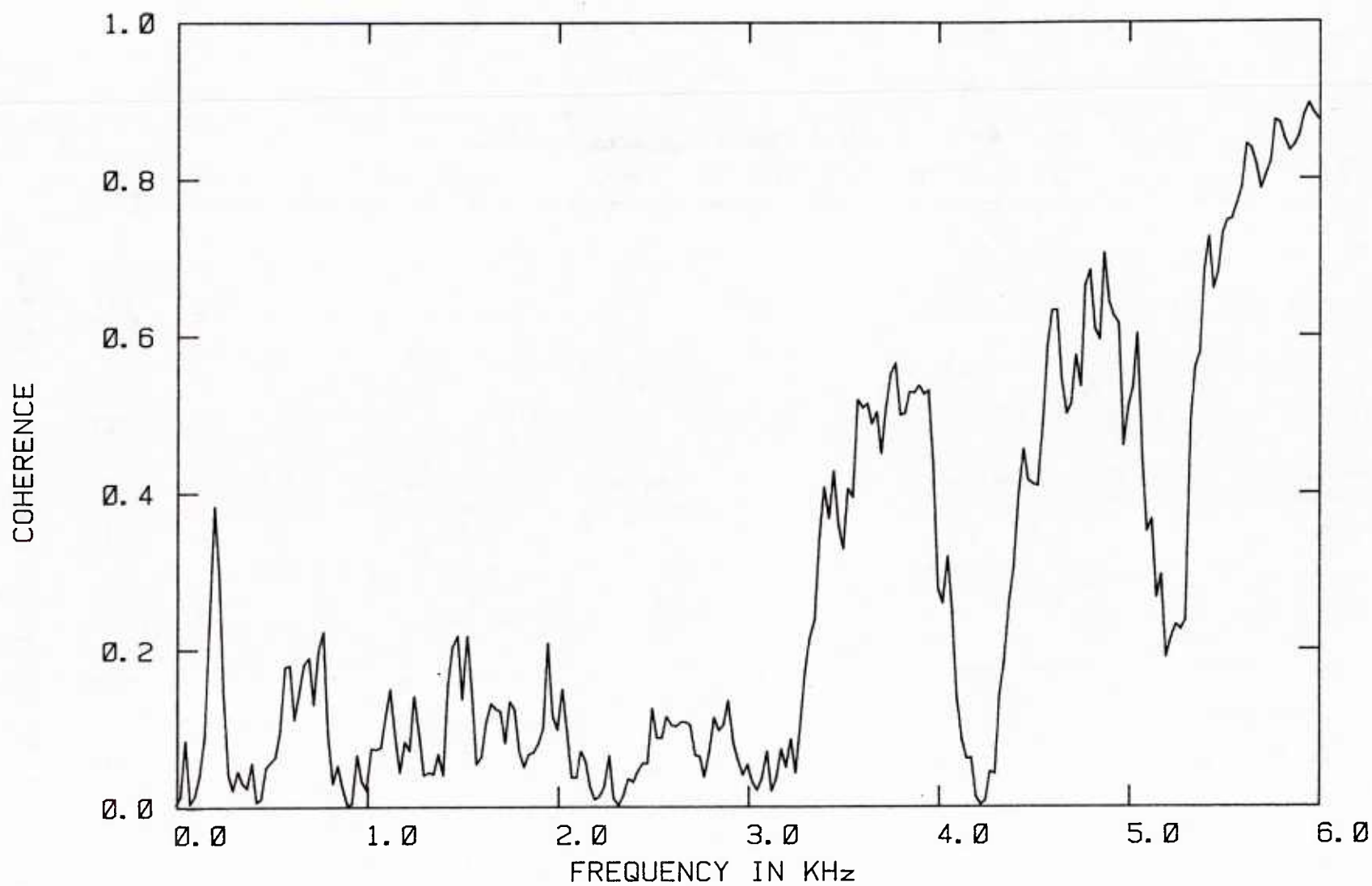


Figure A6. Coherence of 12-Element Alternate Phased Array @ 15 m/s

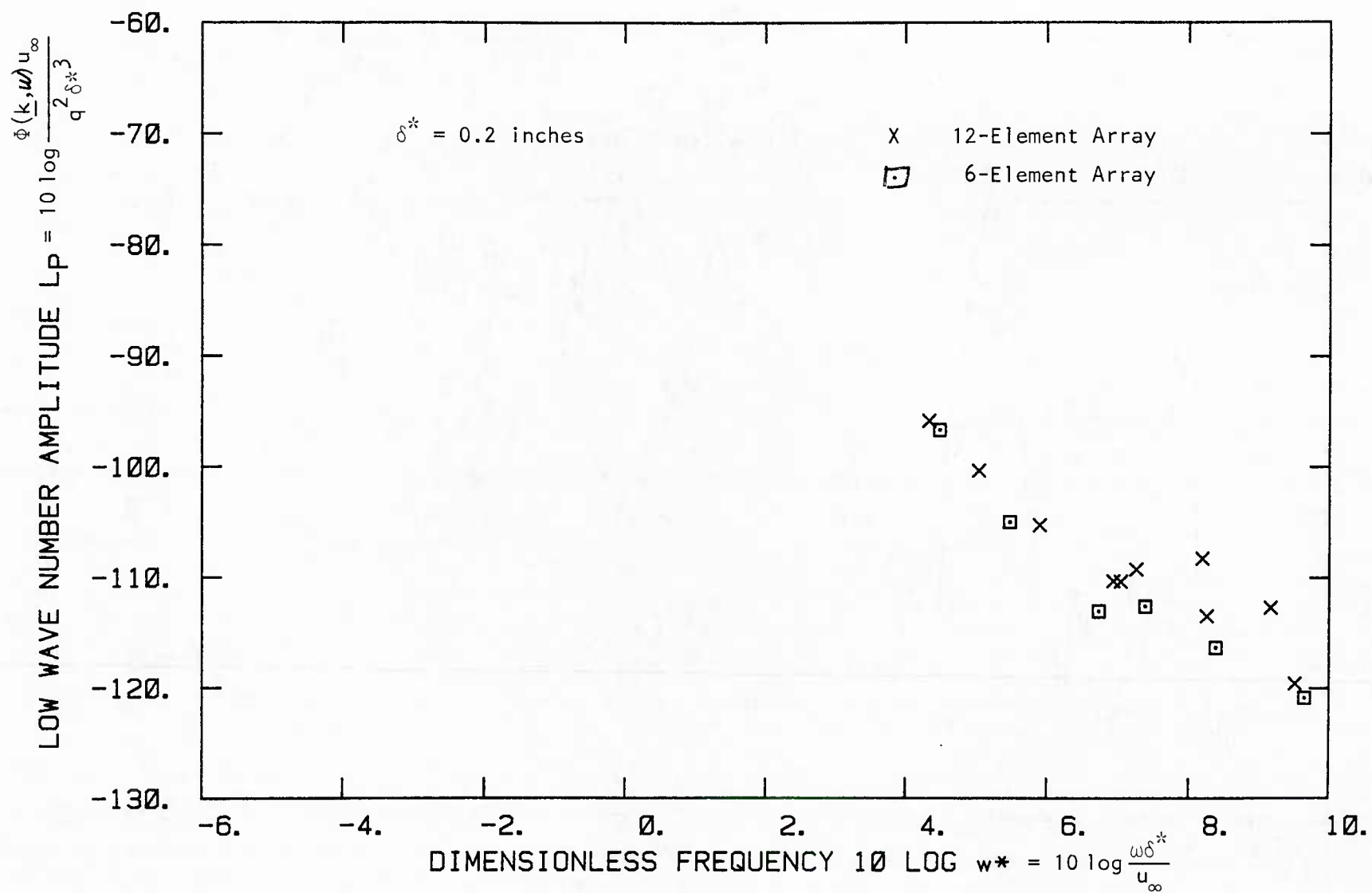


Figure A7. 12-Element Collinear Array, Uniform Shaded, Low Wavenumber Results

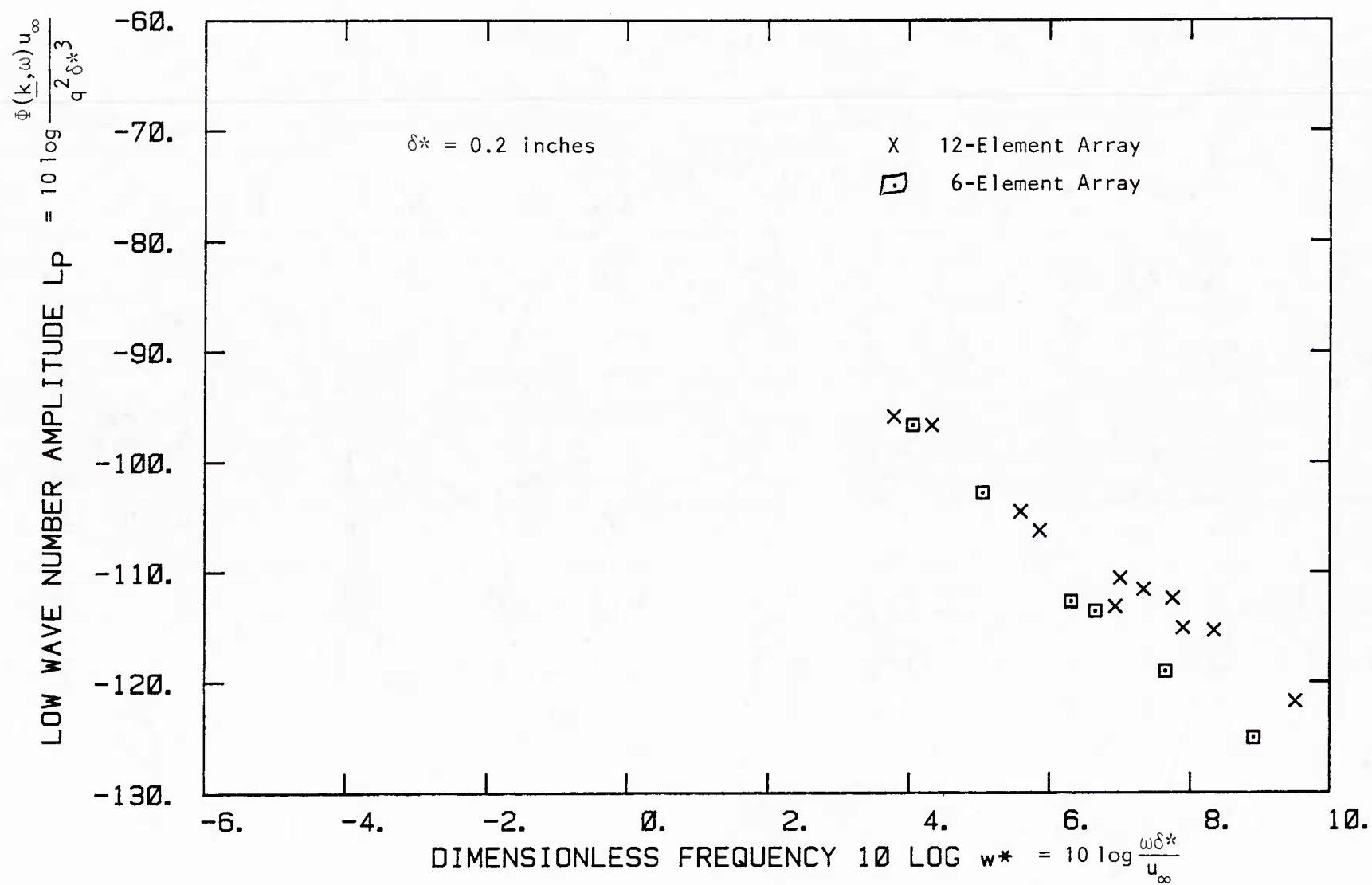


Figure A8. 12-Element Collinear Array, Chebychev Shading, Low Wavenumber Results

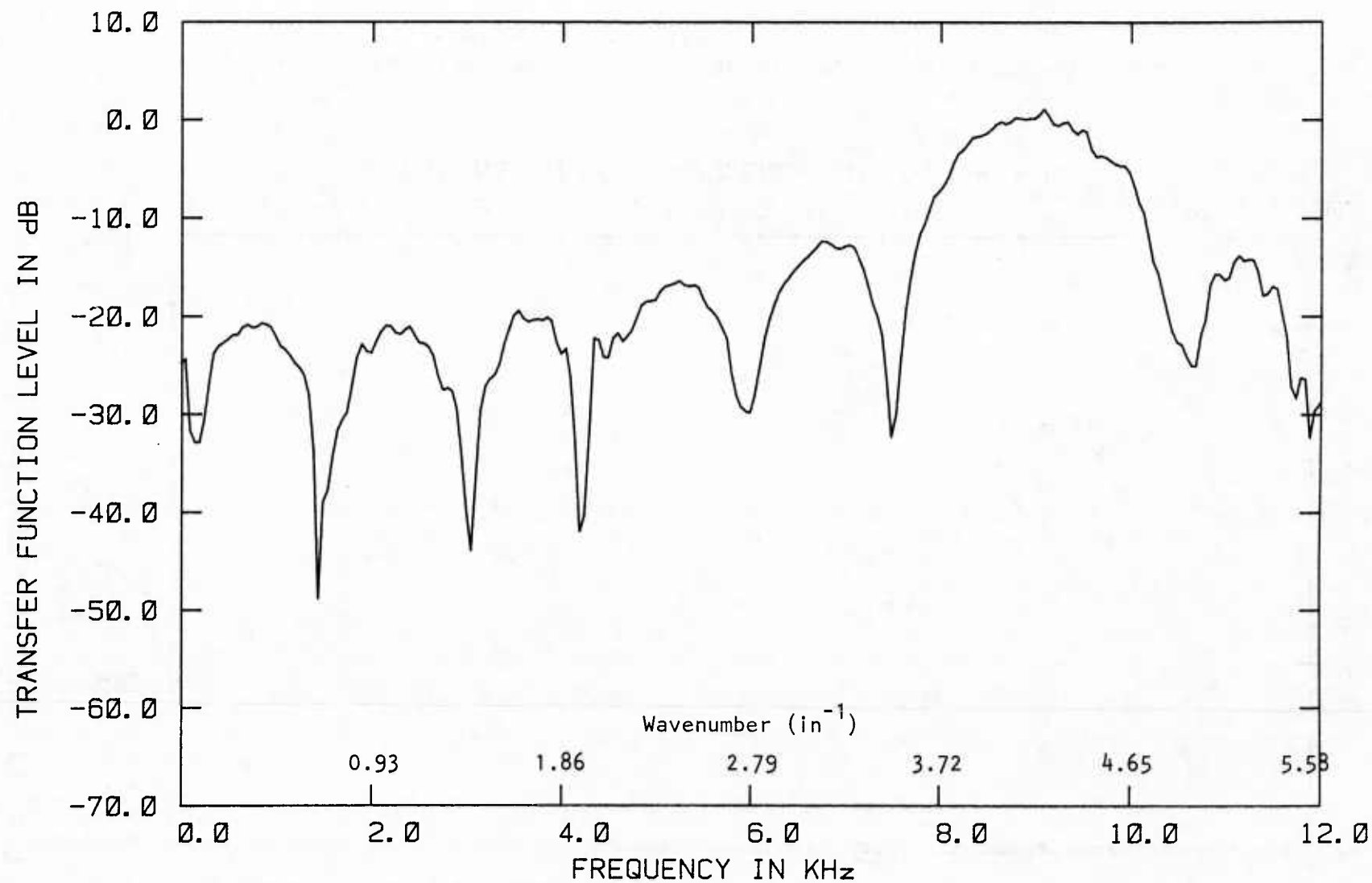


Figure A9. 12-Element Stagger Array Alternating Phased Wavenumber Response

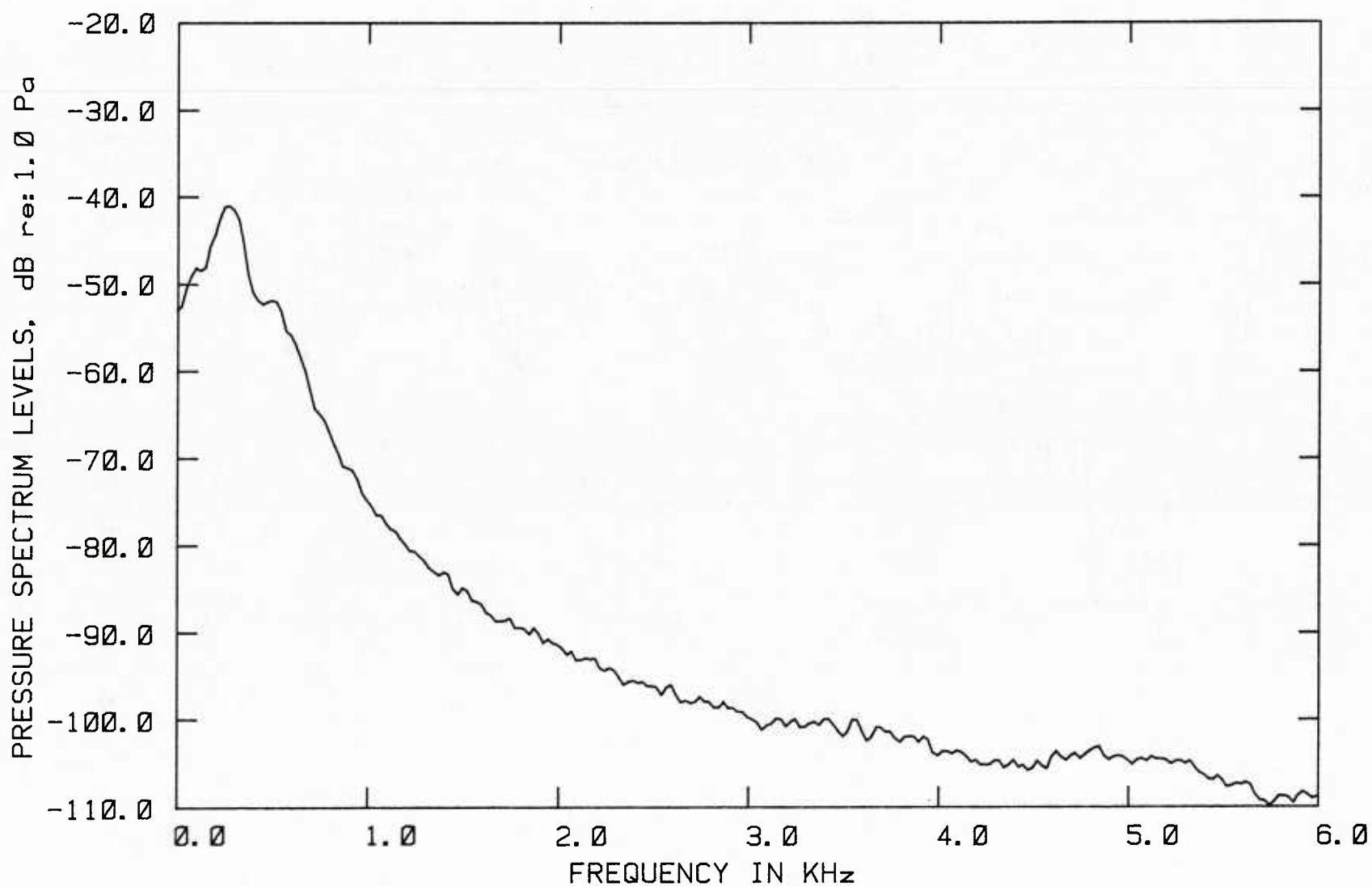


Figure A10. 12-Element Stagger Array Alternate Phased @ 15 m/s

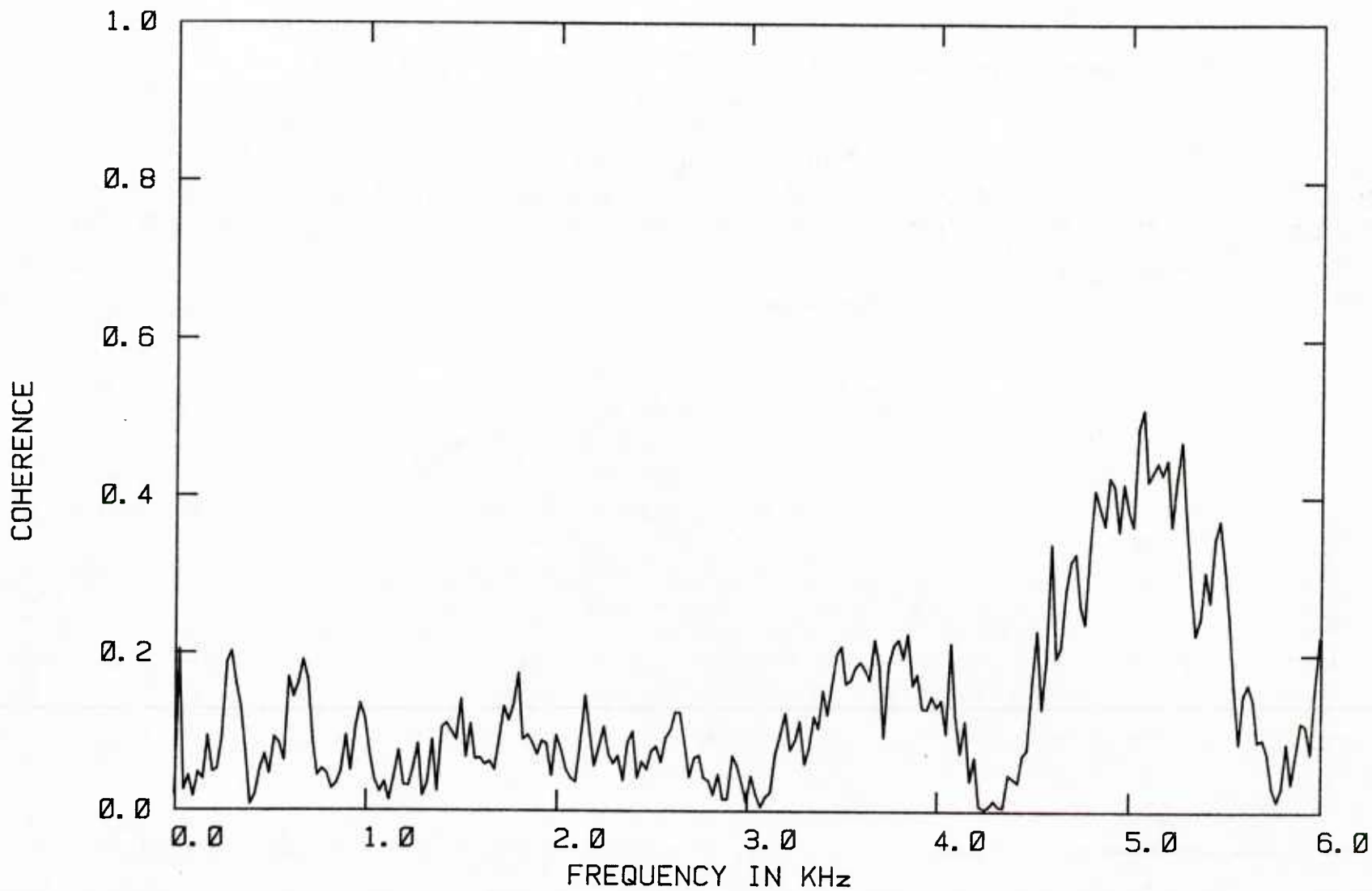


Figure A11. Coherence of 12-Element Stagger Array @ 15 m/s

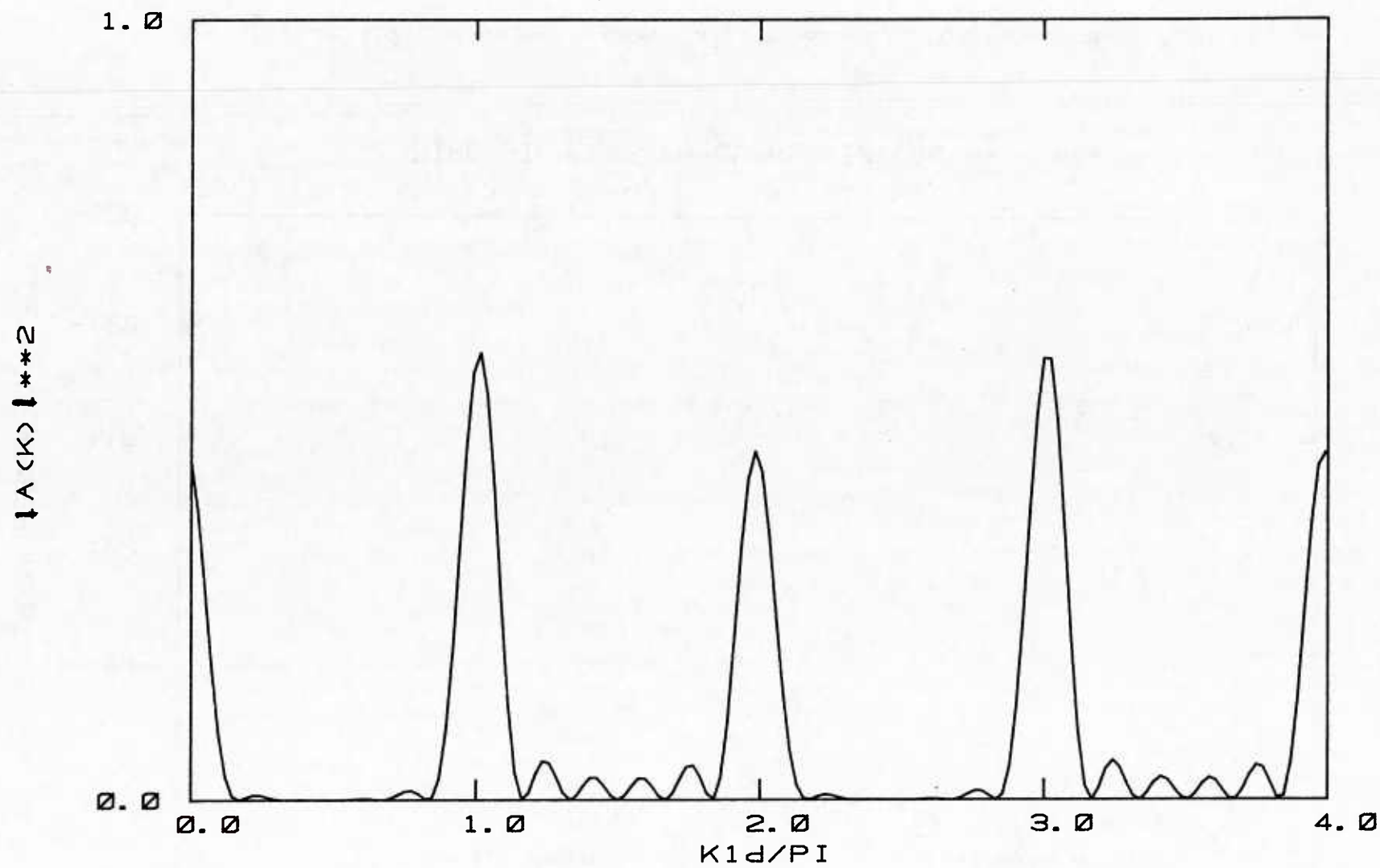


Figure A12. Alternate Phased Stagger array Wavenumber Response
 @ $k_3 = 1.4\pi/d_3$

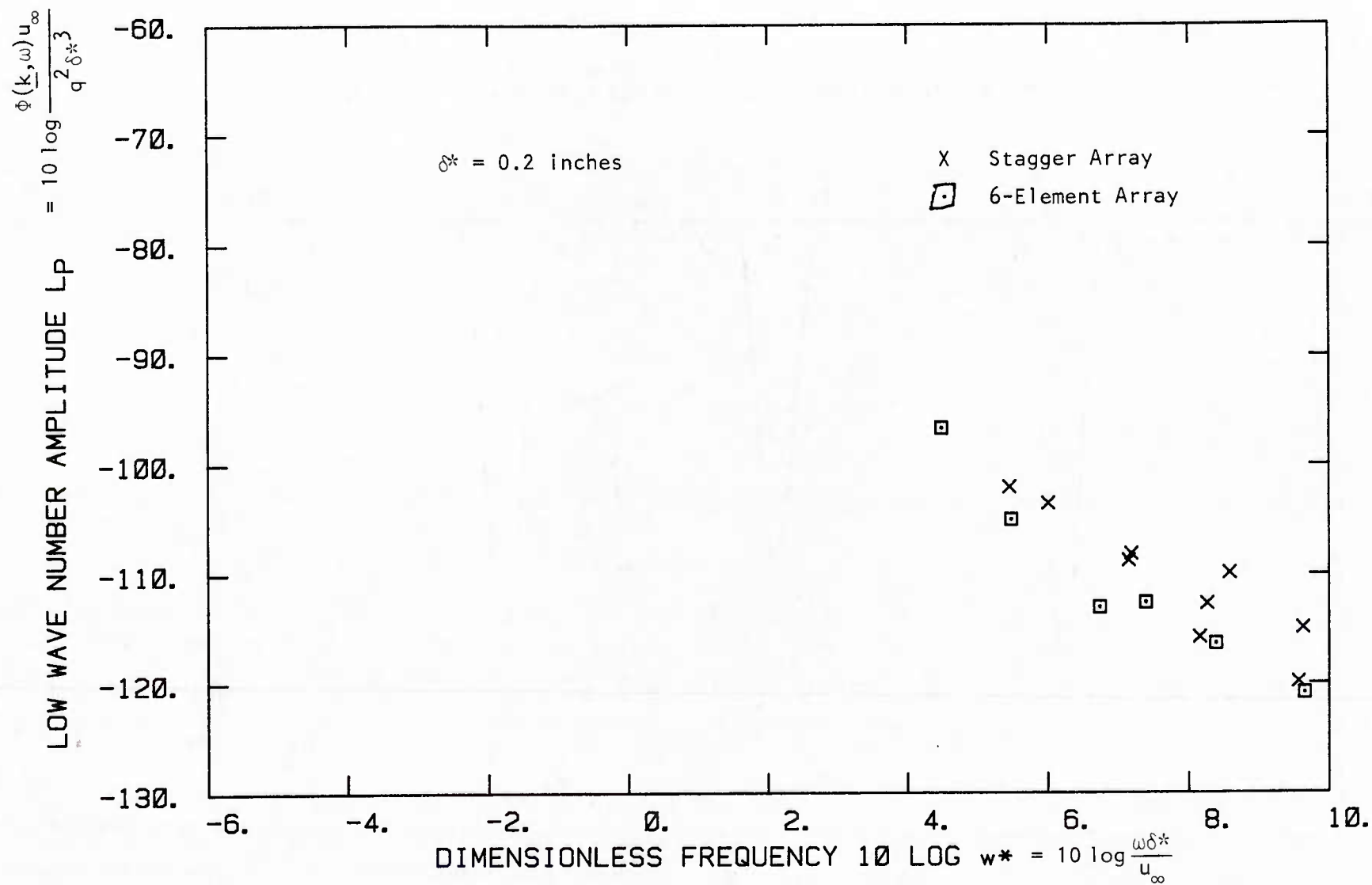


Figure A13. Stagger Array, Uniform Shaded, Low Wavenumber Results

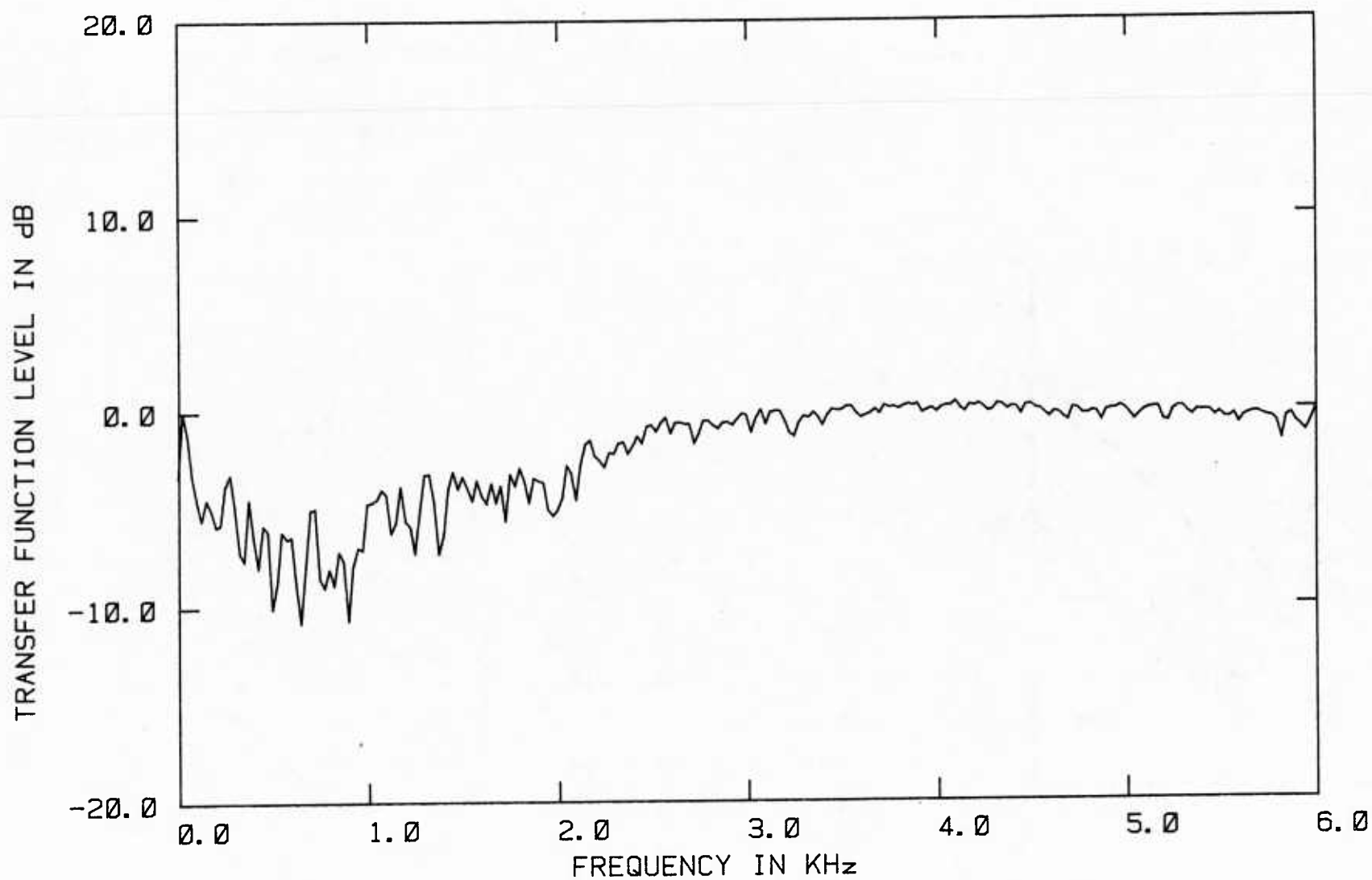
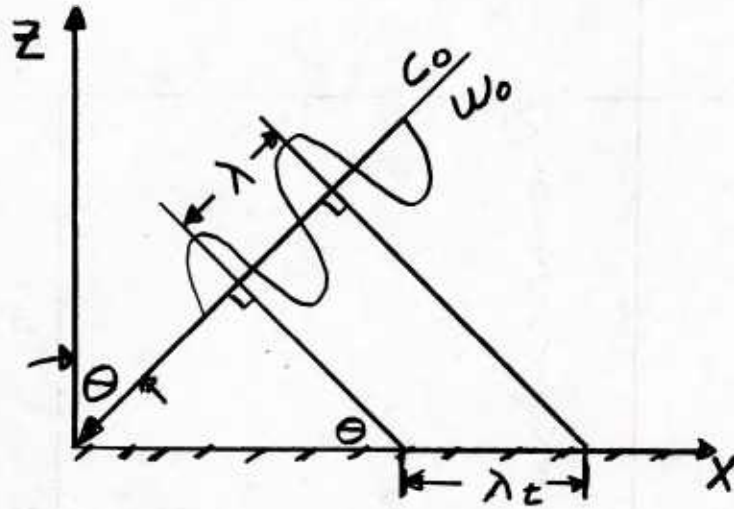


Figure A14. Transfer Function Between Lateral Array and Single Microphone @ 15 m/s



Trace Wavelength = λ_t

$$\lambda_t = \frac{\lambda}{\sin\theta} \quad \lambda_t \geq \lambda$$

Trace Wave Speed = c_t

$$c_t = \frac{c_0}{\sin\theta} \quad c_t \geq c_0$$

Trace Wavenumber = k_t

$$k_t = k \sin\theta \quad k_t \leq k$$

Figure B1. Trace Waves.

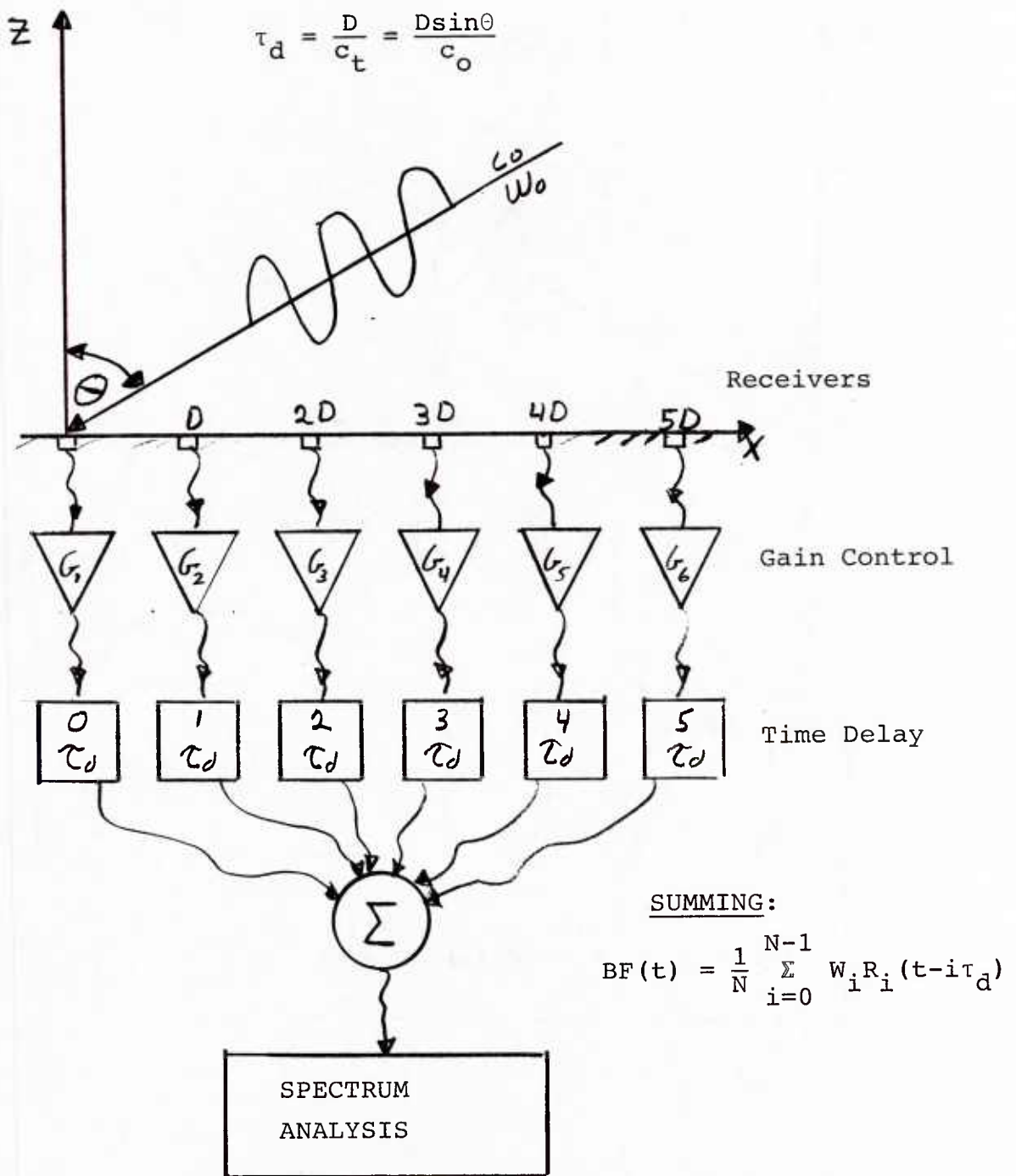


Figure B2. Weighted Delay-and-Sum Beamformer.

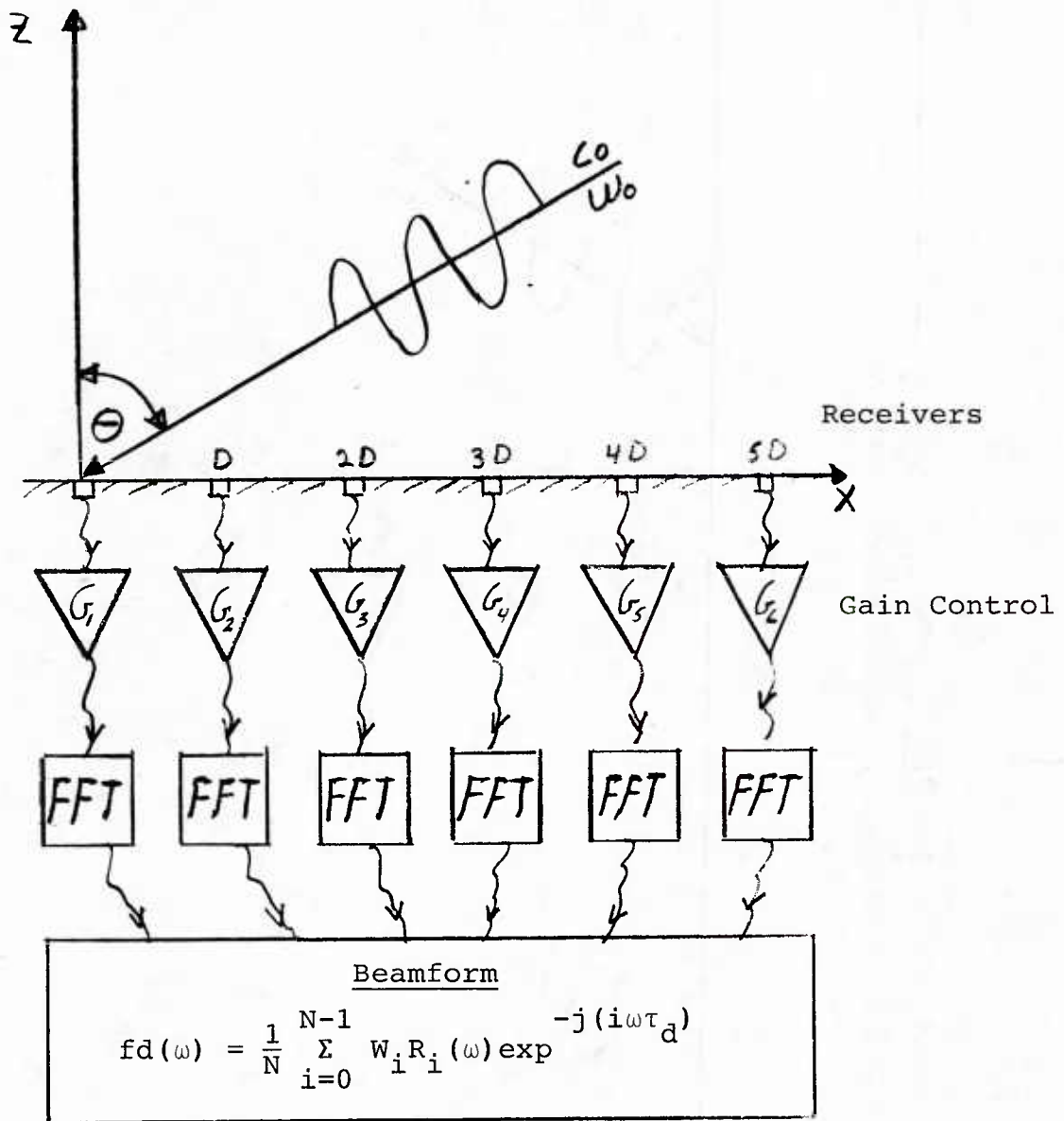


Figure B3. Frequency-Domain Beamforming.

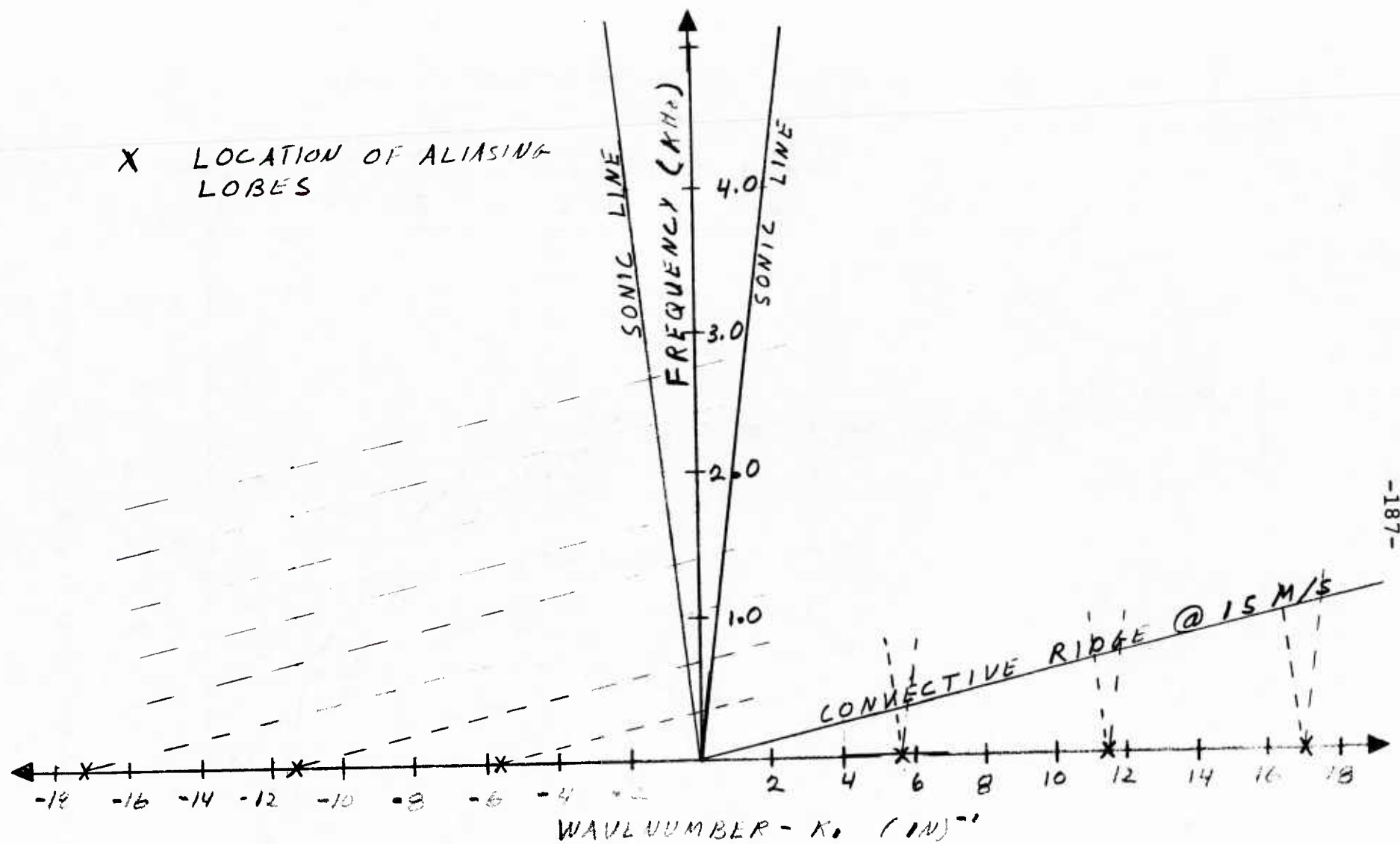


Figure B4. Relationship Among Turbulent and Acoustic Pressure Spectra in Wavenumber-Frequency Plane

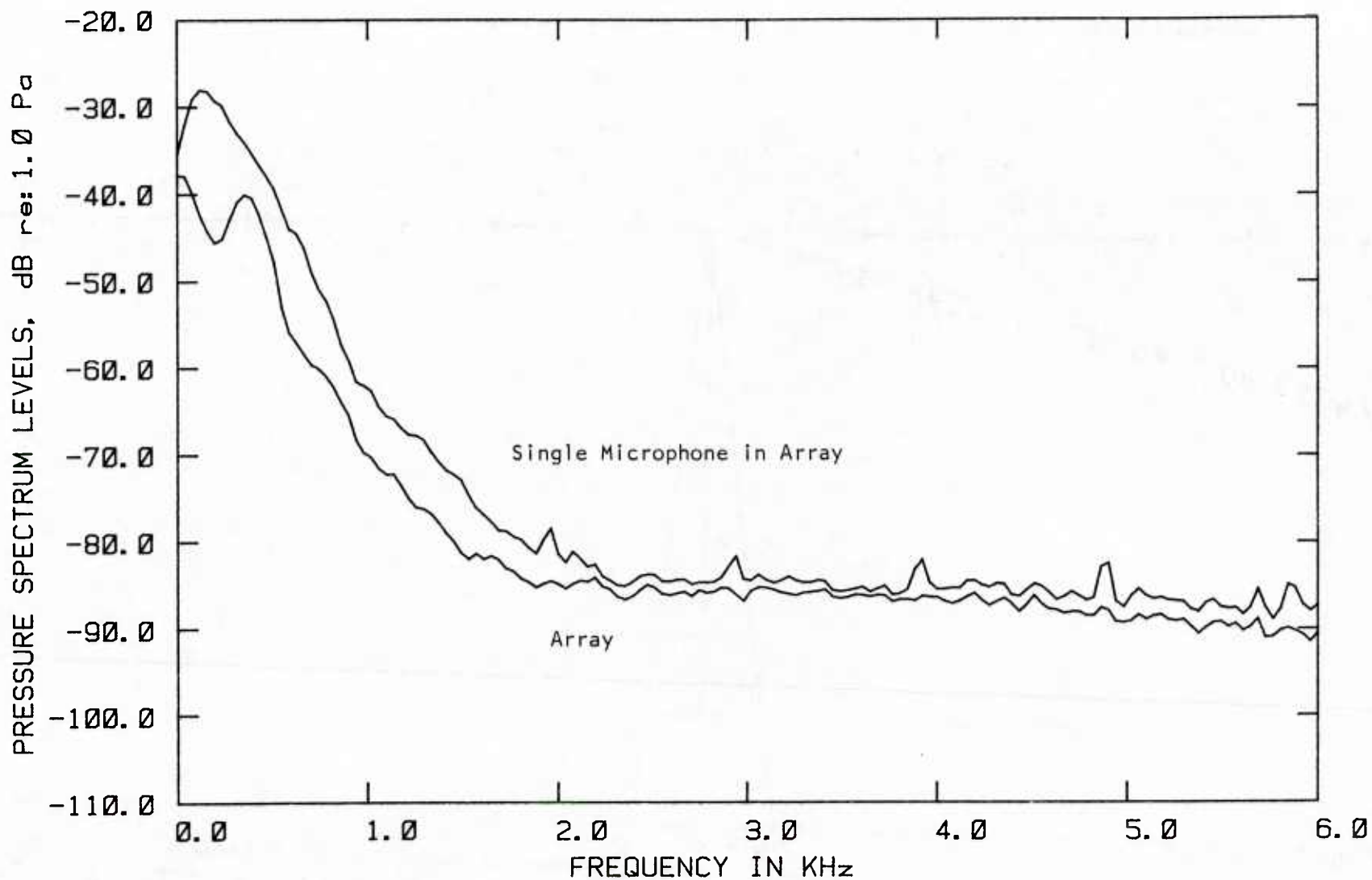


Figure B5. Downstream Acoustic Steered Array @ 15 m/s

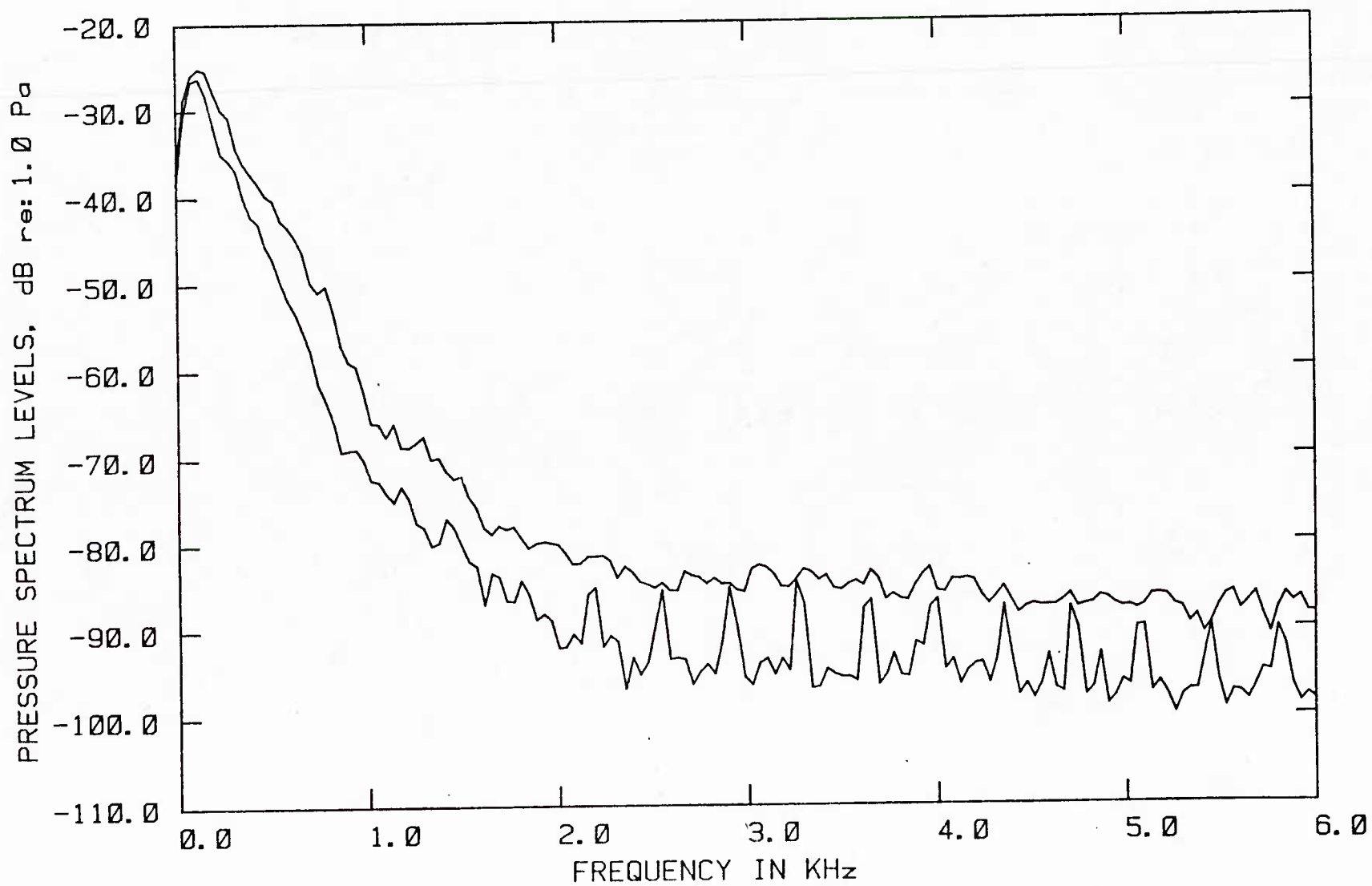


Figure B6. Upstream Convectively Steered Array @ 15 m/s

U215427